Some Effects of Non-Stoichiometry in Antimony Telluride

A thesis presented
for the degree of Doctor of
Philosophy
in the
University of London,

by

Michael John Philip Payne, B.Sc., A.R.C.S.

June, 1966

Department of Metallurgy,
Imperial College of Science
and Technology,
London.

ABSTRACT

A critical review of the literature shows that few of the properties of antimony telluride are well understood. The material is highly anisotropic and exhibits properties characteristic of a heavily doped semiconductor.

Single crystals were produced by a zone melting technique. Diffusion was used to alter the composition of surface layers of the crystals. The layers were investigated electrically using a new extension of the well known four probe technique. The theory of the new method is fully presented and the application of the method discussed. The results are discussed from the point of view of the phase diagram of the antimony-tellurium system and of the electronic band structure of antimony telluride. A two valence band model is seen to be appropriate in the latter case.

CONTENTS

Title page 1

Abstract 2

Contents 3

CHAPTER I. INTRODUCTION 7

CHAPTER II. PROPERTIES OF MATERIALS 11

2.1. Introduction 12

2.2. The Theory of Electrons in Solids 13

2.3. Heavily Doped Semiconductors 15

2.4. Properties of Antimony Telluride 19

i Crystal Structure 19

ii Transport Properties 23

iii Optical Properties 29

iv Band Structure 29

v Chemical Structure 34

vi Crystal Composition 36

vii Other Properties of Antimony Telluride 39

2.5. The Antimony-Tellurium Equilibrium Diagram 40

2.6. Conclusions 45

CHAPTER III. PREPARATION OF SPECIMENS 46

3.1. Preferability of Using Single Crystals 47

3.2. Single Crystal Production 50

i Growth Techniques 50

ii Control of Crystal Growth 52

iii Previous Work on Growth of Sb_2Te_3 Single Crystals 56

iv Construction of Zone Melter 57

v Preparation of Specimens for Zone Melting 59

vi Crystal Growth 62

3.3. Further Preparation 68

3.4. Diffused Specimens 69

CHAPTER IV. EXPERIMENTAL TECHNIQUES 72

4.1. Introduction 73

4.2. Electrical Conductivity Measurement - Review of Methods 74

4.3. Electrical Conductivity Measurement - Theory 77

i Theory of the Potential Distribution in Inhomogeneous Media 77

ii New Method of Analysing the Potential Distribution 83

iii Anisotropic Case 93

4.4. Electrical Conductivity Measurement - Apparatus 97

i The Four Point Probe - Arrangement of Contacts 97

ii The Four Point Probe - Construction 100

iii The Four Point Probe - Use 101

iv The Four Point Probe - Thermal Effects 104

4.5. The Electrical Circuit and Its Use 106

i The Circuit 106

ii Design of the Chopper 108

iii Adjustment of the Chopper 109

4.6. Other Measurements of Conductivity 111

4.8. Determination of Specimen Composition 114

4.9. Thermoelectric Power 115

CHAPTER V. RESULTS

5.1. Electrical Measurements on Homogeneous Samples 117

i Electrical Conductivity 117

ii Hall Coefficient 118

iii Thermoelectric Power 119

5.2. Electrical Measurements on Diffused Samples 120

i Sheet Conductivity and Hall Coefficient Measurements 120

ii Four Probe Measurements - Method of Analysis 122

iii Four Probe Measurements - Analysis of Experimental Curves 128

iv Interpretation of the Derived Parameters in Terms of the Conductivities 133

5.3. X-ray Diffraction and Measurement of Crystal Composition 135

CHAPTER VI. DISCUSSION 137

6.1. Specimen Composition and the Equilibrium Phase Diagram 138

6.2. The Electrical Measurements 142

6.3. Discussion of the Conductivity Measuring Method 155

SUMMARY AND CONCLUSION 161

REFERENCES 162

ACKNOWLEDGEMENTS 180

APPENDIX I. Summary of Electronic Transport Formulae 181

APPENDIX II. The Distribution of Electric Potential in Inhomogeneous Media which are Anisotropic in the Horizontal Plane 186

APPENDIX III. i Radial Heat Flow from an Oscillating Source 190

ii The Measured Thermal Effect 192

iii An Alternative Expression for the Temperature Distribution 195

APPENDIX IV. List of Symbols 196

List of Tables 199

Diagrams 200

C H A P T E R I

I N T R O D U C T I O N

CHAPTER I

INTRODUCTION

Prior to the present century the study of the physical properties of metals formed, in the main, an empirical technology, albeit a successful one. The recent expansion of other forms of engineering and of the physical sciences produced a need for the rapid development of new materials. To meet these needs adequately a deeper understanding was required of the properties of solid matter. Theories were proposed and predictions from these indicated new uses for solids, while verifying the theories themselves.

Notable among these new uses is the transistor, a device whose principal feature is a crystal of a semiconducting material. Invented in 1948 (1), the transistor, by virtue of its small size, low power consumption and long life, has almost replaced the thermionic valve in electronic circuitry. On the scientific side, its development has been the main cause of the large effort now devoted to semiconductor research. A further practical application of semiconductors is the conversion of

thermal energy to electrical energy and vice versa by thermoelectric means (the Seebeck and Peltier effects, respectively (2)). These effects are applied in thermoelectric generators and refrigerators. Certain alloys of antimony telluride, the compound of present interest, are the most efficient materials known for use as elements in this type of refrigerator. About 60°C of cooling can be produced by this means (3).

Physical theory, in particular the quantum theory, has answered many questions concerning the solid state. Certain items of information about a substance can often be easily determined experimentally (e.g. the chemical composition, crystal structure and the simpler electrical, mechanical and thermodynamic parameters). It is then frequently possible to predict, using the theory, the general behaviour of the substance under a wide variety of conditions. However, the more fundamental and complex problem of deducing the parameters from the properties of the constituent elements alone has not yet been solved. The basic knowledge required is the complete description of the forces between atoms in any environment. Such knowledge would immediately give the stable crystal

structure and cohesive forces for any combination of atoms. The thermodynamic properties, which must now be found for each case individually, would be determined. This ideal situation is still distant, however, and present experimental work is often directed to the reverse process, that of finding the interatomic forces from the experimentally derived parameters.

This work describes a technique for measuring the electrical conductivity of thin, inhomogeneous layers on large samples of a base material. It is expected that this method will prove of use in cases where such thin surface layers are the only form in which a substance can be prepared or where large samples would be inconvenient to make.

During the work here described, a substantial portion of the total effort was put into the production of the antimony telluride single crystals which were needed subsequently. For this reason a complete section of this thesis is devoted to the description of the crystal growth technique. This section and that concerning the other experimental methods contain also their relevant literature reviews. The first chapter of the thesis consists of the literature review devoted to the properties of materials.

C H A P T E R I I

P R O P E R T I E S O F M A T E R I A L S

CHAPTER II

PROPERTIES OF MATERIALS

2.1 Introduction

One of the main features of present materials research is the general inaccuracy of any prediction of a particular property of a material; to obtain reliable information each case must be individually investigated. An important aim of research is to reduce the apparent disorder of this situation by discovering correlations between the various properties of substances. The relationships discovered to date have led to the establishment of a number of theories of wide applicability. However, while these theories are generally sufficient to explain experimental data, the accurate forecasting of a parameter of a substance is seldom achieved. A more direct method of estimating a parameter before measurement is to extrapolate from values of the same quantity determined for other, related, materials. While there is no guarantee of success with this approach, its use frequently gives a first approximation to the truth.

Both systems are used in the present work. The

electronic theory of matter is sufficiently well developed to permit both the forecasting and interpretation of actual behaviour. On the other hand, the similarities observed between antimony telluride and the well-studied bismuth telluride are of use in interpreting results for the former compound.

2.2 The Theory of Electrons in Solids

The main properties of electrons in solids are well known and have been described many times (for example (4)). These properties may be described by a small number of functions most of which are characteristic of the particular material and, in general, depend upon its history also. These functions include

i $\varepsilon(\underline{k})$, the electron energy as a function of the wave vector, $\underline{k}$. This defines the electron dynamics.

ii $n(k)$, the density of allowed electron states per unit volume of phase space.

iii $f(\varepsilon)$, the Fermi-Dirac distribution function, which gives the distribution of electrons among the allowed states at any temperature, $T^{o}K$. The parameter ε_F appearing as a parameter in $f(\varepsilon)$ is called the Fermi energy.

iv n, the total number of electrons in the highest occupied bands. Although dependent on temperature, in semiconductors n may often be independently varied by doping.

v $\tau(\underline{k})$, the relaxation time for perturbations of electrons of wave vector $\underline{k}$.

Using these quantities expressions for all the galvano-thermomagnetic coefficients may be obtained, with their temperature dependences (for examples, see (5)). These are discussed below for the relevant cases.

Of the functions above both $n(k)$ and $f(\epsilon)$ are known exactly and, except for unknown defects in a specimen, so is n. A complete knowledge of the band structure thus involves the simultaneous determination of $\epsilon(\underline{k})$ and $\tau(\underline{k})$, a difficult task experimentally. However, the theoretical determination of $\epsilon(\underline{k})$ has improved greatly in recent years (6) and this function has been determined for a variety of materials by various methods. The quantity $\tau(\underline{k})$ can also be calculated for various types of scattering mechanism and, given $\epsilon(\underline{k})$ these types may be distinguished experimentally by their different temperature variations. The most important region of $\underline{k}$-space is that near the Fermi

surface and the relevant band properties can in principle be determined from a suitable selection of the galvanomagnetic coefficients (7). Recently methods have been devised for experimentally investigating the complete band structure (8-11).

2.3 Heavily Doped Semiconductors

As will be seen, the compound antimony telluride has been prepared only with carrier concentrations of about 10^{20} /cc. Optical measurements show a band gap of 0.28 eV (12, 26) and the material may thus be classed as a heavily doped semiconductor. The high carrier concentration does not necessarily mean that degenerate statistics are relevant, but this is likely to be so.

Theoretical examinations of materials of this type have been carried out during the last ten years. The complete analysis involves the solution of the many-body problem for the electrons in the crystal containing a large number of point defects, generally considered to be disordered, which themselves interact with the electrons. The problem has not been treated in full generality; the approximations used

have included i a one dimensional model, ii the electron-electron interaction is given by a screened potential of some kind, iii perturbation theory is used, iv a free-electron type of dispersion law is used. Some of the papers on this subject are given in reference 13. The main point emerging from these papers is that in these materials there is a small, but finite density of electronic states across the complete width of the so-called forbidden energy gap which thus has little meaning in a heavily doped semiconductor. These states are just the impurity levels in the lightly doped material, broadened into a band by the defect interaction. The Hall coefficient of such materials was considered by Zvyagin (14).

Mott (15) has suggested that in the carrier concentration range under discussion there is a sharp transition, with decreasing concentration, from a metallic state, with one free electron per atom, to a non-metallic state with a finite energy gap. The effect, if it occurs, cannot be easily distinguished in highly doped semiconductors from possible consequences of the disorder which is necessarily present. Other possible evidence for the effect has been discussed briefly by Mott (16).

The experimental investigation of materials with high carrier concentrations was stimulated by the discovery of the ESAKI effect (17), (the tunnel diode) in n-p junctions in heavily doped germanium. Much of the subsequent work on highly doped specimens has been done on this material (18). Measurements at high carrier concentrations have also been made on bismuth telluride (7), indium antimonide (19), lead telluride (20) and tin telluride (20, 21) among others. Frequently in these studies it has been found impossible to explain the results accurately on the basis of multi-valley structures (i.e. the $\varepsilon(\underline{k})$ variation possesses multiple, usually equivalent, minima) with constant effective mass tensors. The effects of the non-parabolic form of the bands are invoked to explain this. In consequence, a theory of non-standard energy bands has been developed (22). The optical properties of degenerate semiconductors have been reviewed by Sebenne (11). Again, the Fermi energy shifts away from the band extrema and the small variation of the density of states effective mass is observed.

In the theory of the transport phenomena of standard (i.e. parabolic) energy bands the Fermi-Dirac functions

$$F_n(y) = \int_0^\infty x^n (1 + \exp(x - y))^{-1} \, dx$$

appear. These have been tabulated for most of the important cases (23). The formulae for the main transport properties in terms of the Fermi-Dirac functions and the other relevant parameters are given by Putley (24). They are summarised in Appendix I.

In many cases the transport coefficients in solids cannot be explained using a single band model. A two band model allows the measurements to be fitted using a double set of parameters and an additional variable, the energy difference between the band extrema. The electrical conductivity is the sum of the contributions from each band. The analysis of the Hall coefficient in terms of this model, for arbitrary degrees of degeneracy, has been given by Allgaier (25) for bands of standard type. This work is able to explain the increase with temperature of the Hall coefficient which has been observed in several materials, Bi_2Te_3 (26), GaAs (27) and PbTe amongst others. The two band model is appropriate in situations other than those when two bands actually exist at the Fermi level. For instance, an $\varepsilon(\underline{k})$ variation may exhibit extrema at non-equivalent points within a Brillouin zone and carriers near these extrema have in general different properties. The

carriers may then be divided into several (usually two) groups and the multi-band model applied to these.

2.4 Properties of Antimony Telluride

Antimony telluride is of commercial interest chiefly as a component in alloys with the closely related compounds bismuth telluride and bismuth selenide. Such alloys are among the most efficient materials known for thermoelectric refrigeration (28). Interest in the more fundamental properties of the material has been very limited, probably because of the apparent impossibility of producing an intrinsic form. Any semiconducting properties which the compound possesses are largely lost and no uses have been proposed for it other than that mentioned above.

Antimony telluride has strong similarities to bismuth telluride, upon which much work has been done. It is often advantageous to draw analogies between the two and this will be done where convenient in the following work.

i Crystal Structure

There is some doubt as to the detailed structure of

antimony telluride (29). The compound was supposed by Pearson (30) to be isotypic with bismuth telluride, as stated by Ramsdell (31). Bismuth telluride was described by Lange (32) as having the D_{3d}^5 ($R\bar{3}m$) space group but this remains unconfirmed. Semiletov (33) showed that this is a valid description of antimony telluride, however, and gave the interatomic distances. Bercha (29), on the basis of measurements of the piezoresistance of Sb_2Te_3, has discounted the D_{3d}^5 space group for this substance, but his interpretation of his results is dubious. This point will be discussed later in connection with the band structure of the material. Meanwhile the D_{3d}^5 space group seems the most probable and is assumed forthwith.

There is no doubt, however, that the unit cell of the Sb_2Te_3 lattice is hexagonal with the (most probable) parameters

$$a_{Hex} = 4.265 \text{ ÅU.} \qquad c_{Hex} = 30.43 \text{ ÅU.} \qquad (33\text{-}38, 102)$$

An alternative description of this cell may be given in terms of a rhombohedral structure; in this case the basis vectors are all of length 10.44 ÅU and are mutually inclined

at an angle of 23.23°. This C33 (tetradymite) structure has been described by Mooser and Pearson (39) as follows. It is built up of multiple layers, each of which contains five atomic sheets in the sequence - $X^{(1)}$ - M - $X^{(2)}$ - M - $X^{(1)}$ -, where M represents the metal atoms, (here antimony) and X the metalloid atoms (here tellurium). The superscripts on X are used to distinguish two types of differently bonded X atoms. The stacking of these sheets is such that each atom inside one of the five-fold layers acquires a distorted octahedral neighbourhood. The X atoms at the boundary of each multiple layer have three nearest M neighbours in the same multiple layer and three next-nearest X neighbours at a somewhat greater distance in the adjacent multiple layer.

The height of the hexagonal cell is three of the five-fold layers. The interatomic distances have been found by Semiletov (33) to be

$$Sb - Te^{(1)} = 3.07 \text{ Å U}$$

$$Sb - Te^{(2)} = 3.17 \text{ Å U}$$

$$Te^{(1)} - Te^{(1)} = 3.63 \text{ Å U}$$

Thus the $Te^{(1)} - Te^{(1)}$ bonds, those between the multiple layers, are considerably longer than the other bonds in the system. It is likely that they are also much weaker than either type of Sb - Te bond. The observed very easy cleavage of Sb_2Te_3 in the basal (hexagonal 0001) plane is explained on this basis. The existence of these weakly bonded planes serves to emphasise the anisotropic nature of the structure which manifests itself in most of the physical properties of the compound.

The interatomic distances in bismuth telluride and bismuth selenide are similar to those in antimony telluride and the same type of anisotropy is observed.

The first Brillouin zone for bismuth telluride has been worked out by Koster (40). In view of their similar lattice parameters, the antimony compound has a very similar zone.

Andrievskii (41) has described an amorphous form of antimony telluride, obtained by vacuum deposition. The interatomic distances and coordination numbers in the amorphous and crystalline forms are quite different, indicating that there is no similarity between the two structures.

ii Transport Properties

Second to its anisotropic character, perhaps the most striking property of antimony telluride is the high concentration of current carriers which it always exhibits. These carrier densities are far in excess of those calculated on the assumption of intrinsic conductivity, or from the known maximum concentration of impurity elements. Carrier concentrations of the order of 10^{20} /cc. have been deduced from Hall coefficient measurements on single crystals (26, 42-45). In these experiments the magnetic field was presumably normal to the crystal cleavage planes. Measurements on polycrystalline material (35, 46, 47) yield generally higher values of the Hall coefficient. This implies that the second coefficient for single crystal material is larger than the first, described above. Such anisotropy of the Hall constant has also been observed in bismuth telluride (48, 49).

The Hall measurements indicate p-type conduction in all specimens. The carrier concentration is high so that degenerate conditions probably prevail. The published Hall data are shown in figure 1. The increase of the Hall coefficient with temperature is unusual. For an isotropic

material the simplest explanation of this phenomenon requires a two band model (25). For anisotropic materials an explanation has been given (49) involving the change of anisotropy of the relaxation time with the change of the relative importance of impurity scattering as the temperature rises.

The information in the literature on the electrical conductivity of antimony telluride is quite extensive (figure 2 and table 1). The temperature variation has been found (42-46, 50), generally using single crystals. Only the results of Movlanov (42) show typical doped semiconductor behaviour. His specimens seem to have been somewhat untypical (see also the Hall coefficient data). The anisotropy ratio of conductivity, $\frac{\sigma_{11}}{\sigma_{33}}$, has been measured (the directions 1 and 3 are respectively perpendicular and parallel to the trigonal axis). Jüschke (25) reported values of about 100, Movlanov (42) a value of 7 and Bercha (29) values from 10 to 20. The high ratio found by Jüschke may be in part due to his method of preparation which involved cutting the single crystals with a razor blade at liquid nitrogen temperature, giving a high probability of crack formation in the cleavage planes. Such cracks would

not appreciably affect the measurements made for current flow parallel to the cleavage plane. The measurements of Harman (46) on polycrystalline material revealed a conductivity only about 30% lower than the values of σ_{11} just discussed. This is further evidence suggesting that the anisotropy ratio of conductivity is not too large.

Bercha (29) has investigated the piezoresistance of antimony telluride and has found that the coefficient derived from the effects of a force perpendicular to the cleavage planes is not zero. Klinger (51) predicted a value of zero from symmetry considerations. Similar effects are seen in bismuth telluride (52). This particular coefficient is difficult to measure because of cracking of the sample. The effect may be accounted for by either i assuming the crystal lattice to have a symmetry other than D^5_{3d}, ii a change of the effective mass when pressure is applied, iii a change of the scattering or iv incompleteness of the suggested band model (described later). Of these, case i seems unlikely.

The available data on the thermoelectric power of antimony telluride (35, 42-44, 46, 53-58, 102) are shown in figure 3 and table 2. The results are consistent with the picture of antimony telluride as a degenerate semiconductor.

The results of Movlanov (42) are again exceptional although all of his results are self consistent in showing a transition to apparently intrinsic behaviour above a temperature of about 350°K. A discontinuity in the results of Parrott and Penn (53) at about 170°K was attributed by them to a change in the scattering mechanism near the Debye temperature. A similar discontinuity appeared in their conductivity data. The high temperature mobility is thus probably limited by scattering from lattice vibrations of the acoustic mode. This result was found also by Brodovii (43).

Rönnlund (59) has measured the variation of thermoelectric power with electrical conductivity at room temperature by doping the material. On the assumption of acoustic scattering and isotropic energy bands his data were interpreted using a two valence band model. As the carrier concentration is raised the Fermi energy approaches the bottom of the upper band. The results can perhaps be equally well analysed considering simply a conduction band - valence band system, with the bands possibly overlapping. In this case the Fermi level in a p-type material becomes remote from the conduction band as the number of carriers is

increased and a single band approximation is valid. For low electrical conductivities the increased number of electron carriers causes a lowering of the thermoelectric power. Both of these statements apply to Rönnlund's data. Indeed, an apparently similar, but more striking effect in bismuth telluride has been analysed in this way (3, 53).

Anisotropy of the thermoelectric power has not been investigated.

A fourth transport property, the thermal conductivity, has been measured in antimony telluride (3, 35, 44, 46, 53, 55, 60) (figure 4). The reason for the very large discrepancy in the low temperature data is not known. The increase in thermal conductivity at high temperatures is thought to be due to ambipolar diffusion, i.e. simultaneous transport of both electrons and holes (61). Proof of this would support an analysis of the thermoelectric data of Rönnlund (59) in terms of a valence and conduction band model.

The only other measurements of transport properties in the compound are those of Katsugi (62) who determined all the magnetoresistance coefficients for current flow parallel to the cleavage planes, at 77°K. His results are consistent

with the six-valley model proposed by Drabble (7) to explain the properties of p-type bismuth telluride. It should be noted that the notations of Katsugi and Drabble are slightly different; the effective masses m_1 and m_2 must be interchanged. The substitution of Katsugi's results into his initial equations leads to a value of the conductivity anisotropy, $\frac{\sigma_{11}}{\sigma_{33}}$, equal to 0.74. Since this ratio should almost certainly be greater than unity (49, 50), doubt is cast upon the whole analysis. It is unfortunate that Katsugi did not measure the value of σ_{33}. This result may arise in two ways. Anisotropy in the scattering would invalidate the initial equations. Secondly, the calculations lead to a quadratic equation. Thus two sets of effective masses may be derived from a single set of data and further experiments are required to determine which set is valid. Possibly Katsugi chose the wrong set of results. The two sets of results may be widely different (49).

An effective hole mass of 1.2 times the free electron mass was found by Brodovii (43) from his thermoelectric power measurements. Hole mobilities (derived from Hall coefficient measurements) between 270 and 360 cm^2/volt. sec. have been reported (26, 35, 47, 53). Eichler (47) has found

the thermal energy band gap to be 0.20 eV. but his specimens were intrinsic only above 400°C.

iii Optical Properties

Measurements of optical effects, such as absorption, reflection and Faraday rotation, can be important in band structure determination. In the present instance, they can remove the indeterminacy of the band parameters pointed out in the previous section.

Black (26) measured the infra-red absorption and found the energy gap to be about 0.3 eV. More comprehensive measurements made by Sohr and Testardi (12) indicate a gap of either .21 eV. or .28 eV. depending on the method of analysis. The transitions are thought to be indirect. A certain combination of effective masses may be derived from the absorption data. Using this quantity in conjunction with Katsugi's (62) results yields actual effective masses. These effective masses are about twice those found by Brodovii (43) who, however, used a spherical band model.

iv Band Structure

The aim of the foregoing work has been to determine

the $\varepsilon(\underline{k})$ and $\tau(\underline{k})$ variations for carriers near the Fermi surface, which lies near the valence band extrema. It has been seen that doubt exists concerning even some of the major features, such as the shapes of the equi-energy surfaces and their location in the Brillouin zone. In view of the great similarities in atomic types, crystal structure and transport properties between antimony telluride and bismuth telluride it seems certain that the band structures of these compounds are very similar. Further support for this is adduced from the properties of alloys of the compounds. When allowance is made for changes in degeneracy and ordering (63), the transport properties (35, 44) vary uniformly across the system. (The results of Benel (54) do, however, exhibit discontinuities.) A particularly crucial parameter, the energy gap, is continuous when measured optically (12); Eichler's result (47) for the thermal energy gap may be fitted on to a graph (37) for this quantity up to 67 at. % of antimony telluride. The proof of a single alloy phase across the whole composition range was given by Smith (37). As is then expected, the density (64) and lattice parameters (36) both vary continuously.

Thus it appears valid to use the qualitative features

of the bismuth telluride band structure in discussing the antimony compound. A description of the former band structure is now given. From considerations of symmetry, band extrema can exist at points on the ΓA, ΓD and ΓZ lines in the Brillouin zone described by Koster (40) (figure 5). A six-valley model has been found to be a good fit for the experimental data on p-type bismuth telluride (49, 65-67). The valence band extrema therefore lie somewhere on the lines ΓA or ΓD (I or K, say) since such points have the required six-fold degeneracy. The extrema do not lie at A, D or Γ, however, since these points have degeneracies of only 3, 3 and 1 respectively.

The parameters defining the isoenergetic surfaces are not accurately known (68). For n-type material an ellipsoid axis lies in the direction of ΓD, indicating that the extrema of the conduction band lie on this line (69). A similar type of conclusion cannot be found for the valence band since the measured orientations of the axes of the hole surface of equal energy fit no symmetry direction in the first zone. This surface may be similar to either a prolate or an oblate spheroid (49). Drabble's results for the effective masses (65) assumed an isotropic relaxation time.

As the scattering is anisotropic (49, 66), Drabble's results actually signify the quantities $(m^*/\tau)_i$ where m^* and τ are the ith components of the effective mass and relaxation time tensors, respectively (70). Better results are therefore those of Testardi (66), derived from studies using very high magnetic fields (de Haas - van Alphen effect, etc), although the derived quantities are not changed greatly. Measurements of the Shubnikov - de Haas effect in p-type bismuth telluride (67) yield similar results, as do Efimova's low field galvanomagnetic data (49).

Optical studies (9) give a similar picture. In addition, both the conduction and valence bands have extrema at the point Γ, the centre of the Brillouin zone, an unknown energy different from the extrema at I. This band structure is based, in part, on the theoretical investigation by Lee and Pincherle (71), who reached the same qualitative conclusions. A band overlap of about ½ eV. was found by them, however, due largely to the neglect of spin-orbit splitting in their augmented plane wave calculation. Their work, and that of Kudinov (72), using a tight binding approach, indicates that the extrema lie on the ΓD lines.

There is evidence for another set of extrema

energetically close to those described above. This evidence has usually (73-76) been derived from anomalies in the low field galvanomagnetic coefficients. Such anomalies were explained by Efimova (49) by a change in the type (and, hence, the anisotropy) of scattering in the range 100-200°K. Further evidence for anisotropic scattering was found by Dennis (77) from the thermoelectric power. The data on piezoresistance in bismuth telluride (52, 78) cannot be fitted to the six-valley model as described above. The anomalies may be due either to a change of effective mass or to a change in relative populations of two or more bands as the lattice parameters are altered. Since the effective mass must vary to some degree and since there is no other evidence for a multi-band structure, the effective mass change must be regarded, for the present, as the cause of the effects. The high field galvanomagnetic effects (66, 67) neither support nor disprove the multiband model. The effects mentioned in this paragraph may thus be explained in terms of the known properties of the material. The hypothesis of a multiband model, although consistent with the facts, need not be invoked.

To summarise, the Brillouin zones of antimony telluride

and bismuth telluride are very similar, and a six-valley valence band describes the properties of the p-type compounds. The atomic wave functions are similar. No relevant discontinuities appear in the properties of alloys of the compounds. Hence the valence band structures of the compounds may be regarded as qualitatively the same until proof to the contrary is presented. The comments concerning the bismuth compound are considered to apply equally to antimony telluride.

v Chemical Structure

Once again we may relate the work on bismuth telluride directly to that on antimony telluride. Some care must be taken, however, in view of the known differences in chemical behaviour between antimony and bismuth (79). These differences are thought to be due to the greater availability of the s-electrons for bonding in antimony (80), which leads generally to greater stability of antimony compounds. It is found that antimony telluride is less stable than bismuth telluride (81), contrary to this general tendency.

Mooser and Pearson (39) and Lagrenaudie (82) have

proposed bonding schemes for bismuth telluride, but neither theory is completely consistent with experimental data. Mooser's scheme is of interest, however, in predicting an electronic band, with very low density of states, which overlaps both the valence and conduction bands. The current, and so far completely successful, explanation of the bonding is that of Drabble and Goodman (83). According to these authors the bonds between the $Te^{(1)}$ atoms (see section i for notation) are of van der Waals type as are the bonds between adjacent chains in the structure of elemental tellurium. The presence of such weak bonds explains the large $Te^{(1)} - Te^{(1)}$ interatomic distance and the very easy cleavage of the material. The electron density in these bonds is small, leading to the observed electrical anisotropy. The valence electrons of the $Te^{(1)}$ atoms are used only in producing nearly perpendicular bonds to their three metal nearest neighbours. In these bonds only the p-electrons are used; the 5s-electrons form a lone pair. The $Te^{(2)}$ and metal atoms have nearly octahedral coordination and it is assumed that the bonding orbitals on these atoms are sp^3d^2 hybrids, using both s- and p-electrons.

The above system gives a fully saturated bonding structure with two electrons per bond. The semiconducting properties of the materials are thus explained, taking into account the energy gap determinations described earlier. The difference in length of the M - $Te^{(1)}$ and M - $Te^{(2)}$ bonds is due to the different type of wave function overlap in the two cases. The energies of these bonds should be similar, however, and gives rise to the possibility of second valence and conduction bands energetically close to those observed (74).

vi Crystal Composition

One important feature of antimony telluride has still to be explained in this review. This is the high density of current carriers in crystals grown from melts of stoichiometric composition (26, 42-45). A similar effect is seen in both bismuth telluride and bismuth selenide (26). The reason for this was demonstrated by Offergeld and van Cakenberghe (84) who showed by differential thermal analysis that the congruently melting compounds do not have the stoichiometric composition. Instead they have an excess of the metal. These excesses are

0.4 atomic % (2.1×10^{20} atoms/cc.) in Sb_2Te_3,
0.065 at. % (3.1×10^{19} atoms/cc.) in Bi_2Te_3
and 0.02 at. % (1.05×10^{19} atoms/cc.) in Bi_2Se_3.

The excess atoms act as a doping agent, giving the large carrier densities. The high degree of degeneracy of antimony telluride, compared with the other compounds, is thus accounted for.

It is important to know how the extra atoms are incorporated into the crystal lattice. Three of the mechanisms available involve randomly distributed point defects: a the metal may occupy interstitial sites, b metalloid vacancies may be formed or c metal atoms may substitute for a small proportion of the metalloid. In cases a and b the metal, being the more electropositive element, would act as a donor, in case c as an acceptor (it has fewer valence electrons). The p-type conductivity of the tellurides can be explained on the basis of point defects only if the substitution mechanism is operative. (A different type of mechanism is discussed below.) Further evidence for the substitution mechanism in bismuth telluride was found by Miller (85) from accurate density measurements. (Bi_2Se_3 is normally n-type and mechanism a or b is

presumably correct.) In the case of substitution, if the excess atoms were added to a stoichiometric crystal, only $^3/_5$ of them would occupy tellurium sites and contribute current carriers (86). Using the anisotropy factor given by Katsugi (62) the Hall coefficient parallel to the cleavage plane is then calculated to be 0.028 cc./coul. for antimony telluride. The measured value is about 0.06 cc./coul. (figure 1). The reason for the discrepancy is not known.

Delavignette and Amelinckx (87) observed large dislocation loops in the basal plane of antimony telluride, presumably in the low energy $Te^{(1)}$ planes. The total area enclosed by the loops varied with the degree of non-stoichiometry and it was suggested that this is the non-stoichiometric mechanism in the compound. A similar effect was <u>not</u> found in bismuth telluride. The absence, within a loop, of one of the $Te^{(1)}$ layers would give the layer structure the form

$$-Te^{(1)}-Te^{(1)}-M-Te^{(2)}-M-\underline{Te^{(1)}}-M-Te^{(2)}-M-Te^{(1)}-Te^{(1)}-.$$

It is seen that the central $Te^{(1)}$ atoms now must form six bonds, instead of three as before. There is now a deficiency of electrons in the structure, which becomes p-type, as observed. Unfortunately this possibility cannot be tested against the Hall coefficient measurements as the

authors gave no data on the total area of loop per unit volume of crystal as a function of the composition.

vii Other Properties of Antimony Telluride

Before passing to a discussion of the antimony-tellurium phase diagram, which is relevant to the previous section, we mention the remaining measurements on the compound, Sb_2Te_3.

The heat of formation of the material was investigated by Gerasimov (88) and by Howlett (81). Their results agreed within experimental error, giving a best value of -2.70 kcal./gm.atom. This indicates that the compound has fairly low stability. Howlett found the melting point to be 618.5°C and noted the existence of pre-melting phenomena in a range of 30° below this temperature. These effects may be due to decomposition of the specimen.

Koren and Sirota (89) studied the formation of antimony telluride layers on the surface of single crystals of antimony exposed to tellurium vapour. They obtained the values of the relevant diffusion coefficient, which is probably that of tellurium in the compound. At 500°C this coefficient has a value about 10^{-10} cm^2./sec.

Horne (90) estimated the equilibrium constant for

hydrolysis of the compound to be 10^{-8}, indicating stability under atmospheric conditions.

Delavignette and Amelinckx (91) observed extensive dislocation networks in both Bi_2Te_3 and Sb_2Te_3 by transmission electron microscopy. (These networks are not to be confused with the dislocation loops described in section vi.)

2.5 The Antimony-Tellurium Equilibrium Diagram

The diagram describing the structures adopted by a combination of elements as a function of composition and temperature is an important piece of information; it provides a guide in the preparation of materials and assists in the interpretation of their properties. However, a true equilibrium diagram tells nothing about non-equilibrium transition structures which, particularly at low temperatures, may be very long lived and have at times been mistaken for the equilibrium phases.

The recently published (38, 92, 93) phase diagrams for the antimony-tellurium system show marked differences in the region from 0 to 60 at. % Te (figures 6-8). The diagram of

Hansen (92) (figure 6) is his summary of work prior to 1958. This early work was by no means self-consistent, however. Fay and Ashley (94) considered alloys between antimony and its telluride to be homogeneous. This was confirmed by electrical (54, 56, 95) and magnetic (96) measurements on the alloys. Pelabon (97) verified Fay and Ashley's form for the liquidus. Konstantinov (98) concluded, however, that a eutectic was formed between 0 and 60 at. % Te. The work of Kimata (99) supported this. Hansen (92) accepted the latter view. Abrikosov's phase diagram (93) (figure 7) is nearer to that of Fay and Ashley in that there are shown phases of wide homogeneity ranges. The stable phases are centred roughly on the compositions Sb_7Te_3 (or Sb_2Te), SbTe and Sb_2Te_3. The latter phase, in which we are chiefly interested, has a very narrow range of homogeneity. The thermoelectric power was measured by Abrikosov, with results very similar to those mentioned above, and were taken by him in support of his diagram. The specimens were cast, annealed for several months, and examined for their microstructure. The observation of a eutectic by Konstantinov (98) was explained by Abrikosov on the basis of non-equilibrium crystallisation. Similar wide composition

ranges for intermediate phases were found, using similar techniques, in the bismuth-tellurium and bismuth-selenium systems (100).

Abrikosov (101) later investigated in greater detail the part of the phase diagram near 60 atomic % tellurium. His results are shown in figure 9. Specimens were quenched from the liquid state and their microstructures examined. The phase diagram agreed with that found previously (93) but not with the data of Offergeld (84).

Brown and Lewis (38) pointed out that there is no guarantee that Abrikosov's specimens ever reached equilibrium. They formed specimens by a liquid-solid reaction at a temperature just above the solidus. Single phase specimens were obtained in regions thought by Abrikosov to be two phase (figure 8). A range of homogeneity spreading from 11 to 60 atomic % tellurium was found. The lattice parameters varied smoothly, and nearly linearly, within this phase. The extrapolation of the curves to the composition of pure antimony gave very nearly the lattice parameters of this element. The antimony phase and the intermediate phase are thus related and it is possible that the single phase region actually extends

continuously from 0 to 60 atomic % tellurium, as postulated by Fay and Ashley (94).

There are a priori reasons why appreciable non-stoichiometry may appear in the antimony-tellurium system. The main consideration in forming non-stoichiometric phases is that the energy of formation of the relevant type of point defect should be small. The chief factors contributing to this energy have been listed by Anderson (103). In the present case excess antimony would probably be accommodated by a substitution mechanism so that for wide ranges of non-stoichiometry the ionic types ought to be similar, in particular as regards size (to minimise elastic energy changes) and electronegativity (to minimise electronic energy changes). Furthermore, the possibility of a valency change of either or both elements present helps to maintain charge neutrality. Antimony and tellurium largely fulfil these conditions. The variously defined atomic and ionic radii agree within a few percent. In addition, both elements possess multiple valence states.

The properties of the intermediate phases have been very little studied, except for the extreme tellurium-rich composition, nominally Sb_2Te_3. X-ray diffraction patterns

for three compositions were given by Abrikosov (93) and lattice parameters by Brown (36). Stasova (104), from a study of minute single crystals, showed that material of composition Sb_2Te has a space group probably either D^3_{3d} or C^1_{3v}, very similar to that of Sb_2Te_3. The lattice parameters found by Stasova do not agree well with those given by Brown (36).

The same type of similarities were observed across the bismuth-tellurium system (36, 104, 105) and the bismuth-selenium system (106).

The electrical properties of the antimony-tellurium system have been studied exclusively on polycrystalline specimens and as subsidiary experiments to phase diagram determinations. The results (54, 56, 93, 95, 107) are shown in figures 10 and 11. In view of their inconsistency, due presumably to the apparent difficulty of preparing homogeneous specimens they are not a good basis for interpreting the electrical properties. It does appear, however, that the thermoelectric power is positive in the whole composition range.

Jäschke (50) and Liebe (45) have studied the electrical properties of single crystals of Sb_2Te_3 doped with excess

tellurium, so as to obtain more nearly intrinsic material. Eichler (47) studied corresponding polycrystalline material. Their results are given as a function of the composition of the melt from which the specimens were formed. In view of the uncertainties regarding the phase diagram it is difficult to relate this composition to that of the solid.

2.6 Conclusions

From this summary it may be seen that there is some lack of understanding of the properties of antimony telluride and the related alloys. Some problems of particular interest may be framed in the following questions. What is the mechanism by which the excess antimony is incorporated into the crystal and which positions in the lattice does it occupy? How does it affect the bonding in the compound, or, in what way are the electronic properties altered?

The present investigation was designed to make progress towards answering these questions.

C H A P T E R I I I

P R E P A R A T I O N O F S P E C I M E N S

CHAPTER III

PREPARATION OF SPECIMENS

3.1 Preferability of Using Single Crystals

An important factor contributing to the rapid development of solid state physics during recent years has been the extensive use of single crystals of the materials under investigation. The difficulties of the theoretical investigation of the properties of solids are such that any reduction in the number of variables to be considered is very welcome. The elimination of grain boundaries, with their attendant discontinuity in the crystal structure, is thus of considerable importance in checking the agreement between theory and experiment. In some cases, e.g. antimony telluride, the use of single crystal material is essential if anything approaching a true picture of the properties of the material is to be found. Such materials are anisotropic; some or all of their properties are a function of the crystallographic direction in which they are measured. The tensors relating to each property of such a body cannot be found from measurements on randomly oriented polycrystalline specimens as these can give only an average of the tensor components (an average with unknown weighting factors).

In addition to the problems raised by the misorientations introduced into crystal lattices by grain boundaries, other effects are caused by the properties of the boundaries themselves. The mismatching of the atomic planes at a grain boundary causes the chemical bonds of the atoms near the boundary to be either strained or to be left 'dangling'. Such effects cause an increase in the internal energy of the crystal. The transformation kinetics of polycrystalline and monocrystalline specimens with respect to a second phase may thus be different. In addition the 'dangling' bonds at the interface act as electron traps. The boundary thus becomes electrically charged relative to the remainder of the crystal and affects any property of the material which involves the movement of charge. Such properties include electrical and thermal conduction and the motion of dislocations, which are generally charged in non-metals, also due to dangling bonds.

The mechanical strength of crystalline solids is determined mainly by the dislocation density and mobility. The dislocation mobility is decreased by the presence of grain boundaries; hence normal polycrystalline metals exhibit greater strength than single crystals. When the dislocation density is very low, as in metal whiskers, or dislocation motion is impeded, e.g. by solute atoms, even greater strength is shown. In single crystals, dislocation

motion is comparatively free and such crystals are frequently very soft. This is the case with antimony telluride. The energy of formation of dislocations having their Burgers vector in the cleavage plane is small; there are no strong chemical bonds to be broken. For the same reason the dislocation mobility is high. For the main possible use of this material, thermoelectric refrigeration, polycrystalline specimens can be used without loss of efficiency while maintaining good mechanical strength. For the determination of the material's properties, however, the use of single crystal material appears to be very desirable (see previous chapter) despite the disadvantage of great fragility.

It was hoped in the present work to investigate crystals over a wide range of composition. The growth of massive, highly non-stoichiometric single crystals did not seem feasible. Certainly any crystals produced by normal techniques would be very inhomogeneous. The uncertainties of the phase diagram were a further complication (figures 6-9). Single crystals of peritectically melting material (figure 7) are difficult to produce (108). It was decided to try to produce non-stoichiometric material as layers on the surface of nearly stoichiometric Sb_2Te_3 crystals. This was to be accomplished by diffusion processes. The crystal growing problem was thus reduced to that of obtaining crystals of the compound material.

3.2 Single Crystal Production

i Growth Techniques

Many methods have been used to produce large single crystals (109). The growth of crystals from aqueous solutions is well known but is inapplicable to metallic systems. A similar approach is to use crystallisation from other solvents. For example, Goss (110) has grown silicon single crystals from a saturated solution of silicon in tin. Again, a solution of a solid in a suitable gas, or even in a vacuum, may be used for materials which sublime or have sufficiently high vapour pressures. Zinc sulphide (111), lead selenide (112) and films of germanium (113) are among the single crystals produced by this method.

In contrast to the above techniques, which involve a net transfer of material during the growth process, are the methods involving simply temperature gradients in a specimen of homogeneous composition. In these techniques part of the specimen is maintained in a molten state and the position of the interface between solid and liquid is uniformly moved so as to increase the volume of the solid. Under suitable conditions (to be discussed later) the solidifying material has single crystal form. The chief variants of this method are the Czochralski and Bridgman techniques and zone melting.

The Czochralski technique (114) was devised to draw single crystal metal wires from a pool of molten metal. A small 'seed' crystal of the substance is lowered to touch the surface of a pool of molten material held just above the melting point. The crystal is then raised in such a way that the liquid-solid interface is roughly stationary. The resulting single crystal has the same orientation as the seed. The modern, highly refined, 'pulling' techniques are used in the semiconductor industry for the production of large crystals of germanium and silicon (115).

The technique devised by Bridgman and developed by Stockbarger (116) consists of lowering a melt through a sharp temperature gradient. The temperature gradient is usually formed by using separate furnace windings with a baffle plate between them which fits the crucible closely.

The method of zone melting is commonly used to obtain materials, particularly semiconductors, of high purity (117). It is similar in configuration to the two previous methods. The material is placed in a long horizontal crucible and a molten zone is made to pass along it. The purification process depends on the different concentrations of impurity in liquid and solid phases in thermodynamic equilibrium with each other; the impurity generally tends to collect in the molten zone and is carried to one end of the crucible. Further, if care is taken in the control of conditions at

the freezing liquid-solid interface, a single crystal can frequently be grown, particularly if a seed crystal is used to initiate the growth. Purification by zone melting has been applied to a wide variety of materials but for the production of single crystals the method is less generally useful, due mainly to the effects of the contact between the specimen and the crucible wall. These effects include the introduction of impurities and the mechanical forces acting on the specimen during crystal growth. In suitable cases, however, the method has the advantages over the Czochralski technique that the apparatus is simpler and that some of the optimum growth conditions are easier to obtain and over the Bridgman technique that rather more of the growth parameters may be varied.

The methods involving growth at the liquid-solid interface have been used mainly for preparing crystals of metallic and semiconducting substances. In recent years, however, crystals of other types of materials, notably organic compounds and refractory oxides, have been successfully grown by these methods (118).

ii Control of Crystal Growth

The requirements for the growth of single crystals of good quality are similar for all techniques. The main considerations relevant to the present case are as follows:-

a There is a lower limit to the temperature gradient at the freezing interface. This gradient must be sufficient to conduct away the latent heat released on solidification.

b The velocity of the freezing interface must not be too large.

c The smallest useful velocity for the molten zone is set by the thermal stability of the apparatus.

d Mechanical strains due to thermal expansion limit the size of the temperature gradients.

e The effects of the roughness of the crucible wall in nucleating spurious crystal growth should be eliminated.

f Excessive vaporisation of the material and, in the case of some compounds, decomposition must be prevented.

These conditions are now discussed.

A primary condition for effective single crystal growth is the avoidance of supercooling of the liquid phase near the growing boundary. This supercooling, which causes stray nucleation, can arise in the following way. On solidification the latent heat of fusion of the solid is given up and generates thermal gradients in the material. The gradient on each side of the boundary is such as to cause a heat flow from the boundary. These thermal gradients are (approximately) additive with the gradients set up by the external heaters. If supercooling is to be avoided, the resulting total gradient in the liquid must

transfer heat towards the freezing interface. Thus the lower limit to the temperature gradient at the boundary depends on the rate of evolution of the latent heat. This rate is proportional to the velocity of the interface. Hence conditions a and b above are related from this viewpoint.

Frequently the composition of the freezing solid depends on the characteristics of diffusion in the liquid phase (119, p. 161). The velocity of the growth boundary (condition b) is clearly of importance in this case. In a pure, congruently melting material such effects should be small. Generally, however, some means of agitating the liquid is desirable; in the Czochralski method the growing crystal is rotated.

The small growth rate must hold at all times. It is insufficient that merely the average velocity of the interface should be small. The mechanical system causing motion of the interface must therefore operate smoothly. Likewise, rapid temperature fluctuations of the system must be avoided since these also lead to varying interface velocities. This effect is minimised if a large temperature gradient at the growing surface is used, in agreement with condition a. The mean interface velocity must clearly be greater than the velocity fluctuations due to temperature changes (condition c). A stabilised power supply is necessary.

The temperature gradient must not be too large, however, or excessive thermal stresses are set up in the grown crystal with consequent deterioration of the crystal quality (120) (condition d).

A uniform single crystal is produced only if the growth conditions are the same over the complete liquid-solid boundary, i.e. the boundary should be plane. This further helps to alleviate thermal stresses in the solid. In cases such as zone melting, where the liquid is in contact with the atomically irregular wall of the crucible, it is usually desirable for the interface to be very slightly convex towards the liquid. By this means the results of any stray nucleations at the crucible wall are eventually eliminated since near the wall the direction of growth at the interface has a component directed towards the wall (condition e).

The considerations outlined above are important in all cases. In particular cases other factors must also be taken into account. Many compounds of interest (including antimony telluride (26)) decompose at temperatures near the melting point, the rates of evaporation being different for the components. Unless steps are taken to eliminate the evaporation there is a large loss of one constituent from the specimen resulting in a non-uniform crystal of uncontrolled composition. This effect can obviously be prevented by maintaining a suitable pressure of the volatile

component above the material (121). Such conditions may be attained with the specimen in a sealed container at a high temperature. The volatile component then cannot condense on the wall of the container. Alternatively, a sample of the volatile constituent may be placed in a section of the tube where the temperature is lower than, and independent of, the temperature of the main specimen. The lowest temperature in the sealed tube then determines the vapour pressure of the evaporating element.

The experimental investigation of actual growth conditions is generally difficult to perform accurately. The thermal gradients cannot be measured accurately without appreciable disturbance of the temperature distribution.

iii Previous Work on Growth of Sb_2Te_3 Single Crystals

Several workers have used single crystals of antimony telluride for their work on the transport properties of the material. Zone melting was the method most used to produce the crystals (26, 29, 42, 43, 60) with, usually, a high ambient temperature. Speeds between 2 and 15 mm./hour have been used, with temperature gradients of order 50 ^{o}C/cm. The Bridgman (45, 59) and Czochralski (50) methods have also been used.

The zone melting technique appears to be suitable for single crystal growth.

iv Construction of Zone Melter

A zone melting furnace was constructed taking into account the problems outlined in section ii. The design is shown diagrammatically in figure 12. An attempt was made to perform the growth process in an environment having good cylindrical symmetry.

The specimen, A, of length about 40 cms., was contained in a sealed Vitreosil tube, B, of 1 cm. bore. A high ambient temperature for the specimen was maintained by eight heater wires, C, connected in series stretched parallel to the specimen tube. The ends of the wires were supported on Sindanyo, D, one of the supports being spring loaded, E, to allow for the thermal expansion of the wires. When the specimen tube was in position, the sprung Sindanyo support was given a single turn. The heater wires then came into good thermal contact with, and were supported by, the specimen tube. Each wire consisted of several strands twisted together giving a large surface area to the heater wires. The dissipation of heat by the wires was thus eased and the required power input was obtained with lower temperatures of the wires. The longitudinal arrangement of the heater wires gave exactly the same generation of power per unit length in each section of the furnace. The specimen was thus maintained at a uniform temperature. The length of the furnace was 52 cm.; the ends of the specimen

were 6 cm. inside the furnace and were not appreciably cooler than the centre sections.

Thermal insulation of the heaters from the atmosphere was achieved by placing around the specimen tube and heaters a transparent Vitreosil tube, F, (bore 15 mm.) which supported a layer of alumina cement, G, of thickness 2½ mm. The alumina layer was made of uniform thickness by grinding it down using a lathe before it was fired. In addition the layer had a uniform slit about 6 mm. wide cut in it along the tube. This allowed for observation of the tube interior. The figure of 2½ mm. for the thickness of the alumina had been roughly calculated previously from a numerical solution of the equation of heat flow.

The hot zone required for zone melting was created by a short furnace (not shown on the diagram) of length 7½ cm. which slid on silica rods, H, and surrounded the alumina insulation. This furnace was moved by a constant horizontal force supplied by a weight and pulley. The rate at which the weight fell and the furnace moved was controlled by a sychronous motor acting through a high gear ratio. By interchanging the gears various speeds between 9 and $^{1}/_{9}$ cm./hour could be obtained.

Provision was made for the specimen tube to project into a small auxiliary furnace to allow control of the vapour pressure above the growing crystal as outlined in a previous section. This facility was not needed, however.

The frame on which the furnace was mounted could be tilted so as to eliminate the mass transfer along the tube during the zoning process due to the different specific volumes of the liquid and solid phases.

Each furnace winding was supplied with power from a separate variable autotransformer. These were fed from the mains via a constant voltage transformer which reduced mains voltage fluctuations to less than 0.1%. The degree of stability of the temperatures given by this power supply was found to be sufficient for crystal growth.

In order to avoid undue thermal stresses to the grown crystal provision was made to cool them to room temperature over a period of about 6 hours. When the moving furnace ended its run it operated a microswitch which switched off the control motor and caused a second motor to turn the autotransformer voltages gradually to zero.

iv Preparation of Specimens for Zone Melting

The materials used in the crystal growth were 99.999% pure antimony obtained from Koch-Light Laboratories Ltd. and 99.999% pure tellurium obtained from either Koch-Light or from Johnson-Matthey and Co. Ltd. The Johnson-Matthey tellurium was visibly covered with a surface layer of some impurity, probably tellurium oxide. This was largely removed by mechanical scraping. To realise the full

purity of the tellurium, the material from both sources was distilled twice at a temperature just above the melting point in an atmosphere of air at a pressure of about 10^{-3} torr. Such a process has been shown (122) to produce a big reduction in the impurity concentration of oxygen and other impurity atoms.

Following the distillation, ingots of each element were made by placing lumps (not powder) of the elements in 9 mm. bore tubes, flushing with high purity argon, evacuating the tube and sealing it. The lumps of material were then melted to form ingots, special care in this operation being needed in the case of antimony since this element expands on freezing. The ingots had masses rather greater than would be needed for the production of a specimen for the zone melting.

The crucible tube which was to contain the specimen during the zone melting was of 1 cm. bore transparent Vitreosil. The wall thickness was about 1.2 mm. and the tube was chosen as straight and as uniform in bore as possible. It was cleaned with rinses in aqua regia and acetone and was then thoroughly washed with distilled water. The tube was then partially sealed off near one end. The method employed for sealing was to insert a silica slug of 9 mm. diameter and about ½ inch length into the bore and then to fuse this to the tube wall. By this means the outer

radius was kept nearly uniform along its whole length and the danger of an uncontrolled collapse when sealing under vacuum was avoided. A disadvantage of this method was the inevitable reduction in the vacuum pumping speed but this was unimportant in the present case. A partial seal was made by fusing only one side of the tube to the silica slug.

The inside of the specimen container was coated with a layer of pyrolytic carbon. The layer was just opaque and was strong and smooth. It was made by moving the tube slowly through a furnace at about 1200°C while argon saturated with ethyl alcohol passed slowly through it. Following this a thin strip of this coating along one side was burned away. This formed a window so that the interior of the crucible could be seen. In addition the carbon was burned from the places where the tube was to be sealed.

Portions of the ingots of the elements, in the proportions required to form congruently melting antimony telluride (84), were sealed into the crucible under a pressure of about one torr of pure argon. Care was taken to avoid scratching the graphite coating. The elements were made to react together as gently as possible and the tube was sealed in a further position, such that the specimen was contained in the minimum convenient length of tube (about 40 cm.). The total specimen weight was about 160 g.

The specimen was placed in the zone furnace and was

maintained at a temperature above that of melting for 48 hours to ensure homogeneity. It was then slowly cooled and was zone melted several times to obtain exactly the congruently melting composition over most of the specimen and to ensure freedom from bubbles, etc. of the ingot. The treatment of the metal was watched through the windows in the alumina and graphite layers, which were situated vertically above the sample so as to disturb the thermal symmetry as little as possible. Since thermal radiation could escape comparatively easily through this window the top of the specimen tube tended to have a temperature lower than that of the specimen. The use of an atmosphere of argon above the metal (as previously mentioned) eliminated any possibility of condensation of metal vapour on this part, presumably by increasing the thermal coupling between the tube wall and the specimen.

vi Crystal Growth

The main factors to be controlled during the growth of crystals of compound substances are, as shown in section ii, the speed of growth, the temperature gradients at the liquid-solid interface, the shape of the interface and the vapour pressure of one of the constituents above the compound. In the present case independent control of the last quantity was deemed unnecessary. During growth, vapour

from the metal could not condense on the tube wall and since the volume of the space above the specimen was small the composition of the solid remained practically unchanged.

The independent quantities, the interface curvature and the temperature gradients at the interface, could both be fixed as desired using the independent controls of the ambient temperature furnace and the small zone furnace. The shape of the growing interface is determined largely by its position relative to the zone furnace. If we assume the interface to be virtually in a state of equilibrium then the equation of temperature distribution inside the material is

$$\nabla . (k \nabla T) = 0 \qquad (3.1)$$

where T is the temperature and k the thermal conductivity, assumed isotropic. In cylindrical coordinates, taking the axis of the tube as the z-axis and assuming radial symmetry, this equation becomes

$$k\left[\frac{1}{r}\frac{\partial}{\partial r}\left[r\frac{\partial T}{\partial r}\right] + \frac{\partial^2 T}{\partial z^2}\right] + \nabla k \cdot \nabla T = 0 \qquad (3.2)$$

For the case of a plane isothermal surface (in which we may situate the growth interface) we have

$$\frac{\partial T}{\partial r} = 0$$

and hence

$$k \frac{\partial^2 T}{\partial z^2} + \frac{dk}{dz} \frac{\partial T}{\partial z} = 0 \qquad (3.3)$$

since k changes only across the interface. The second term in this equation represents the change of thermal gradient across the interface which is necessary for continuity of heat flow. At points near the interface the isothermal surfaces are nearly plane but here $\frac{dk}{dz} = 0$. Then, near a plane interface

$$\frac{\partial^2 T}{\partial z^2} = 0 \qquad (3.4)$$

The physical meaning of this result is as follows. No heat can flow parallel to an isothermal surface in its vicinity since otherwise there would be a temperature gradient in this direction and the surface would not be isothermal. Thus all heat flow near an isothermal surface must be normal to it with no lateral gain or loss of heat. Hence the temperature gradients near the surface must be constant, i.e. $\frac{\partial^2 T}{\partial z^2} = 0$ where z is the direction of the surface normal.

If, as is the case here, we require the growth interface to be slightly convex to the liquid, then near the interface the temperature must be slightly higher near the

outer surface than on the axis of the specimen, i.e. at the surface $\frac{\partial T}{\partial r}$ is negative and there is a lateral flow of heat into the specimen. Since, by symmetry, we must have $\frac{\partial T}{\partial r}$ (r = 0) = 0, it follows that near the interface $\frac{\partial^2 T}{\partial r^2}$ is positive. Then, from equation 3.2, in regions where $\nabla k = 0$ (outside the interface), we have $\frac{\partial^2 T}{\partial z^2}$ is negative.

The above condition on the most suitable situation for crystal growth has additionally the following advantage. Since the temperature gradients near the interface are constant to the first order of approximation a small change in the length of the molten zone during growth has no effect on these temperature gradients and the crystal grows under steady conditions. The requirements for long term temperature stability of the apparatus may then be relaxed somewhat.

The temperature distribution in the specimen near the zone furnace has the approximate shape shown in figure 13. The horizontal axis represents the distance from the centre of the zone furnace, the vertical axis the temperature in excess of that maintained by the main heater called the ambient temperature. The length of the zone furnace is 2L. With the melting temperature T_m corresponding to the point of inflexion of the graph, the condition for effective crystal growth is fulfilled and the required length of the molten zone is 2s. The graph does not show the

discontinuity in slope at the melting temperature caused by the different thermal conductivities of solid and liquid.

Clearly the thermal gradient at the interface may be altered while maintaining the condition $\frac{\partial^2 T}{\partial z^2} = 0$ by simultaneously raising the ambient temperature and decreasing the zone furnace power, or vice versa.

Thus to avoid a completely empirical determination of the practical conditions for crystal growth the temperature distribution in the specimen under at least static conditions must be found. As mentioned previously, this is very difficult. In the present case, in order to make some use of the considerations given above, the following very crude method to find the temperature distribution was employed. If the ambient temperature, T_a, is varied by small amounts the temperature profile of figure 13 does not change appreciably, except that the melting point, T_m, moves along the curve and the length of the liquid zone varies accordingly. The length of the molten zone as a function of the power input to the ambient temperature furnace was found for constant power input to the zone furnace. The scale of temperature was found by determining the input power to the main furnace which just produced a molten zone ($T_o = T_m$) and that which melted the whole specimen ($T_a = T_m$). On the assumption that the furnace temperatures were proportional to the power input the constant difference $T_o - T_a$ could be

found and the temperature gradients determined. With these results the furnace input powers to give a zone length of 4 cm. (compared to the zone furnace length of 7½ cm.) and a temperature gradient at the interface of about 70 ^{o}C/cm. were chosen and were used successfully. Under these conditions the maximum temperature in the hot zone was about 20^{o}C above the melting temperature and the ambient temperature was about 400^{o}C.

The optimum growth speed was found empirically subject to the condition that the rate of generation of the latent heat should be much less than the heat carried by the temperature gradient at the interface. A rate of 2½ mm./hour was found to be suitable.

The specimens resulting from growth under these conditions were usually, but not always, mainly single crystal material. The polycrystals generated from the first material to freeze were observed to grow out of the crystal, due to the convex growth interface, in about the first 10 cms. The last five cms. was polycrystalline also, presumably due to the disturbance of growth conditions by the discontinuity at the end of the sample. The cleavage plane of the single crystal portion was always within a few degrees of the furnace axis. This situation is to be expected since the thermal conductivity along the specimen axis is then greatest, the temperatures reached in the

specimen are minimised and the system is thermally stable. Additionally, the cleavage plane was always within 30° of the horizontal. This indicates some lack of radial thermal symmetry under the growth conditions.

Occasionally small angle boundaries were seen in the otherwise single crystal section. These boundaries did not affect the cleavage of the crystals and such specimens were used in the same way as more perfect ones.

3.3 Further Preparation

After growth the crystals were left in their silica tubes until required, when they were sectioned transversely using a Capco diamond saw. For support during cutting the crystals were left in the growth tube. Despite this, some of the cut sections were cracked into two on a single cleavage plane, apart from the many small cracks at the cut surface.

For further treatment the crystal sections were mounted in plastic to prevent cracking and the sawn faces were ground on fine silicon carbide paper, removing about ½ mm. of material. By this means most of the surface cracks were eliminated. Immersion for about one minute in an etching solution (1 HCl/2 HNO_3/2 H_2O) removed the remaining damaged surface layer (about 100 microns thick) and produced a good

single crystal surface which was usually quite flat. Any cracks on the cleavage planes were preferentially attacked by the acid and became easily visible. In this way one was reasonably sure that a specimen was, as a whole, free from cracks. X-ray diffraction photographs taken by the Laue method showed single crystal structure.

Attempts to produce a single crystal surface by etching the as-sawn specimen face were not successful; any deep cracks initially present on the surface were propagated through the body of the crystal. This is probably due to bubble formation inside the cracks resulting from the acid attack.

The preparation of good crystal surfaces in the cleavage plane is trivial. The cleavage is well performed using Sellotape, or similar material.

The plastic mounts used during this preparation could be removed by solution in trichloroethylene.

3.4 Diffused Specimens

Several types of system are available for the formation of the diffused specimens.

a The antimony telluride crystal may be placed in direct contact with solid antimony (e.g. 123). Since the diffusion of fairly large amounts of antimony was

anticipated, such a configuration would lead to uncertainties, after diffusion, of the original interface position. Furthermore, considerable difficulties in sectioning to expose the diffused surface could be introduced.

b Diffusion from a liquid phase could remove these obstacles but involves a better knowledge of the phase diagram than is currently available.

c A third possibility is to place the antimony telluride crystal in antimony vapour, derived from the element at a temperature in general different to that of the compound. The main transport is probably that of tellurium out of the compound and into the antimony, which acts as a tellurium sink. The antimony should thus be finely divided so as to present a large surface area. Systems of this type have been much used to obtain small deviations from stoichiometry in semiconductors (124).

A disadvantage of the method when large diffused concentrations are desired is the low diffusant concentration in the vapour phase.

d A system similar to the above is that where the crystal evaporates into a vacuum. The evaporated material may be removed from the system using a cold finger or similar arrangement. The evaporation rates of the constituent elements are generally unequal (e.g. 125)

initially and the surface composition changes until atoms are removed in the stoichiometric ratio of the compound. Meanwhile diffusion occurs in the concentration gradient within the specimen. Eventually a state of dynamic equilibrium is attained (126).

In the present study systems c and d were used. The specimens, with surfaces prepared as described, were placed in silica tubes which were flushed with high purity argon, evacuated to 10^{-4} mm. mercury, and sealed. For case c a small amount of powdered antimony was also placed (not in direct contact with the crystal) in the capsule which was then maintained, in an isothermal state, at high temperature. In case d the capsule volume was larger and the evaporated material condensed on one end of it which projected outside the furnace. The highest safe annealing temperature was 540°C (see figures 6-8); above this there was a danger of the specimen melting. The highest temperature actually used was 500°C, which was maintained within $\pm$ 1°C. Estimations of the diffusion times required were obtained using coefficients found for the homologous compounds Bi_2Te_3 and Bi_2Se_3 (127, 128) in addition to the data of Koren and Sirota (89).

It was not found possible to prepare diffused crystal faces other than cleavage faces. The other surfaces were much pitted. Following diffusion the specimens were again

mounted in plastic with the cleavage face exposed and it was verified by X-ray diffraction that the monocrystalline character of the surface was preserved.

CHAPTER IV

EXPERIMENTAL TECHNIQUES

CHAPTER IV

EXPERIMENTAL TECHNIQUES

4.1 Introduction

The various measurements which have been made previously on highly non-stoichiometric antimony telluride were discussed in Chapter II. They were seen to be inconsistent (e.g. figures 10 and 11). In the present work several properties of non-stoichiometric material were measured. The properties chosen for measurement were among those generally considered in this type of investigation, the electrical conductivity, Hall coefficient, thermoelectric power and crystal structure. Where possible, advantage was taken of the single crystal form of the specimens. The nature of the samples, an inhomogeneous layer on the surface of a large, uniform crystal, necessitated a new method of analysis for measurement of the electrical conductivity of such diffused specimens. This method, including the new theory, is discussed first, and is followed by details of the other measurements, which were of standard types.

4.2 Electrical Conductivity Measurement - Review of Methods

For the present experiments a method was required which would determine the variation of two conductivity components in an anisotropic, inhomogeneous sample.

The various methods of electrical conductivity measurement may be classified by the number of contacts which must be made to the specimen. Various contactless methods have been employed, involving the effects of currents induced in a specimen by a varying electromagnetic field. Both low frequency (129) and high frequency methods (130) have been used. The only contactless method so far described which may meet the present requirements is that of Johnson (131). This method utilises the electromagnetic 'skin effect'. The skin depth varies with frequency. From the dependence of the electrical resistance on frequency, the conductivity profile can be found. The necessary frequency would be about 10^{10} or 10^{11} c.p.s. in the present case, however, which corresponds roughly to the carrier relaxation time. The method is therefore not applicable to the determination of the d.c. conductivity.

A single contact method has been used (132, 133) to measure the resistivity of doped silicon to an accuracy of 10%. The spreading resistance of a small area contact is measured. (The spreading resistance is the potential difference per unit current between the electrode, assumed

to be an equipotential region, and a distant point in a semi-infinite medium.) A second, large area, contact of small resistance is, of course, also required. The spreading resistance depends mainly on the conductivity in the immediate vicinity of the contact. Thus, using a small contact, very small regions of a specimen can be investigated. The method cannot detect anisotropy, however. Furthermore, it is assumed that the geometry of the contact area is unchanged from one experiment to another. This condition could not be achieved with antimony telluride using the necessary small contacts. The material was heavily deformed and cracks appeared.

There remain the various multiple contact methods which are forms of the four probe method, now described. Current flows in a sample between two electrodes and the resulting potential difference between two other electrodes is measured. The resistance characteristic thus found, with the probe and sample geometries, determines the conductivity (assumed uniform). The contacts used are usually small compared with their separation. Tables of the geometrical factors have been published for simple geometries (134). Mircea (135) has derived a general method for calculating these factors. By a simple transformation, to be described later, the method may be applied to anisotropic media (136). The main advantage of the method is the elimination of the

effects of the resistances of the contacts. So long as the output potential can be measured sufficiently accurately, the method is most easily used on high conductivity material (137). The effects of heating, minority carrier injection and current leakage are then minimised.

Many variations of the four probe technique have been used. A very convenient method for finding the conductivity of thin sheet specimens is that of van der Pauw (138). The specimens, of uniform thickness, may have any shape so long as they are singly connected. Electrical connections are made to any four points (A, B, C and D in cyclic order) on the circumference. A resistance $R_{AB,CD}$ is found from the potential difference generated between C and D by a current through A and B. Similarly $R_{BC,DA}$ is found. These two quantities, with the specimen thickness, yield the conductivity of the material in the plane of the sample. From $R_{AC,BD}$, measured both with and without a magnetic field perpendicular to the plane of the specimen, the Hall coefficient may be found.

The four probe method was first devised as a method for measuring the resistivity of the ground (139). An important problem in this context is the determination, using such electrical methods, of the conductivities and thicknesses of the underground rock strata. This situation is very similar to the present one and much of the theory may be used

directly. The chief differences between the two cases are:-

a The geophysical problem is generally concerned with inhomogeneity in the form of a series of discrete layers which are themselves uniform. In the present case there is a continuous variation of conductivity with distance from the surface.

b Due to the small diffusion depths in the present specimens it is not possible to make measurements with probe spacings much smaller than the size of the inhomogeneity. Measurements are restricted to 'large' distances. The reverse limitation applies in geophysics.

c Thin surface layers may be removed from diffused specimens, thus altering the conductivity profile in a known manner. Such an operation is clearly not possible in earth measurements.

The four probe method may be used to find the conductivity profiles for specimens of the type obtained in the present work.

4.3 Electrical Conductivity Measurement - Theory

i Theory of the Potential Distribution in Inhomogeneous Media

The basic problem to be solved is how to find the conductivity variation, $\sigma(r, z, \varphi)$ (r, z and φ are cylindrical coordinates), in inhomogeneous media from

measurements of the electric potential on the surface of the medium. The type of inhomogeneity discussed is that of an isotropic, semi-infinite medium with its surface in the plane $z = 0$, whose conductivity varies only with the depth, z ($\sigma = \sigma(z)$). Stevenson (140) showed the problem to be insoluble for more general types of inhomogeneity if the current electrode is fixed.

With the finite specimens used in practice, two current electrodes must be used, of course. Each current source may be considered as separately generating a potential distribution in the sample. The actual potential distribution is found by addition. Thus in the theory it is necessary to consider only a single current source. The effect of others is easily found.

The fundamental equation for the potential in any medium carrying a current is derived from the conservation of electric charge,

$$\operatorname{div} \underline{j} = 0 \tag{4.1}$$

where $\underline{j}$ is the current density. Using Ohm's law and substituting the negative potential gradient for the electric field,

$$\nabla^2 V + \frac{1}{\sigma} \frac{d\sigma}{dz} \frac{\partial V}{\partial z} = 0 \tag{4.2}$$

for $\sigma = \sigma(z)$. ∇^2 is the Laplacian operator. Putting

$$\frac{1}{\sigma}\frac{d\sigma}{dz} = f(z) \tag{4.3}$$

equation 4.2 is, in cylindrical coordinates

$$\frac{\partial^2 V}{\partial r^2} + \frac{1}{r}\cdot\frac{\partial V}{\partial r} + \frac{\partial^2 V}{\partial z^2} + f(z)\cdot\frac{\partial V}{\partial z} = 0 \tag{4.4}$$

with the boundary conditions

a V is everywhere finite and vanishes at infinity.

b $\frac{\partial V}{\partial z}$ is zero at $z = 0$, except at the electrode.

Equation 4.4 is separable. Putting $V = R(r).Z(z)$ yields Bessel's equation of zero order for R(r). Of the various solutions to this equation only the Bessel function of the first kind, $J_o(\theta r)$, can be made to satisfy the boundary conditions. Z(z) satisfies the equation

$$\frac{d^2 Z}{dz^2} + f(z)\frac{dZ}{dz} - \theta^2 Z = 0 \tag{4.5}$$

which has two solutions. The appropriate solution is that which approaches zero for large values of z. θ is an auxiliary parameter; it is the separation constant of equation 4.4. The potential due to a point source of current on the specimen surface, or to a small hemispherical contact at constant potential is

$$V(r,z) = -Q\int_0^\infty d\theta.J_o(\theta r).\theta.Z(z,\theta)/Z'(0,\theta) \qquad (4.6)$$

Q is the 'source strength' of the current source. It is found by using Gauss' theorem over a small surface enclosing the electrode.

$$Q = I/2\pi\sigma(0) \qquad (4.7)$$

where I is the total current. Only V(r,0) can be measured,

$$V(r,0) = -\frac{I}{2\pi\sigma(0)}\int_0^\infty d\theta.J_o(\theta r).\theta.Z(0,\theta)/Z'(0,\theta)$$

This is usually written as

$$V(r) = \frac{I}{2\pi\sigma(0)}\int_0^\infty k(\theta).J_o(\theta\, r).d\theta \qquad (4.8)$$

The function

$$k(\theta) = -\theta.Z(0,\theta)/\left[\frac{d}{dz}Z(z,\theta)\right]_{z=0} \qquad (4.9)$$

is known as the 'kernel function'. If V(r) is known for all values of r the kernel function can be evaluated using the Hankel inversion formula (141).

$$\frac{I}{2\pi\sigma(0)}\, k(\theta) = \theta \int_0^\infty r.V(r).J_0(\theta r).dr \qquad (4.10)$$

subject to certain restrictions on V(r).
Thus V(r) and k(θ) represent equivalent information and the latter is usually used as a basis for further calculation.

The potential distribution corresponding to a given conductivity variation may be found using equations 4.3, 4.5, 4.8 and 4.9. This is much easier mathematically than the reverse process of finding $\sigma(z)$ from V(r), which is required in practice. As a result an indirect method of interpreting the V(r) curves is in general use in geophysics. In this method a series of standard graphs is computed for predetermined conductivity profiles and the measured potentials are compared with these. The calculated graph of best fit, or an interpolation between some of these graphs, indicates the interpretation to be assigned to the measured curve. To meet all practical requirements a very large number of curves is needed. Various albums of such graphs have been prepared (142, p. 13); to date they refer only to the layer structures relevant in geophysics. Methods of calculating standard graphs for layer structures have been reviewed by van Dam (142). The recent applications of the method in semiconductor research (143-145) have also been of this type; a single homogeneous layer on a homogeneous base medium has been reasonably

assumed for the structure of evaporated layers on conducting substrates. It may be noted that the geometrical factors mentioned in section 4.2 in connection with measurements on homogeneous finite samples are of the same nature as these standard graphs; a conductivity profile is initially assumed (the conductivity is zero except in a certain region of space).

Direct methods of interpretation (i.e. obtaining $\sigma(z)$ from $V(r)$) have been described in a very few cases. Pekeris (146) gave a method suitable for layered structures. The only method apparently suitable for the present case is that of Slichter (147) and Langer (148) which applies to a continuously varying conductivity with at most a single discontinuity. The conductivity profile is determined as a power series in z. Stevenson (140) in a worked example found that the method did not yield a reasonable result. More suitable cases tested, to a higher degree of accuracy in the present work, show the method to be valid within limits. A great deal of calculation is needed to obtain useful results, however. For instance, an analysis performed for the distribution of potential $Vr = 0.3 + 0.7 \exp(-r/\beta)$ determined the coefficients of z^n up to $n = 40$ in the series for the conductivity. The series appeared to possess a radius of convergence of 1.77β, i.e. the series is not valid for larger values of z. Other types of potential distribution gave similar results.

In addition, the application of the Slichter-Langer technique requires chiefly a knowledge of the potential distribution at distances from the electrode less than the mean depth of the inhomogeneity. While this information is easily acquired in geophysical applications it cannot at present be obtained on the specimens under investigation here.

ii New Method of Analysing the Potential Distribution

This section of the thesis presents a method whereby those parts of the potential distribution which can be measured in solid state work may be analysed. It utilises the additional possibility present in this work of the removal of surface layers from the sample.

The section of the potential distribution which is considered to be known is that at distances greater than the mean depth of the inhomogeneous surface layer. The type of inhomogeneity considered is that of a medium with a conductivity profile $\sigma(z)$ where $\sigma(z)$ is everywhere finite and approaches a constant value for large values of z. This is just the sort of profile obtained in diffusion experiments, even when a p-n junction is formed, although the method may not be suitable for the latter case. A further restriction on the form of $\sigma(z)$ appears later, but this does not affect the application to diffusion experiments.

The form of the method consists of measuring the described section of the potential distribution on the specimen surface, removing a thin surface layer, remeasuring the potentials and repeating this process until the effects of inhomogeneity can no longer be detected, i.e. when the potential is proportional to r^{-1}. Whereas the complete knowledge of potentials over a single surface is just enough information to determine the conductivity profile in an isotropic medium (e.g. the Slichter-Langer method), the solution for an anisotropic medium cannot be defined unless other information is available. The present technique in general yields a surplus of information, depending on the accuracy of the measurements. The variation of both conductivity tensor components of an anisotropic medium can be found.

In this section the theory is derived for an isotropic medium. The anisotropic case is treated in the following section. The theory shows how a series expansion for the kernel function may be found in terms of the conductivity variation. Relations between the coefficients of the series are derived. The coefficients may be determined directly from the measurements of potential.

It is most convenient to work with a 'normalised' conductivity variation

$$c(z) = \sigma(z)/\sigma(\infty) \tag{4.11}$$

where $\sigma(\infty)$ is the value of σ for large z. From equation 4.3

$$f(z) = \frac{d}{dz} \log c(z) \tag{4.12}$$

A function is defined (145) by

$$v(z,\theta) = -Z(z,\theta)/\frac{d}{dz}Z(z,\theta) \tag{4.13}$$

Some properties of $v(z,\theta)$ are as follows:-

a Equation 4.5 may be written in terms of $v(z,\theta)$

$$\frac{dv}{dz} - v.f(z) + 1 - \theta^2.v^2 = 0 \tag{4.14}$$

b By comparison with 4.9

$$k(\theta) = \theta.v(0,\theta) \tag{4.15}$$

c For large values of z the potential is not influenced by the inhomogeneity. Then $v(z,\theta)$ approaches the value for the homogeneous case, found from 4.14.

$$\lim_{z\to\infty} v(z,\theta) = \theta^{-1} \tag{4.16}$$

d For at least small values of θ, $v(z,\theta)$ may be written in the form

$$v(z,\theta) = \frac{1}{\theta}(b_0 + b_1\theta + b_2\theta^2 + \dots .) \qquad (4.17)$$

where $b_i = b_i(z)$. This follows from 4.15 and the fact that the kernel, $k(\theta)$, being everywhere finite and continuous, may be expanded as a series in θ.

e From 4.16 and 4.17

$$\lim_{z\to\infty} b_i(z) = 0 \quad , \; i > 0 \qquad (4.18)$$

f The fact that 4.14 is even in θ does not imply that the odd derivatives of v with respect to θ are zero at $\theta = 0$. From 4.17, v is singular at $\theta = 0$.

Substitution of the series 4.17 for $v(z,\theta)$ into equation 4.14 yields

$$\theta + \sum_{i=0}^{\infty} \left[b_i'\theta^i - f(z)b_i\theta^i - \theta^{i+1} \sum_{j=0}^{i} b_j b_{i-j} \right] = 0 \qquad (4.19)$$

The coefficients of θ^i must be separately zero for all values of i.

$$b_i' - f(z).b_i - \sum_{j=0}^{i-1} b_j b_{i-j-1} + \delta_{1,i} = 0 \qquad (4.20)$$

where $\delta_{i,i} = 1$ and $\delta_{i,j} = 0$ $(i \neq j)$. This is a first order, linear differential equation for $b_i(z)$ in terms of the functions $b_j(z)$ with j less than i. It is easily solved using the integrating factor $\exp(\int_z^\infty f(z).dz)$ which is equal to $1/c(z)$ from equation 4.12. For i=0 the solution of equation 4.20 is

$$b_0(z) = c(z) \tag{4.21}$$

where the fact that $k(\theta=0) = c(z=0)$ has been used. For i>0 equation 4.20 may be written as

$$\frac{d}{dz} B_i(z) = c(z).D_i(z) \tag{4.22}$$

where $B_i(z) = b_i(z)/c(z)$

and

$$D_i(z) = \begin{cases} 1-c(z)^{-2} & i=1 \\ \sum_{j=0}^{i-1} B_j B_{i-j-1} & i>1 \end{cases} \tag{4.23}$$

Thus

$$B_i(z) = \int_\infty^z c(z).D_i(z).dz \tag{4.24}$$

for i>0. For i=0, 4.21 gives $B_0=1$.

For example,

$$B_1(z) = \int_{\infty}^{z} (c-c^{-1})dz \qquad (4.25)$$

$$B_2(z) = 2\int_{\infty}^{z} c\ dz \int_{\infty}^{z} (c-c^{-1})dz \qquad \text{etc.} \qquad (4.26)$$

The integrals defining the functions B_i all converge only if $c(z)$ approaches unity for large z as, or more rapidly than,

$$c(z) = 1 + \alpha.\exp(-\beta z)$$

where α and β are any constants satisfying $\alpha>-1$ and $\beta>0$. This condition is fulfilled in allldiffusion experiments into previously homogeneous, effectively semi-infinite media.

We now consider the specimen surface to be in the plane $z=s$. The coefficients in the series expansion of $k(\theta)$ (which is also a function of s) are

$$e_i = b_i(z=s) = c(s).B_i(s) \qquad (4.27)$$

$$k(\theta) = \sum_{i=0}^{\infty} e_i . \theta^i$$

$$= c(s) \sum_{i=0}^{\infty} B_i(s) . \theta^i \qquad (4.28)$$

By differentiation of the functions B_i with respect to s, the following relations may be derived relating the conductivity with the functions B_i for even values of i.

$$\frac{du}{ds} + P_{2i}u = Q_{2i} \quad , \quad i=1,2,3,\ldots \qquad (4.29)$$

where $u = c(s)^{-2}$

and

$$P_2 = \frac{2}{R_2}(R_2'+2) \qquad Q_2 = \frac{4}{R_2}$$

$$P_4' = \frac{2}{R_4}(R_4'-\tfrac{1}{2}R_2^2) \qquad Q_4 = \frac{8}{R_4} B_2$$

$$P_6 = \frac{2}{R_6}(R_6'-R_2R_4) \qquad Q_6 = \frac{8}{R_6}(B_4+\tfrac{1}{2}B_2^2)$$

$$P_8 = \frac{2}{R_8}(R_8'-R_2R_6-\tfrac{1}{2}R_4^2) \qquad Q_8 = \frac{8}{R_8}(B_6+B_2B_4)$$

$$R_2 = B_2'$$

$$R_4 = B_4'-R_2B_2$$

$$R_6 = B_6'-R_2B_4-R_4B_2$$

$$R_8 = B_8'-R_2B_6-R_4B_4-R_6B_2$$

etc. (4.30)

Thus, given the functions $B_{2i}(s)$ (i.e. the variation of the B_{2i} as surface layers are removed), the functions $P_{2i}(s)$ and $Q_{2i}(s)$ may be constructed and the equations 4.29 solved. (The determination of $B_{2i}(s)$ from the measured potentials is discussed later in this section.) Each value of i gives separately the conductivity profile. The agreement between the profiles deduced indicates the reliability of the data. Generally the most accurate solution will be obtained for the lowest value of i.

It would be desirable to use the additional information available in the evaluation of the data, rather than as a check. This is most usefully accomplished by the elimination of terms like R'_{2i} in P_{2i}. R'_{2i} involves the second differential with respect to surface position, s, of the coefficient B_{2i} and is known inaccurately if measurements are made on only a few successive surfaces of the specimen. Relations between the functions P_{2i} and Q_{2i} are found by taking linear combinations of the equations 4.29:-

$$u = \frac{Q_{2k} - Q_{21}}{P_{2k} - P_{21}} = \frac{Q_{2m} - Q_{2n}}{P_{2m} - P_{2n}} = \text{etc.} \qquad (4.31)$$

and

$$u' = \frac{P_{2k}Q_{21} - Q_{2k}P_{2n}}{P_{21} - P_{2k}} = \frac{P_{2m}Q_{2n} - Q_{2m}P_{2n}}{P_{2n} - P_{2m}} = \text{etc.}$$

for all values of k, l, m and n. From equations of the type 4.31, expressed in terms of the functions R_{2i} and B_{2i}, some of the R'_{2i} functions can be eliminated depending on the number of the B_{2i} which are known. All of the R'_{2i} may be eliminated if at least five of the B_{2i} functions are known. The algebra of the elimination is, however, complicated.

The remainder of this section describes the derivation of the quantities $B_{2i}(s)$ from the potential measurements on the plane z=s.

It has been shown (149) that the asymptotic form of the potential variation at large radii is

$$V(r) = \frac{I}{2\pi\sigma(s)} \cdot \frac{1}{r} \left[k(\theta) + \sum_{m=1}^{\infty} (-1)^m \cdot \frac{(1.3.5\ldots(2m-1))^2}{(2m)!} \cdot \frac{d^{2m}k}{d\theta^{2m}} \cdot \frac{1}{r^{2m}} \right]_{\theta=0}$$

$$= \frac{I}{2\pi\sigma(\infty)} \cdot \frac{1}{r} \left[1 - \frac{1^2}{2!} \cdot \frac{E_2}{r^2} + \frac{1^2.3^2}{4!} \cdot \frac{E_4}{r^4} - \frac{1^2.3^2.5^2}{6!} \cdot \frac{E_6}{r^6} + \ldots \right] \qquad (4.32)$$

where $E_n = \left[\frac{d^n}{d\theta^n} k(\theta) \, / k(\theta) \right]_{\theta=0} = n! . B_n(s)$ from 4.28. Thus the first few values of $B_{2n}(s)$ may be found by analysing the observed potential variation at large radii in terms of equation 4.32. At the same time the value of $\sigma(\infty)$ is determined. This fixes the scale of the conductivity profile (equation 4.11).

The physical significance of equation 4.32 may be seen by considering the surface potential to be due to a vertical line distribution, q(z), of current sources in a homogeneous medium rather than to a single point source in an inhomogeneous medium. The elements of the line source are 'image' sources, familiar from electrostatics. They result from the application of the boundary conditions in the real medium. Since $\left[\frac{\partial V}{\partial z}\right]_{z=0} = 0$, q(z) must be an even function. It therefore possesses non-zero multipole moments, S_n $\left[= \int_{-\infty}^{\infty} z^n . q(z) . dz \right]$, only for even values of n. A moment S_n produces a potential S_n / r^{n+1} at large distances, r (150). Hence, in the present case, only odd powers of the distance appear in expression 4.32.

The expression S_n / r^{n+1} for the potential due to S_n is exact if q(z)=0 for $|z|>r$. Since the distribution of image sources here has an infinite extent, but with decreasing magnitude, the equation 4.32 represents the potential distribution when the effects of the image sources at depths greater than r are neglected. The approximation improves

for large radii and the expression 4.32 is an asymptotic expansion.

Thus, it has been shown that, using equations 4.29 and 4.32, the conductivity profile of an isotropic specimen of the stated form can be determined.

iii Anisotropic Case

The case of current flow in anisotropic inhomogeneous media is naturally more complicated than the corresponding isotropic case; the independent components of the conductivity tensor vary with depth generally in different ways. The problem is to determine the variation of all of the independent components. We consider chiefly the case of isotropy in the horizontal plane, with conductivity $\sigma_r(z)$. The conductivity in the perpendicular direction is $\sigma_z(z)$.

Much the simplest approach to the potential distribution in such configurations is to make use of a transformation due to Maillet (151, also see 136, 147) which reduces the anisotropic problem to an equivalent isotropic one. This involves the transformation of the original configuration defined by $(r, z, \sigma_r(z), \sigma_z(z))$ into one defined by $(r', z', \sigma(z'))$ where r' and z' are the new coordinates and $\sigma(z')$ is the new (isotropic) conductivity. r' and z' and σ are generally functions of all of r, z, $\sigma_r(z)$ and $\sigma_z(z)$. The potential is the same at corresponding points.

The case relevant to the present situation is

$$r' = r$$

$$dz' = dz.g(z) \tag{4.33}$$

$$g(z) = (\sigma_r/\sigma_z)^{1/2}$$

$$z' = \int_0^z g(z).dz$$

$$\sigma = (\sigma_r.\sigma_z)^{1/2} \tag{4.34}$$

Radial distances are unchanged. Anisotropy effectively changes the depth of any point (eq. 4.33). Relations 4.33 and 4.34 may be verified respectively from the equivalent to equation 4.4 in the anisotropic case and from the expression for the source strength of the input current.

By analogy with 4.11 a 'normalised' conductivity in the transformed medium is

$$c(z') = \frac{\sigma(z')}{\sigma(\infty)} = \left[\frac{\sigma_r(z).\sigma_z(z)}{\sigma_r(\infty).\sigma_z(\infty)}\right]^{1/2} \tag{4.35}$$

In terms of the quantities c and z' the equations of section 4.3.ii remain valid but they apply to the transformed medium. The reverse transformation yields the corresponding equations in the original medium. In particular equation 4.24 becomes

$$B_i(z) = \int_{\infty}^{z} c(z).g(z).D_i(z).dz \quad , i>0 \tag{4.36}$$

with c(z) and g(z) defined as above and $D_i(z)$ as in 4.23. Evaluating these expressions at the specimen surface, z=s, and differentiating with respect to s gives equations analogous to 4.29

$$\frac{dW}{ds} + P_{2i}W = Q_{2i} \tag{4.37}$$

where $$W = (c(s).g(s))^{-2} \tag{4.38}$$

$$P_2 = \frac{2}{R_2}(R_2' + 2g(s)^2) \tag{4.39}$$

and the remaining P_{2i}, Q_{21} and R_{2i} are defined as in 4.30.

It is necessary to know the coefficient functions in equation 4.37 for two values of i (one of which must be unity) in order to find both c(s) and g(s). The coefficients do not contain g(s) explicitly for i greater than one. Thus equation 4.37 may be solved with (say) i=2

and the function W(s) so found can be substituted into the equation for i=1 to determine g(s). Then c(s) and the two conductivity components σ_r and σ_z can be found at once.

The evaluation of the functions $B_{2i}(s)$ from the observed potential distribution is exactly the same as described in the previous section. The $B_{2i}(s)$, being coefficients in the series expansion of the kernel function, are determined solely by the surface potential distribution (equation 4.10).

The corresponding problem when there is anisotropy in the horizontal plane is much more difficult. A transformation as described above is not applicable if this anisotropy varies with depth. It would involve an elongation, dependent on depth, of one of the horizontal coordinate axes. In the case of a structure consisting of discrete layers the adjacency of points across a boundary is lost in the transformation. Thus the boundary conditions of the problem are invalidated, i.e. charge is not conserved in the transformed medium. To solve the problem recourse must be made to the equation div $\underline{j}$ = 0 in the original medium. The first part of the solution, reaching a stage corresponding to equation 4.8, is given in Appendix II.

4.4 Electrical Conductivity Measurement - Apparatus

i The Four-Point Probe - Arrangement of Contacts

The basic four point probe experiment was described in section 4.2. The conductivity is found from a transfer characteristic and a geometrical factor. The theory just developed demands the determination of the distribution of potential due to a single source of current. This information can be derived using the standard configuration of four collinear contacts but it is simpler to conform as closely as possible to the theoretical ideal. This ideal is equivalent to any arrangement in which the effects of one current source and one potential measuring contact are eliminated. The finite sample size precludes the removal to very large distances of the secondary current and potential contacts but their effects may be reduced by using the symmetry of the specimen which is in the present case a rectangular parallelepiped.

Figure 14 shows the positions of the image sources for the two symmetrically situated actual sources A and B on the specimen (represented by the central rectangle). Associated with each source and image shown is an infinite row of images perpendicular to the plane of the page. These images result from the boundary conditions at the top and bottom surfaces of the sample. By symmetry, the electric field near the source A is due to the source A alone, with a small

additional field in the y-direction due to source B and its images. If, instead of a point source, B is a uniform line source along one side of a thin sample then it produces no electric field at A. The optimum positions and forms for the two current electrodes are thus determined as being A and B.

We now require to find the most suitable position for the auxiliary potential probe. There is no point on the specimen which necessarily corresponds to the chosen zero of potential (that at infinity in a semi-infinite medium). However, an electrode fixed at any point on the sample is at a constant potential (per unit current) which can easily be eliminated from the measurements. To ensure conditions as similar as possible between experiments the probe may be placed at a point of symmetry, such as C or D, where the electric field is zero. Then small variations in the position of the contact do not affect the measured potential.

With the electrode configuration described above, the required potential distribution may be measured in the vicinity of the source A. The main disturbing effects are a that discussed in the previous paragraph and b the potential gradients due to the image sources nearest to A. These image sources are those directly above and below A with the specimen dimensions used (about 8 mm. x 10 mm.

x 2 mm.). The effect of these images was calculated and was always less than the errors of measurement. The specimens were thus effectively semi-infinite so far as the present measurements were concerned.

The measurements of potential are most conveniently made on a line passing close to A. If the auxiliary current source B is a point source, a straight line in the x-direction is most suitable, that is, a line perpendicular to the electric field of B.

Henceforth, the 'main' current probe, at A, is referred to as c_1; the 'main' potential probe near A is p_1; the current probe at B is c_2 and the potential probe at C or D is p_2.

It is clear that the perturbation of the potential distribution caused by an inhomogeneous surface layer extends to distances only of the order of the depth of the inhomogeneity. This was estimated to be about 20 microns in the specimens used. Thus measurements had to be performed with probe spacings between c_1 and p_1 which were of this order. Furthermore, for the theory given to be applicable and for accurate measurement of the distances, the dimensions of the areas of contact to the specimen of c_1 and p_1 must be much less than the interprobe spacing. It was also required that the p_1-probe could contact the specimen at any position on the chosen line past c_1.

ii The Four Point Probe - Construction

The requirements of the last paragraph were put into practice as follows. Finely pointed probe wires were mounted on movable stages. One such assembly is shown in figure 15 which depicts the experimental arrangement. The probe itself was clamped into a hole in a brass block which was attached, through an insulating block, to a supporting arm. This arm could be tilted, using a screw, so that the probe was moved vertically. By means of a long arm attached to the screw very fine adjustments in the vertical position of the probe were possible. The probe could be set down anywhere on the specimen surface.

The probes were made from 0.2 mm. diameter tungsten wire electrolytically etched to a point using 5% caustic soda solution and alternating current at six volts. To obtain a point with uniform taper and an included angle of 3 or 4 degrees, the wire was raised during etching. The probe was finally cleaned by passing direct current at four volts for about one second. The radius of the probe tip was .5 micron or less. Finer probes were easily made but were too weak for use in this apparatus. The c_1 probe was made rather coarser than the p_1 probe since it had to pass much larger currents and its contact with the specimen was required to be stable for periods of about one hour, indicating that a larger contact pressure was needed. For

the auxiliary probes, c_2 and p_2, no special shaping was performed. These probes were applied with quite large contact forces, to ensure stability. The probe wires were bent to obtain horizontal and vertical sections each about 5 mm. long. When the probes were mounted the horizontal parts acted as a spring loading with a force constant of about 0.05 gm. wt. / micron deflection of the probe.

iii The Four Point Probe - Use

The probes were lowered gently to contact the horizontal surface of the specimen. The c_1 probe made contact with a force of about 0.5 gm. The p_1 probe was adjusted so that it could move along a line passing c_1 at a distance of about twenty microns, without touching. For this to be possible both p_1 and c_1 were tilted slightly from the vertical.

The measurements of potential were made with p_1 lowered to contact the specimen every few microns along a traverse past c_1. The indicated potential rose by one or two per cent. as the contact pressure was increased for reasons discussed later. The measurement was taken when further pressure increase had no effect on the potential. The p_1 contact force was about 0.1 gm.

To shield the specimen from draughts and to prevent arcing should either current contact break down, a drop of

an inert liquid, silicone oil, was placed on the sample surface. Also, while measurements were made, the apparatus was in a draughtproof box.

The smallest interprobe spacing ever achieved with the apparatus was nine microns. It was not worthwhile to use such a small distance generally; the relative error of measurement was too large.

The areas over which electrical contact was made by c_1 and p_1 were estimated in a few cases from the spreading resistance of the contacts. Measurements were made of the resistance between, for instance, the c_1 and c_2 probes in contact with the specimen and then, with the same contact forces, touching a cleaned copper block. The difference in resistances was the spreading resistance of the c_1 contact. The spreading resistance of c_2 was neglected; the contact area of c_2 was much larger than that of c_1. Values of about one ohm were generally obtained. In a homogeneous medium of conductivity σ the spreading resistance is

$$R = (Fa\sigma)^{-1}$$

where F is a geometrical factor equal to 2π for a hemispherical contact and to 4 for a circular disc (152). 'a' is the corresponding radius. Hence in the present case the radii of the contact areas were of order 0.5 micron.

Following these measurements the interprobe distances which had been used were found by photographing the damage produced on the specimen by the probes. Figure 16 shows a typical example. A Reichert projection microscope was used. The damage caused by p_1 was usually quite regular and its position was found to within 0.25 micron. The c_1 damage was more extensive but in general the position of the centre of the contact could be guessed from the photograph; this guess was then verified from the symmetry of the measured potentials about the point closest to c_1 on the traverse line of p_1. Any asymmetry remaining in the apparent potential distribution was allowed for in the analysis of the measurements.

When the set of measurements described above was completed a thin layer was stripped from the sample using Sellotape and the measurements were repeated on the freshly exposed surface.

The Sellotape was stuck on to a clean glass slide and was then removed. (Immersion in water loosened the base of the tape and the adhesive was dissolved by benzene.) The thin layer of antimony telluride remained stuck to the slide, probably because of the presence of minute amounts of adhesive. The thickness of the layer was measured using a sensitive mechanical gauge (Talysurf). It was generally of the order of four microns.

iv The Four Point Probe - Thermal Effects

It is well known that electrical measurements made on materials with high thermoelectric figures of merit are susceptible to errors because of stray thermal e.m.f.s. These e.m.f.s can arise from stray temperature gradients in the apparatus and from thermal gradients produced by the current flow in the specimen. The thermal effects are usually eliminated from the measurement by using some form of alternating current and measuring circuit. In the present experiment, the input current to the sample had an alternating square waveform. This gave a zero mean generation of Peltier heat at the current contacts and thus no thermal gradients due to this effect except near the electrodes. The current produced an alternating potential difference between the p_1 and p_2 probes. To obtain a direct potential for measurement on a potentiometer the connections to these probes were reversed in synchronism with the current. This reversal eliminated from the measurements any steady thermal e.m.f.s in the system and also those due to Joule heating in the spreading resistance of the current contacts.

The only thermally produced component of the measured potential was that caused by the thermal wave due to the oscillating Peltier effect at the c_1 contact. The expressions for the amplitude and phase of the thermal wave

for this particular case were not found in any of the standard textbooks. The derivation of these quantities is given in Appendix III. Also, expressions are given for the measured effect, taking into account the reversal of the potential measuring leads, and another form for the electrically generated temperature at any time and position. The amplitude of the thermal wave has approximately the form $\exp(-cr)/r$ where c is a positive constant. The thermal e.m.f. is therefore negligible at large values of r. The application of these results to the analysis of the present work involves the assumption that there is no inhomogeneity in the thermal diffusivity of the specimens. This is thought to be justified to a sufficient accuracy. With this assumption it is in principle possible to determine both the diffusivity and the ratio of Peltier coefficient to thermal conductivity of the sample.

The Peltier generation of heat can be influenced by Joule heating near the contact. That is, the Peltier coefficient is altered by the rise in temperature due to the Joule effect. The expression for the temperature rise at a small contact of any shape passing a current has been given by Cutler (153)

$$\delta T = \Pi IR(\sigma/k) + \tfrac{1}{2}(IR)^2(\sigma/k)$$

where the spreading resistance is R, the current is I, the Peltier coefficient is Π and σ and k are the electrical and thermal conductivities respectively. The first term represents Peltier heating, the second Joule heating. For the present experiments, the above expression gave a temperature rise at the contact of about $\pm$ 35°C (depending on the direction of the current) due to Peltier heating and about 1½°C due to Joule heating. The rise due to Joule heating in the probe wire was calculated to be 10°C or less. Thus the mean contact temperature, determining the mean Peltier coefficient, was almost equal to the ambient temperature.

4.5 The Electrical Circuit and Its Use

i The circuit used for the measurements was very straightforward. The power supply was an eight volt battery of accumulators. This was connected in series with a current limiting resistor of 400 ohms, a standard resistor of 0.1 ohm, a milliammeter and the input to one section of the automatic reversing switch, the 'chopper'. (This section of the chopper is called the 'current section'.) From the direct current, the chopper produced current with an alternating square waveform which was passed directly through the c_1 and c_2 contacts of the four point probe.

The potential difference appearing between the p_1 and p_2 probes was applied to the second section of the chopper (called the 'potential section') and was converted to a direct signal with the same waveform as the input current. This signal was passed to a Tinsley potentiometer (type 4363) graduated in microvolts. The potentiometer output was applied in turn to a thermal compensator, a photocell galvanometer amplifier and a galvanometer (Tinsley types 5214 A, 5214 and SS2/45E respectively). The compensator was used to offset stray thermal e.m.f.s in the potentiometer circuit. Screened wire was used for leads carrying small signals.

The sensitivity of the measuring system was adjusted, using the amplifier feedback control, so that full scale deflection of the galvanometer was obtained from about one microvolt to the potentiometer. A steady potential could then be measured to within 0.1 microvolt with ease. In the experiment the indicated potential was the mean of the periodically varying input potential. The mean current drawn from the power supply was measured by connecting the potentiometer across the standard resistor in the input circuit.

The response of the measuring system was tested. It was found to be linear in the voltage range employed with the waveforms used. The measurements of current and

potential difference were in accord with the value of a standard resistor when this was substituted for the four point probe. The non-equilibrium arrangement thus gave no additional errors.

A switch was provided to short circuit the input of the potential section of the chopper. At intervals in a series of measurements this short circuit was applied and the electrical zero of the galvanometer circuit was readjusted using the thermal compensator. After the initial setting, this adjustment was always very small, of order 0.1 microvolt.

The potentials measured on the specimen generally fluctuated rapidly and irregularly with an amplitude of about 0.3 microvolts, often much more and occasionally much less. The fluctuation was least when measurements were made on a freshly prepared crystal surface. The effect was therefore attributed to the presence of traces of dirt on the specimen surface or, sometimes, the probe tip. The amplitude of the variation for a particular measurement was taken to be the error of the measurement.

ii Design of the Chopper

The chopper was essentially a set of eight periodically operated contact pairs wired to perform the function of a two pole reversing switch. The mechanism (figure 17) followed closely the design of Dauphinee (154).

Beryllium-copper strips (A), clamped at their upper ends, carried gold-nickel alloy electrical contacts (B). A reciprocating light bakelite rod (C) operated contact pairs in antiphase. The phase of the cycle at which a contact pair closed or opened was controlled by an insulated screw (D) which adjusted the stationary contact. The rod C was driven, through a cam and pulley system, by a synchronous motor. By means of the pulley system the chopper could be operated at various speeds between 16 and 42 c.p.s. A speed of 32.5 c.p.s. was generally used. The galvanometer could then respond neither to the signal frequency nor to its beats with possible stray 50 c.p.s. signals.

iii Adjustment of the Chopper

Suitable adjustment of the chopper was essential to obtain reliable measurements. The waveforms of the input current and output potential are shown in figure 18. The various requirements for the adjustment are listed below, those for the current section of the chopper being given first.

a The current section of the chopper was adjusted to a break before make condition. For two parts (A, figure 18) of each cycle there was no current flow. The potential difference (fig. 18, i) measured across the standard resistance in the input circuit then corresponded to the current actually passing through the specimen (fig. 18, ii).

b The two parts B of each cycle were adjusted to be equal within 0.1%. This was done by arranging the mean output current (fig. 18, ii) to be zero. The net generation of Peltier heat was then minimised.

c The two parts A of each cycle were made as nearly equal as possible, using an oscilloscope. This had the minor advantage of minimising the first harmonic component of the current waveform which, in some cases, might 'beat' with stray effects at mains frequency.

Now consider the adjustment of the potential section of the chopper. The potential difference generated between the p_1 and p_2 probes has, like the current, the waveform of fig. 18, ii. The chopper converts this to the waveform of fig. 18, iii. The potential measurement required is the mean value of this wave, shown as a dashed line. To obtain this measurement, the current flowing in the potentiometer input circuit should have just the same waveform. This current depends upon the specimen and probe resistance as seen from the chopper, the potentiometer input resistance and the chopper adjustment. Assuming the specimen resistance to be much less than that of the potentiometer (60 ohms), two possible cases of the current waveform are shown in fig. 18, iv and v, corresponding to different chopper adjustments. In case iv the potentiometer input is short circuited during the part D of each half-cycle. In case v

it is open circuited so that no current flows during time D. The waveform of iv is the better approximation to the waveform of i and was used.

d The potential section of the chopper was adjusted so that it presented a short circuit for a very small part, D, of each half-cycle.

e The phase of D was arranged to be at the mid-point of part A of the cycle. Then the potentiometer was connected to the specimen in opposite directions for equal lengths of time and there was no effect due to steady thermal e.m.f.s in the specimen or probes.

During experiments, the condition that the specimen resistance was small was fulfilled by application of sufficient contact pressure (as described in section 4.4.iii). The spreading resistance of the p_1 contact was then small. The effects of the flow of current in the potentiometer circuit produced only a small (systematic) error, about ½%, in the measurements.

4.6 Other Measurements of Conductivity

Apart from the measurements, described previously, of the potential distribution on the surface of an inhomogeneous layer on a large sample, two other types of conductivity measurement were performed.

For the use of the method of analysis given earlier it was necessary that the conductivity components of the as-grown crystal should be known. They were measured using the four point probe apparatus with the probes closely spaced and collinear. Measurements on a cleavage plane gave the value of $(\sigma_r . \sigma_z)^{\frac{1}{2}}$. The value of σ_r was found from measurements made on surfaces perpendicular to the cleavage plane (prepared as described in Chapter III) with the line of the probes perpendicular to the cleavage (136, 151). For the latter experiment care was taken that the region of the crystal used contained no cracks.

A further set of conductivity measurements was made on the thin layers of material previously stripped from the diffused specimens (section 4.4.iii). The van der Pauw method (138) (discussed in section 4.2) was used. Five small indium contacts, about 0.1 mm. across, were made to the specimen edge. The specimens were very much bent during the stripping process and were often cracked. To ensure that the layers satisfied the conditions of the theory of the method any isolated cracks were extended to join the perimeter of the layer. As a check on the measurements, five sets of readings were taken, using the contacts four at a time. The consistency of the five results indicated their validity. The measurements were made at various temperatures between room temperature and 140°C, in a non-inductively

wound furnace. A thermocouple fastened to the reverse side of the glass specimen mount was used to determine the temperature of the sample.

4.7 Hall Coefficient Measurement

As part of his analysis of the determination of conductivity using irregular disc samples, van der Pauw also showed how the Hall coefficient was to be found (138). The method was used in the present work with the same specimens as in the previous section and the same type of measurements. The resistance $R_{AC,BD}$ (defined as in section 4.2) was measured with a magnetic field perpendicular to the plane of the sample and then with an opposite, but equal, magnetic field. The Hall effect corresponded to the difference between these resistances and could be found only within a 10% error.

The magnetic field used was about 4000 gauss. Otherwise measurements were made under the same conditions as those of the conductivity.

4.8 Determination of Specimen Composition

i X-Ray Fluorescence

Cleavage faces of antimony telluride single crystals were subjected to composition measurement using X-ray fluorescence. The samples included the non-stoichiometric layers used in the previous experiments.

The instrument used was a Raymax 60 manufactured by A.E.I. Ltd. Measurements were made using the $L\alpha_1$ emissions from both antimony and tellurium. They were not affected by the plastic or glass specimen mount.

Standard specimens for calibration purposes were made from compressed mixtures of finely powdered antimony and tellurium.

ii X-Ray Diffraction

The composition of non-stoichiometric antimony telluride may be found from the lattice parameters if the data of Brown and Lewis are assumed to be correct (38) (see page 42).

Debye-Scherrer X-ray exposures were made for various samples of both as-grown and non-stoichiometric material. The specimens were ground in an agate mortar to pass through a number 300 mesh. They were loaded into glass capillaries and were annealed at 150°C for one week. The low temperature was chosen to avoid the possibility of further evaporation of material.

The exposures were made using copper Kα radiation.

iii Polarography

The powder specimens from the X-ray diffraction experiments were analysed by standard polarographic techniques.

4.9 Thermoelectric Power

The thermoelectric power of the as-grown single crystals of antimony telluride was measured by a standard method.

A specimen a few millimetres thick had two surfaces prepared by cleavage. It was held between polished copper blocks which were heated by internal resistance elements. The temperature difference between the blocks was governed by a controller which was operated by insulated thermocouples inserted in small holes near to the heating elements. The difference of temperature was variable between $\pm$ 20°C. The potential difference between the blocks as a function of temperature difference yielded the thermoelectric power of the crystal, relative to copper, at the mean temperature of the measurements. The apparatus was maintained under argon at about 10^{-4} mm. of mercury pressure while measurements were made between room temperature and 210°C.

C H A P T E R V

R E S U L T S

CHAPTER V

RESULTS

This chapter deals with the values obtained for the various phenomenological parameters of the material and with the methods of deriving these parameters from the measured quantities.

In this chapter the conductivities σ_r and σ_z of the previous chapter are signified by σ_{11} and σ_{33} respectively. This is a more suitable notation for the crystals employed.

The errors quoted throughout this chapter are the standard deviations.

5.1 Electrical Measurements on Homogeneous Samples

Measurements were made on the as-grown crystals to determine the electrical conductivity tensor, one of the two Hall coefficients and the thermoelectric power.

i Electrical Conductivity

The experimental methods described in section 4.6 were used. Several samples from various parts of a single crystal ingot were tested and the following results obtained at 20°C.

$$\sigma_{11} = (4.70 \pm 0.11).10^3 \text{ /ohm cm.}$$

$$\sigma_{33} = (1.91 \pm 0.23).10^3 \text{ /ohm cm.}$$

$$(\sigma_{11}/\sigma_{33})^{\frac{1}{2}} = 1.53 \pm 0.09$$

$$\sigma = (\sigma_{11}.\sigma_{33})^{\frac{1}{2}} = (3.18 \pm 0.14).10^3 \text{ /ohm cm.}$$

The errors quoted are due to actual differences in the specimens; the various parameters were constant within these errors along the length of the ingot. Measurements on a single specimen were reproducible within 1%.

The temperature variation of the radial resistivity, ρ_{11}, measured by the van der Pauw method, is shown in figure 19 normalised to the value at 20°C. The errors of the measured points on this curve are of order 0.3% or less. Only electrical measurements are involved; the geometrical factor cancels from the calculation. The graph has an upward curvature and the points lie on a straight line if either $\rho_{11}(T)/\rho_{11}$ (20°C) is plotted against (temperature, $T^{\circ}k)^{5/2}$ or log ρ_{11} is plotted against T.

ii Hall Coefficient

The Hall coefficient measured was that with the current flowing in the basal plane and the magnetic field

perpendicular to this plane (ρ_{123} in the usual notation (ref. 7)). At 20°C the best value $\rho_{123} = 0.057 \pm 0.005$ cm.^{3}/coulomb was obtained from measurements on several specimens. The variation with temperature for one specimen is shown in figure 20. The errors shown in this figure correspond to the errors in the electrical measurements. There is also a systematic error (in this case of order 5%) in the graph due to inaccuracies in determining the relevant geometrical factor, the specimen thickness.

The above measurements were made with a magnetic field of 3770 gauss. Additional measurements at 6500 gauss showed no significant differences in the Hall coefficient.

iii Thermoelectric Power

The absolute thermoelectric power in the temperature range 20 to 210°C is shown in figure 21. Each point on the graph was obtained as follows. The straight line of best fit to the readings of potential difference and temperature difference between the copper blocks was found by the method of least squares (150, 155). Its slope represented the thermoelectric power. The error in the slope was also calculated in the analysis and is shown in figure 21. The absolute thermoelectric power of copper, calculated from $\alpha_{Cu} = 2.76 + 0.012T$ μV/°C (T in °C), was added to the measured quantity.

5.2 Electrical Measurements on Diffused Samples

A complete set of data was obtained for only one diffused specimen. For this specimen (2-27A) diffusion took place into a vacuum for 240 hours at 500°C. The analysis of these data is given. Corroborative evidence from other specimens is introduced where relevant.

Although the reverse of the chronological order of measurement, the readings made on the sheet specimens are dealt with first. These results are used in the analysis of the four probe measurements.

i Sheet Conductivity and Hall Coefficient Measurements

The layers removed from the surface of specimen 2-27A had the properties at 20°C shown in table 3. The first column of this table represents the mean depth of the layer below the original surface of the sample. W has the same significance as in section 4.3.ii (equation 4.38); that is $\sigma = (\sigma_{11}\cdot\sigma_{33})^{\frac{1}{2}}$, $g = (\sigma_{11}/\sigma_{33})^{\frac{1}{2}}$, $c(z) = \sigma(z)/\sigma(\infty)$, $W = (gg)^{-2} = (\sigma(\infty)/\sigma_{11}(z))^{2}$. ($\sigma(\infty) = 3.18.10^{3}$ /ohm cm. from section 5.1.i.)

The errors shown for the conductivity and Hall coefficient involve the inaccuracies in the electrical measurements and those of the layer thickness. The latter error was the larger. The Hall mobility may be found in the van der Pauw method without a knowledge of the specimen

Table 3

Properties of layers removed from diffused specimen 2-27A

Mean depth, z microns	σ_{11}/ohm cm.	W	ρ_{123} cc./coul.	μ_H cm^2 /volt.sec.
2.5	$(2.77 \pm .17) .10^3$	$1.32 \pm .18$	$.053 \pm .006$	147 ± 5
5.7	$(2.5 \pm .3) .10^3$	1.6 ± 0.3		
8.4	$(2.9 \pm .8) .10^3$	1.2 ± 0.6		
23.7	$(4.9 \pm .3) .10^3$	$0.42 \pm .05$	$.056 \pm .003$	274 ± 4

dimensions. The mobility thus exhibits a comparatively small error and is more suitable to characterise the sample than is the Hall coefficient.

The temperature dependences of the normalised resistivity ρ_{11} and the Hall coefficient ρ_{123} for some of the specimens are shown in figures 19 and 20 respectively.

The surface layer from a specimen annealed in antimony vapour at 500°C for 3800 hours showed properties as follows:-

$\sigma_{11} = (3.05 \pm 0.10).10^3$ /ohm cm.

$\rho_{123} = 0.0124 \pm 0.0010$ cc./coulomb

$\mu_H = 37.1 \pm 2.5$ cm.^{2}/volt sec.

ii Four Probe Measurements - Method of Analysis

A typical set of readings from the four probe apparatus is shown in table 4 and figure 22. Such measurements were required to be analysed in terms of the various contributions to the measured potential which were discussed in section 4.4. These contributions are summarised here and are presented in a form suitable for the analysis. In the following, Ω and Ψ represent the potential generated per unit current. Ω is the total measured effect and Ψ the purely electrically generated potential due to the point source in a semi-infinite medium.

Table 4

Measurements of Potential Distribution on the Surface of Specimen 2-27A

R microns	Ω μv/mA	ΩR	Weighting function, λ
50.7	9.81	497	.330
40.6	12.24	497	.291
34.3	14.38	493	.262
25.5	18.78	478	.214
20.3	23.06	468	.176
19.1	23.94	457	.167
19.5	24.26	473	.167
23.6	20.40	481	.200
28.3	17.34	490	.229
43.8	11.42	500	.303
62.2	8.01	498	.369
71.6	6.87	492	.399
91.8	5.26	483	.458
112.4	4.10	461	.520
130.9	3.47	455	.565
154.0	2.88	444	.620
168.1	2.59	436	.654
189.9	2.25	427	.702
206.3	2.00	412	.745
231.3	1.76	407	.794
250.7	1.57	394	.840
273.1	1.41	384	.888
294.4	1.29	380	.927
310.6	1.20	372	.962

R is the measured probe separation, Ω the measured potential per unit current and λ the weighting function 5.5 with $\beta_1 = .05$, $\beta_2 = .3$ and $\beta_3 = .3$

a. The main contribution to Ω is Ψ, which may be written in the form

$$\psi(r) = \frac{A_1}{r} + \Psi_1(r) \qquad (5.1)$$

$A_1 = 1/2\pi\sigma$ and represents the effects of the homogeneous base material. $\Psi_1(r)$ represents the perturbation due to the inhomogeneous surface layer. Equation 4.32 shows that, for large radii, the series expansion of $\Psi_1(r)$ in terms of r^{-1} contains only odd powers, starting with the third. The sum of the first few terms of this series is not a suitable representation of Ψ_1 for the purposes of analysis, however; the inaccuracy would be large for the smaller values of r. It is better to choose for the form of Ψ_1 a sum of functions each of which possesses the above series expansion for large radii. In the present work functions of the type $S_1 r^L/(1 + (r/S_2)^2)^m$ were used $(L - 2m + 3 = 0)$. S_1 and S_2 are the parameters to be found and are different in each term.

b. The constant potential per unit current developed at the auxiliary potential measuring probe, p_2, in the electric field of both current electrodes is represented by the parameter A_2.

c. The Seebeck emf. generated by the thermal wave due to the Peltier effect at contact c_1 may be represented

approximately in the inhomogeneous medium by the expression A3.14 of Appendix III which is derived for a homogeneous medium. The series A3.14 converges rapidly because of the n^{-2} factor (n = 1, 3, 5, ...). Terms above the second may be neglected in the present application. The waveform factor R = $^{1}/_{4A/(A + B)}$ (see figure 18) appears in A3.14. Its value in the present experiment was 0.0780, which rendered the second term of A3.14 very small compared to the first term. Hence the thermal effect considered may be adequately represented by the expression

$$\frac{A_7}{r}.\exp(-A_8 r).\cos(A_8 r) \qquad (5.2)$$

From A3.14, A_7 = 485 α^2/k μvolt micron/mA. at 20°C, where α is the thermoelectric power of the crystal surface in mV/°C and k is the thermal conductivity on watts/cm. °C.
A_8 = 10.11/a for the chopper frequency used (w = 204.2/sec.) where 'a' is the thermal diffusivity of the material.

Clearly this potential difference is independent of the sign of the thermoelectric power. Detailed consideration of the heat flows involved shows that near the electrode it has the same sign as the purely electrically generated potential.

Summing the contributions to the measured potential yields

$$\Omega(r) = \frac{A_1}{r} + A_2 + \Psi_1(r) + \frac{A_7}{r}.\exp(-A_8 r).\cos(A_8 r) \qquad (5.3)$$

It is required that the coefficients in this expression be found, especially A_1, A_7, A_8 and at least the first two coefficients in the series expansion of Ψ_1.

A systematic error which occurred in the measurements could in part be eliminated in the analysis. Figure 23 shows the geometry of the measurement of potential at the point E on the p_1-probe traverse line HJ. The assumed electrical centre of the current source is B. The actual centre is C, displaced from B in general in both the x and y directions. The measured probe spacing is then R but the true spacing is r. The displacement BD may be detected through the asymmetry of the measured potentials about the point G. The other component of the error, DC, affects the apparent potential distribution in a manner inseparable from the effects of inhomogeneity. It is probably the most important experimental error. Its magnitude was of the same order as A_9, in practice about 0.3 micron. Since its effects cannot be established, the analysis assumed the points C and D to be coincident ($r = r_1$). Then the potential distribution to be represented by equation 5.3 was $\Omega(r_1)$, related to the measured distribution $\Omega(R)$ by the equation

$$r_1 = (R^2 + A_9^2 + 2A_9R(1 - h^2/R^2)^{\frac{1}{2}})^{\frac{1}{2}} \qquad (5.4)$$

(see figure 23). A_9 was such that the variation of potential on the line HJ was symmetrical about the point F.

The calculation of the unknown parameters in 5.3 and 5.4 was performed by the method of least squares (150, 155) using an I.B.M. 1401/7090 digital computer system. Provision was made in the program to use any required combination of the terms in 5.3 (for instance, Ψ_1 is known to be zero in homogeneous samples) and to fix any of the parameters at any desired value for a particular calculation. The latter facility was useful in reducing the number of parameters to be determined since, from section 5.1.i, the value of A_1 is known independently and may be fixed.

As discussed in reference 155, a suitable weighting function must be employed in the least squares calculation. The weighting function, λ, expresses the different reliability of individual measurements and equals the reciprocal of the errors of these measurements. The error in the potential was in the present case due to three separate effects,

a. The error in the zero setting of the galvanometer. (β_1, equal to about 0.01 microvolt/mA with the 20 mA current used)

b. The error due to the unsteadiness in the measured potential (see section 4.5.i). This was roughly proportional to the square root of the potential. ($\beta_2\Omega^{\frac{1}{2}}$ with β_2 approximately equal to 0.3)

c. The effective error in Ω due to the error in measuring the distance, R. In the least squares analysis R was assumed to be known precisely and a corresponding error was introduced into Ω. This uncertainty had magnitude $\delta\Omega \simeq \frac{d\Omega}{dR}.\delta R \simeq -\frac{\Omega}{R}.\beta_3$. $\beta_3 = \delta R$, the random error in R, which was estimated to be 0.3 micron.

Combining the above errors by the usual root of the sum of the squares method yields the weighting function

$$\lambda = (\beta_1^2 + \beta_2^2\Omega + (\beta_3\Omega/R)^2)^{-\frac{1}{2}} \qquad (5.5)$$

The system of simultaneous equations set up as part of a least squares calculation, the 'normal' equations, was non-linear in the present case and was solved by an iterative process.

iii Four Probe Measurements - Analysis of Experimental Curves

The distribution of potential was measured on four consecutively exposed surfaces of specimen 2-27A. The set of results shown in table 4 and figure 22 corresponds to the initial specimen surface. One of the photographs from which

the measurements of probe spacings were derived is shown in figure 16.

The various points discussed in the previous section were taken into account. The measurements on the last exposed surface, when no effects of inhomogeneity were detected, showed that for this specimen $A_1 = 500 \pm 4$ μvolt micron/mA. (Hence $\sigma(\infty) = (3.18 \pm 0.03).10^3$ /ohm cm. in agreement with the results of section 5.1.i.) Therefore two calculations were performed, with A_1 fixed at 500 and 496 respectively. The error introduced into the other derived quantities by the inaccuracy of A_1 was thus estimated. It was generally of order 2%.

The weighting function λ of expression 5.5 was used with $\beta_1 = 0.01$, $\beta_2 = 0.3$ and $\beta_3 = 0.3$ and gave generally fairly rapid convergence of the iterative process of solution. About 4 to 10 cycles were needed to calculate the coefficients to an accuracy of one part in 10^4. The effect of altering the weighting function was determined. For example, a change in β_2 (the most important factor in λ) from 0.2 to 0.45 resulted in coefficients only about 4% different.

It was found that the data were sufficiently accurate to allow the determination of only two independent parameters in the representation of Ψ_1, that is, only the first two coefficients in the expansion of Ψ_1 could be

found. The functions used to approximate Ψ_1 were $A_4/r(1 + (r/A_5)^2)$ or $A_4/(1 + (r/A_5)^2)^{3/2}$. The alternative forms were adopted to test the effect on the resulting coefficients of a change in this function. The two trial functions yielded results only about 10% different but the former gave more rapid convergence and a lower standard deviation of the experimental points about the computed best line. The first function above was thus a better approximation to $\Psi_1(r)$ in the range of r investigated. Attempts to represent Ψ_1 by functions not possessing the expansion of the form 4.32 (e.g. exponentials) were generally unsuccessful. Thus the approximation represented by the asymptotic series 4.32 is satisfactory in this work.

The values of the parameters relating to the physical properties of specimen 2-27A were determined as shown in table 5. The quantities B_2 and B_4 are those required in the analysis method of sections 4.3.ii and 4.3.iii. They are derived using equation 4.32. A_7 and A_8 are the combinations of the material's parameters defined in section 5.2.ii.

The quantity $A_1/(r\Psi)_{min}$ in table 5 represents a further item of information obtainable from the measurements. Its interpretation is as follows. If all the calculated contributions except that of the base material and its inhomogeneity are subtracted from the measured potential distribution, the graph of Ψ against r results. $r.\Psi$ reaches

Table 5

Parameters Derived from the Measured Potential Distribution on Consecutively Exposed Surfaces of Specimen 2-27A

depth of surface, s microns	0	4.7	7.1	36.5
B_2 micron^2	107 ± 5	72 ± 5	51 ± 5	0 ± 5
B_4 micron^4	3600 ± 500	290 ± 40	70 ± 10	0 ± 10
A_7 μvolt micron/mA	62 ± 4	11 ± 1	33 ± 2	
A_8 micron^{-1}	.0082 ± .0004	.011 ± .001	.026 ± .002	
$A_1/(r\Psi)_{min}$	1.14	1.20	1.16	

its smallest observed value, $(r\psi)_{min}$, at the smallest measured value of r. The reciprocal value, $1/(r\psi)_{min}$, represents some sort of averaged conductivity for the inhomogeneous system. The maximum conductivity in the system must have at least this magnitude, $\sigma_{max} \geq 1/(r\psi)_{min} 2\pi$. Thus the tabulated quantity, $A_1/(r\psi)_{min}$ sets a lower limit to the maximum value of the normalised conductivity, c(z), attained in the diffused system.

The reproducibility of the potential distribution measurements was checked by determining the distribution a second time on the initial surface of specimen 2-27A. In this case, however, measurements were not made on both sides of the current electrode, so the parameter A_9 could not be found. The other derived parameters were correspondingly in error. In spite of this the values found for B_2 and B_4 were only about 10% different (lower) than those determined from the results of table 4, indicating the validity of the latter. The values found for A_7 and A_8 in this auxiliary test were 40 μvolt micron/mA and 0.010 micron^{-1} respectively.

Measurements made on other diffused specimens, including those annealed under antimony vapour all yielded curves for the potential distribution very similar to figure 22.

iv Interpretation of the Derived Parameters in Terms of the Conductivities

The quantities $B_2(s)$ and $B_4(s)$ of table 5 are to be interpreted in terms of the quantities $c(z)$ and $g(z)$ defined by 4.35 and 4.33 respectively. The analysis is performed using the equations 4.37, 4.38, 4.39 and 4.30 (pages 95 and 89).

It is very convenient to make use of the values of $W(s)$ derived from the measurements of the sheet conductivity (table 3). Thus the analysis proceeds as follows. The functions $R_2(s)$, $R_2'(s)$ and $Q_2(s)$ of equations 4.37 and 4.39 are derived from $B_2(s)$. Then $P_2(s)$ is written down in terms of $g(s)$. The use of the known quantities $W(s)$ and $\frac{dW}{ds}(s)$ in equation 4.37 yields $g(s)$. From $W(s)$ and $g(s)$, $c(s)$ is found. It is checked that the resulting conductivities give the true values of $B_4(s)$.

A plot of the values of B_2 against s shows a linear variation. Thus

$$B_2(s) = 107 \pm 5 - (7.7 \pm 0.3)s \text{ micron}^2$$

$$B_2'' = 0 \pm 0.5$$

$$R_2 = B_2' = -7.7 \pm 0.3 \text{ micron}$$

$$R_2' = 0 \pm 0.5$$

$$Q_2 = 4/R_2 = -0.52 \pm 0.02 \text{ micron}^{-1}$$

$$P_2 = 2(R_2' + 2g(s)^2)/R_2$$

$$= -(0.52 \pm 0.02)g(s)^2 \pm 0.13 \text{ micron}^{-1}$$

The data of table 3 show that in the range $0 \leqslant s < 8$ microns, $W(s) = 1.39 \pm 0.15$ with a probably zero or small negative slope, $\frac{dW}{ds} = -0.015 \pm 0.015$ micron^{-1}. It is unlikely on physical grounds that $\frac{dW}{ds}$ is positive.

The substitution of the above data into equation 4.37 yields the result that $g(s) = 0.84 \pm 0.15$ for $0 \leqslant s < 8$ microns, it being assumed constant within the error in this range. From the values of $g(s)$ and $W(s)$ it follows that the normalised conductivity $c(s) = \sigma(s)/\sigma(\infty)$ equals 1.0 ± 0.2 in the range considered.

Various comments can be made concerning the value of $c(z)$.

a. It is not possible that $c(z)$ equals unity over the complete range of z. Were this so, the medium would be electrically homogeneous and no perturbation of the potential distribution would occur.

b. The upper limit found for $c(z)$, 1.2, is scarcely sufficient to satisfy the condition (represented by $A_1/(r^W)_{min}$) on the maximum of $c(z)$ given in the previous section.

c. The values of B_4 cannot be explained unless $c(z)$ is greater than about 1.25 over some range of z.

For these reasons it appears that the conductivity $c(z)$ reaches a maximum at some value of z greater than 7 or 8 microns. From consideration of the magnitudes of B_2

and B_4 it is likely that the maximum value is about 1.35. This indicates that along a line from the homogeneous body of the specimen to its surface, the conductivity σ_{33} initially increases more rapidly than σ_{11} decreases.

5.3 X-Ray Diffraction and Measurement of Crystal Composition

None of the methods used gave satisfactory results for the composition of the diffused layer. Both X-ray fluorescence and polarography indicated a slight excess of antimony above the stoichiometric amount, however.

The lattice parameters of the congruently melting material were

$$a_{Hex} = 4.263 \text{ Å U.} \qquad c_{Hex} = 30.43 \text{ Å U.}$$

in agreement with the published results (page 20). No change of lattice parameters was detected for the diffused material on the cleavage faces of the crystals. Assuming that a change of c_{Hex} of 0.01 Å U could be identified and that the lattice parameter data of Brown and Lewis (38) are correct, the change of composition of these surfaces was less than 0.3 atomic percent.

About 40% of the Debye-Scherrer photographs made for specimens from diffused surfaces perpendicular to the

cleavage plane showed changes of c_{Hex} of about -0.3 Å U. This corresponds to a composition change of about 8 atomic percent. The remaining 60% of tests showed no lattice parameter change.

C H A P T E R V I

D I S C U S S I O N

CHAPTER VI

DISCUSSION

The results presented in the previous chapter are discussed in terms of the properties of the material, in particular the electronic band structure. The results of other workers are introduced as required. It is found that the knowledge of the anisotropy of electrical conductivity provides important information regarding the band structure. Finally the limitations and advantages of the method used to determine the conductivity profile are discussed.

6.1 Specimen Composition and the Equilibrium Phase Diagram

It is a disadvantage of previous work on antimony telluride that in no case was the crystal composition known with the precision required for semiconductor work. This flaw may be attributed to the non-stoichiometric congruently melting composition, the lack of detailed knowledge of the phase diagram and the different preparation methods employed. Some authors, who have grown crystals directly from a melt, have used the composition of the melt to characterise their specimens (45, 47, 50). Most workers produced crystals by zone melting an ingot of initially stoichiometric

composition. The ingots were zone melted several times, to remove bubbles, etc., before crystal growth was attempted (e.g. 42). The resulting crystals had unknown inhomogeneity in composition.

In the present work the zone melting process was used for single crystal production but the starting composition was that given by Offergeld as being congruently melting, i.e. 40.4 at. % antimony (84). The resulting crystals had uniform electrical resistivity over their complete length, and in particular over the last part to solidify, verifying Offergeld's data. The crystals grown were thus of composition 40.4 at. % antimony, 59.6 at. % tellurium.

There remains the problem of estimating the composition of the diffused crystals used for the electrical measurements. It was shown on page 135 that the composition change on diffusion was less than 0.3 at. %. The direction of the change is not obvious, however. The following points are relevant;

a. There is slight evidence from polarography and X-ray fluorescence that the specimens became richer in antimony.

b. Tellurium is generally more volatile than antimony. For instance, the vapour pressure of elemental tellurium at 500°C is about 10^{-3} atmosphere whereas that of antimony is much less than 10^{-5} atmosphere. In addition, the loss of

the volatile component is well known in this class of compound (26).

c. From the electrical measurements it was found that the anisotropy of electrical conductivity fell on diffusion. As will be shown, this continues a trend from the more nearly stoichiometric crystals of other workers. Furthermore, the four probe potential measurements were indistinguishable for samples diffused for comparable lengths of time in vacuum or in antimony vapour, indicating that the diffusing element was indeed tellurium.

Thus it appears that the diffused specimens had an excess of antimony compared with the as-grown crystals.

The phase diagram for antimony-tellurium in the region of 60 at. % tellurium is now discussed. The previous work was described in section 2.5. The composition limit of the antimony telluride phase is given by Poretskaya as being 59.2 at. % tellurium (101, figure 9). The result from the present work that the composition change was 0.3 at. % or less is apparent support for this. In addition the apparent composition change to about 8 at. % excess antimony found on some of the diffused surfaces perpendicular to the cleavage also agrees with the results of Abrikosov and his group (93). This latter evidence suggests the chance nucleation of a second phase, with a composition roughly corresponding to a phase limit shown by Abrikosov (figure 7).

The range of stability of the Sb_2Te_3 phase may not be as small as appears at first sight, however. The maximum stoichiometric deviation reached in a sample may be much less than that of the phase limit, for the following reasons,

a. The specimen surface, which is continually evaporating, presumably represents the greatest stoichiometric deviation in the sample. This composition is governed by the rates of evaporation of the constituents compared with the rates of diffusion in the solid near the surface (126). Thus there is no reason why the surface of a rapidly evaporating solid should correspond to the phase limit.

b. It is known that in some situations the diffusion coefficient depends strongly on the concentration of the diffusing element. For instance, a change in concentration from 10^{19} to 10^{20} zinc atoms/cc. in gallium arsenide increases the zinc diffusion coefficient by a factor of 100 (156). This results from the changing proportions of differently ionised zinc atoms as the Fermi energy is altered by the increasing current carrier density. It may be that the properties of the surface layer formed on the specimens in the present work were such that diffusion to the crystal surface was greatly reduced. Then the diffusion processes would be governed chiefly by this surface layer. Concentration gradients, once formed, would change only

slowly. This situation, if correct, has relevance for Abrikosov's work since he relied upon diffusion for homogenisation of his samples.

There is, however, some evidence from the electrical measurements that the properties of the surface layer of the diffused specimens are approximately constant over a range of depth near the surface. This implies that the composition is also constant in this range. The situation would then be that of a surface layer possessing a composition probably near that of the limit of the phase, with a 'diffusion front' moving into the material. This presents some further support for the work of Abrikosov.

The work performed is insufficient for the rejection of either of the recently published phase diagrams for antimony-tellurium, those of Abrikosov and of Brown and Lewis. Indeed, the two sets of work can presumably be reconciled in some way, possibly through the existence of a concentration dependent diffusion coefficient as described earlier.

6.2 The Electrical Measurements

The experimental facts to be explained will be summarised. We let X be the stoichiometric deviation; X is positive for material with excess antimony.

a. Jäschke (50) and Liebe (45), with crystals grown from melts having X smaller than in the present work, found the radial conductivity, σ_{11}, to increase with increasing X. The present work shows that at higher values of X σ_{11} falls. The maximum value that σ_{11} can attain appears to be about 5500 /ohm cm. (29, 42).

b. The conductivity perpendicular to the cleavage, σ_{33}, increases with X for all values of X investigated (results of present work and of Jäschke). Eventually σ_{33} becomes greater than σ_{11}, with a probability of 7 : 1 from the errors of the present work. The variation with X of the anisotropy ratio σ_{11}/σ_{33} is very marked. One of Jäschke's samples showed this ratio to have a value of about 300 while the value found in the present experiment for material with high X was about 0.7. The detailed form of the variation of σ_{33} found by Jäschke will be described later. The other published results on the conductivity anisotropy ratio also tend to support the view that this quantity falls with increasing X (29, 42).

c. σ_{11} possesses a temperature dependence which cannot be explained on the basis of simple scattering theory in a simple band. In particular, if acoustic phonon scattering in a single band is assumed, as stated by Brodovii (43), then A1.7, A1.12 (Appendix I) and the properties of the Fermi-Dirac functions, A1.2, for nearly degenerate material

show that the radial resistivity should increase less rapidly at high temperatures. Figure 19 shows this to be untrue for the as-grown material.

d. The Hall coefficient, ρ_{123}, increases with temperature in a similar manner at two compositions. The apparent similarity in magnitude of the two coefficients may be coincidental since there was a large experimental error. The results of Liebe show a similar variation (45). Eichler's measurements on polycrystalline samples show the Hall coefficient reaching a maximum in some cases (47).

The simplest model which may be applied for the electronic band structure of a solid is that of a single, isotropic, parabolic band ($\varepsilon \alpha k^2$) with isotropic scattering. The experimental results cannot be explained on this basis. Neither is anisotropy of the band (probable in antimony telluride) sufficient, for it does not provide a means whereby the various phenomenological anisotropies may change. Various possibilities are now investigated for the explanation of the results.

a. Changes of the effective mass of current carriers with variations of conditions such as temperature and degree of degeneracy are well known in semiconductors (e.g. 19, 20, 157). An alteration with carrier concentration of the effective mass ratios of the ellipsoidal energy valleys in antimony telluride would lead to changes in the ratio of the

mobilities parallel and perpendicular to the cleavage plane (μ_1/μ_3). However, the effective masses have in general been found to change only by a factor of a few times for carrier concentration changes of order 100. From the Hall coefficient measurements, such large changes of concentration did not occur in the materials investigated and the required variation in effective mass ratio seems unlikely. Were such a variation to occur, the band energy could not be even remotely quadratic in the wave vector in this range.

b. Changes of scattering anisotropy must certainly occur in antimony telluride and were suggested by Liebe (45) to explain the high temperature variation of the Hall coefficient. Such variations of scattering might follow from the possible effective mass changes of the previous paragraph but the large magnitude of the changes of mobility are still difficult to explain. Additionally, the scattering properties are unlikely to be very greatly different from those in p-type bismuth telluride where the anisotropy of scattering has been shown to be small (49). It therefore appears unlikely that variations in the scattering anisotropy produce the observed effects.

It is convenient here to make a more detailed comparison with the results found for p-type bismuth telluride by Efimova (49). In this work the various

anomalies, notably the increase of the Hall Coefficient with temperature, were well explained on the basis of the anisotropy of scattering varying with temperature. However, the conductivity anisotropy, σ_{11}/σ_{33}, was assumed constant with respect to changes in the carrier concentration. It did, in fact, show a slight increase with increasing concentration in marked contrast to the results on antimony telluride. It therefore seems unlikely that a similar explanation can be applied to both compounds. The phonon spectra, dielectric constants, etc. should be similar for the two compounds, however, giving the same type of scattering properties as mentioned in the previous paragraph.

c. A further possible explanation for the variation of the conductivity is provided by consideration of the tunnel effect in relation to the potential barrier which must exist between the adjacent $Te^{(1)}$ planes, which are thought to be joined by only van der Waals type bonds. The results of Jäschke (50) for specimens with low stoichiometric deviations, X, show that σ_{33} increases rapidly with increasing X and falls slowly with increasing temperature up to about 50°C when it begins to increase rapidly in a manner apparently governed by an activation process. σ_{11} shows no sign of this latter phenomenon and continues to decrease slowly with rising temperature. The high temperature

variation of σ_{33} must thus be attributed to a rapid increase in the mobility μ_3. The situation would then be such that at low temperatures the value of μ_3 is governed by tunnelling between the $Te^{(1)}$ planes. The tunnelling probability depends very sensitively on the height and width of the barrier. Thus, as X increases and more carriers are introduced into the material, the Fermi energy, ε_F, rises, the probability of transitions between adjacent five-fold layers increases and μ_3 is correspondingly larger. At high temperatures carriers may be thermally activated over the potential barrier. Both transport processes would not affect σ_{11}, at least to a first approximation. However, upon calculation, the barrier heights deduced for the two processes show a wide disparity and the envisaged situation must be incorrect.

A further possibility is that the high temperature increase of σ_{33} is due to electrons excited to the conduction band. This must also be ruled out, however, from comparison of the activation energy (about 0.1 ev) and the forbidden energy gap in the material (page 29).

d. A remaining possibility for explanation of the observations is the use of a two valence band model, each band being considered anisotropic as regards both effective masses and scattering. Such a model possesses a large number of adjustable parameters and is perhaps capable of

being fitted to almost any experimental data. In the present case it accounts for the facts in a reasonable way and is thus considered acceptable. This model (but with spherical symmetry) was employed by Rönnlund to interpret his room temperature data on the thermoelectric power as a function of σ_{11} (59). This interpretation was queried in section 2.4.ii but the work of the present chapter indicates its validity.

We consider a model consisting of a lower band, L, with its extremum at energy $\varepsilon = 0$ and an upper band U with minimum energy $\varepsilon = \varepsilon_U$. The hole energies within the bands are regarded as being greater than those of the extrema. Hence $\varepsilon_U > 0$. The parameters for the two bands are distinguished by subscripts L and U respectively and the two principal directions by single subscripts 1 and 3 respectively. Thus σ_{3L} refers to the electrical conductivity due to the holes in the lower band, in the direction perpendicular to the basal plane. The resulting observable coefficients, due to the contributions from both bands, are given in equations A1.13, A1.15 and A1.17.

Rönnlund, assuming acoustic phonon scattering to be relevant found $\varepsilon_U \approx 1/4$ e.V., the Fermi energy ε_F to be of the same order as ε_U and, for the mobilities, $\mu_{1L} = 57$ cm.^{2}/volt sec and $\mu_{1U} = 340$ cm.^{2}/volt sec. On the basis of these figures the calculated temperature

coefficient of σ_{11} is only about half that determined experimentally in the present work. The dependence on temperature of the thermoelectric power is also incorrect. The differences should be accounted for by modification of the assumptions regarding the scattering process. Such changes would alter the values of the parameters giving the best fit to the data, but probably not by large amounts. A modified model may therefore still be used qualitatively to interpret the data.

The concentration of current carriers presumably increases as the stoichiometric deviation, X, becomes greater. This statement is justified by the large changes of the room temperature Hall coefficient with X. (That the carrier density need not vary with increased doping in some cases was shown by Rosenberg (102).) Thus, as X increases, the Fermi energy rises towards, or further into, the upper band and the proportion of holes in this band becomes greater. The observed consequence of this is that σ_{33} is increased while σ_{11} falls.

The increase of σ_{33} with X is attributed, at least for the larger values of X, to the occupation by holes of states in the upper band when the Fermi energy is sufficiently large. Jäschke's values for σ_{33} at high temperatures may be accounted for if, in his specimens, $\varepsilon_F < \varepsilon_U$. Then the observed activation energy is $\varepsilon_U - \varepsilon_F$ which decreases as X

increases, in agreement with the facts. The available information on the variation of σ_{33} allows no conclusions to be drawn on the relative magnitudes of μ_{3U} and μ_{3L}. The scattering processes are expected to be somewhat different for the two bands. Assuming other factors, such as the deformation potentials, to be equal (which is unlikely to be true, however), the carriers in the upper band undergo less lattice scattering than do those in the lower band because their kinetic energy is less (equation A1.7). For the same reason they are more affected by ionised impurity scattering, although such impurities are probably well screened electrostatically because of the high carrier concentration. It is likely therefore that the relaxation time τ_{3U} is larger than τ_{3L}.

The rapid increase of σ_{33} with X for low X and low temperatures may well be due to the necessarily increasing disorder in the lattice, accompanied by the formation of some bonds between the $Te^{(1)}$ - $Te^{(1)}$ layers. Such bonds would result in a lowering of the effective mass of carriers in the direction across these layers.

The variation of σ_{11} with X allows rather more definite conclusions to be drawn. σ_{11} initially increases with X. σ_{33} increases more rapidly and eventually becomes of the same order as σ_{11}. Then σ_{11} falls with increasing X to a value below that of σ_{33}. There is no apparent reason why

the carrier density should decrease in this region; indeed, the continued rise in σ_{33} indicates that it does not. The fall in σ_{11} must therefore be attributed to a rapid increase in the scattering for holes moving parallel to the cleavage plane. The simplest explanation for this in terms of the proposed model may be made by supposing the fall of σ_{11} to correspond to the rise of the Fermi energy within the upper band, i.e. $\varepsilon_F > \varepsilon_U$. The total scattering for current carriers moving in a given direction depends upon the available density of final states, that is, the density of states with a component of the wave-vector perpendicular to the given direction (ref 4, p. 129). (The scattering is also governed, of course, by the relevant transition probabilities). When $\varepsilon_F > \varepsilon_U$ final states are available in both bands, the scattering is increased and the conductivity falls.

The possibility of such interband scattering has been offered as an explanation for the abnormally great temperature dependence of the mobility in non-degenerate p-type germanium (158). The present situation is very different from that in germanium, but the increased temperature coefficients due to this form of scattering are still expected. Clearly then the determination of the energy band parameters from the phenomenological parameters should be performed using a suitable mixture of the various

types of scattering, including interband scattering.

The properties of the lower band are determined by the behaviour for small stoichiometric deviations. It follows that $\mu_{1L} > \mu_{3L}$. If it is assumed that these mobilities are unchanged by increasing carrier concentrations then the fact that $\sigma_{33} > \sigma_{11}$ when the upper band is occupied shows that $\mu_{1U} < \mu_{3U}$. Since it is unlikely that the scattering in the upper band is very anisotropic it follows that probably, for the effective masses, $m^*_{3U} < m^*_{1U}$. That is, for the upper band the isoenergetic ellipsoids are extended in the direction parallel to the basal plane of the material.

The interpretation of the conductivity data described above is quite consistent with the available information concerning the Hall effect. It is shown by Allgaier (25) that for the model under consideration the Hall coefficient, ρ_{123}, increases with rising temperature so long as $\mu_{1U} \neq \mu_{1L}$. Liebe's results (45) show a variation of this sort as do those of the present work. Liebe's interpretation of his data in terms of changes with temperature of the type of scattering seems improbable. The Hall coefficients vary by a factor of about two but are known from theory to be relatively insensitive to the type of scattering (for a single band with degenerate statistics). Also, it was seen earlier that changes of the scattering could probably not affect the anisotropy of conductivity by the amount observed.

Furthermore, the two band model shows that in many cases the Hall coefficient reaches a maximum at some temperature. Such a maximum was observed in two of Eichler's polycrystalline samples (47).

From the above considerations it is probable that the physical situation in antimony telluride may be fully represented by a two band model. The origin of the second band is not clear. The following possibilities present themselves.

a. The second band is an impurity band; that is, a band caused by wave function overlap between the excess antimony atoms in the lattice. It is very likely that the excess antimony is accommodated in some particular type of plane parallel to the five-fold layers within the lattice (either substitutionally, interstitially or as tellurium vacancies). There are thus always several atomic layers between each layer containing defects. The wave function overlap in the direction perpendicular to the basal plane is therefore always comparatively small. The mobility in this direction, μ_3, is always small, changing only slowly. The amount of overlap in the direction parallel to the cleavage plane increases rapidly with the defect concentration and the mobility μ_1 does likewise. Such properties are not characteristic of either band in the model described so that the presence of an impurity band is unlikely.

b. The observed effects result from the operation of the non-stoichiometric mechanism proposed by Amelinckx (87) (i.e. the presence of large dislocation loops in the basal plane; see page 38). In the region of the loops the crystal structure is considerably altered. In particular there are no pairs of very weakly bonded tellurium planes. Because of this the electronic structure is much changed and probably becomes more isotropic. The specimen may now be regarded as a stoichiometric, very anisotropic crystal with small, more nearly isotropic regions embedded in it. For the degrees of non-stoichiometry attained these regions must be small and it is hard to see how the net conductivity anisotropy ratio σ_{11}/σ_{33} can be reduced below the value unity solely by their presence. The conclusion is therefore reached that the formation of dislocation loops cannot be the main mechanism for the accommodation of non-stoichiometry in antimony telluride.

c. It seems most probable that the two valence band structure arises from the two slightly different bonds in the lattice, i.e. the Sb - $Te^{(1)}$ and Sb - $Te^{(2)}$ bonds. Their lengths differ by only 3% and it is likely that the bond energies are very similar. On this basis, however, it is not clear why the anisotropy is so different for the two bands.

6.3 Discussion of the Conductivity Measuring Method

The method described in chapter IV for the determination of the conductivity profile of inhomogeneous media is here discussed from the viewpoint of its practical application to small samples.

An example of the use of the method was given in chapter V. It was necessary in this example to incorporate experimental data derived independently (from the van der Pauw method), but this was because of the small number of successive crystal surfaces investigated on the specimen by the four probe method. The number was small because the thickness of the surface layers removed, by cleavage using Sellotape, was not controllable. A more suitable method of sectioning is clearly desirable, preferably one which leaves the removed layers intact as in the present work.

The limitations of the method are of several types, those inherent in four probe measurements generally, those particular to the special properties of the apparatus required for this application and those resulting from the method of analysis.

The possible sources of error characteristic of the four probe method as such are well known (137) and were stated on page 76. One of these effects, that of the Peltier heating at the current contacts, was significant in the present work and was taken into account in the analysis.

Consideration of the results of section 5.2.iii shows that the various combinations of parameters of the material cannot be found without a large error. This error is probably due to uncontrollable differences in detailed geometry between different current contacts. Such variations may have a large effect on the proportion of Peltier heat flowing actually into the specimen, and, hence, on the thermoelectric potentials generated. The analysis of the experimental curves would be easier, and more accurate, if the thermoelectric effects were completely eliminated. This may be achieved by the determination of the high frequency limit of the potential distribution either by direct measurement or by extrapolation from lower frequencies.

An important limit on the application of the method is the difficulty of making sufficiently small, yet stable, contacts to the specimen. The minimum probe spacing is required to be not more than the approximate depth of the inhomogeneity. For the simplest theory to be applicable the dimensions of the various contact areas must be much less than the probe spacing. The probes then become mechanically very weak. A major difficulty in the present work was the extreme mechanical weakness of the material under investigation. The damage caused by the probe contact extended apparently well beyond the actual area of contact

and was generally not symmetrical. The determination of the actual contact positions was thus in error. For measurements on harder materials this inaccuracy would be minimised.

The method of analysis of the experimental curves to obtain conductivity profiles has itself certain limitations. An interesting one arises if the geometric mean conductivity, $\sigma = (\sigma_r(z).\sigma_z(z))^{\frac{1}{2}}$, is a constant for a specimen. σ_r may vary in any way with the depth, z. The normalised conductivity, c(z), defined by 4.35, is then always unity. The coefficient B_1 (equation 4.25) in the expansion of the kernel function is always zero. It then follows from equations 4.26 and 4.24 that all the other coefficients except for B_0 also equal zero. The kernel function therefore is a constant and the potential is not changed from its r^{-1} dependence in homogeneous media. The medium can not be distinguished from a homogeneous one from the surface potentials alone. A method of resolving this difficulty is to use samples of finite depth instead of the effectively semi-infinite ones of the present work. The effective electrical thickness of the specimen (from equation 4.33), in its variation with the actual specimen thickness, yields the conductivity anisotropy σ_r/σ_z. Then, since $\sigma_r.\sigma_z$ is known, both $\sigma_r(z)$ and $\sigma_z(z)$ may be found.

A further, more general, defect of the present analysis

method results from the fact that the quantities derived from the potential distribution, the functions $B_{2i}(s)$, $i = 1, 2, 3, \ldots$ (equation 4.32), represent integrals over the conductivity variation. They are therefore insensitive to any fine structure occurring in $\sigma(z)$. This fault is unavoidable since the potential at any point depends on the complete conductivity profile and represents some sort of averaged conductivity for the system.

An advantage of the method is that it can be used to find the anisotropy ratio of conductivity of a very thin surface layer. It is apparently the only method available to do this. In addition it is in principle possible to find the complete variation of conductivity as a function of composition from a single specimen.

The method is very time consuming. The time needed could be much reduced by the use of an analytical method requiring fewer measurements. Such a method is now described for the isotropic case. It uses a knowledge of the surface potential at a single, fixed value of the radius, r, as surface layers are removed. In the limit of small r this gives the conductivity at the surface directly. In the limit of large r such data would yield the coefficient B_2 and hence the conductivity from the analysis given in chapter IV. For intermediate values of r it is probable that the data still contain sufficient information

to determine completely the conductivity profile.

The relations between the conductivity $\sigma(z)$ and the surface potential $V(r)$ are completely defined by equations 4.3, 4.5, 4.8 and 4.9. The function $Z(z, \theta)$ (for $z \geqslant s$) is independent of the position of the specimen surface, $z = s$, since it is defined by equation 4.5 and two boundary conditions at $z \rightarrow \infty$. Then, if the potential $V(r, s)$ is known for a fixed value of r and for all positions of the specimen surface, $z = s$, the conductivity profile may be found as that which is self consistent when introduced into the above set of equations. In more detail, a possible method of approach is to guess a first approximation to $\sigma(z)$. This is probably conveniently taken as the variation with s of the quantity (current/r.V (r, s)). This is substituted in 4.3 and $f(z)$ is found in the approximation. Equation 4.5 is solved numerically for a range of values of θ, and the result is substituted in equations 4.9 and 4.8. From 4.8 the next approximation to $\sigma(s)$ is found directly and the cycle is repeated until $\sigma(s)$ does not change within the required accuracy. The method is clearly complicated from the computation point of view but may be simplified by the use of devices such as that due to Longman (159) for the calculation of the infinite integral over Bessel functions (equation 4.8). The method may be extended to anisotropic media if the potential is known as a

function of s for two values of the radius, r. From the practical point of view such information could be most easily collected using a multipoint probe of fixed probe spacings to make measurements at various points on the bevelled surface of an inhomogeneous specimen.

SUMMARY AND CONCLUSION

A method of growing large single crystals of antimony telluride by the method of zone melting has been described and used.

A method for the evaluation of the variation of electrical conductivity within an inhomogeneous layer on the surface of a uniform material was derived. It has advantages over other methods, particularly when applied to anisotropic materials. The method was applied to diffused layers formed on the cleavage surfaces of antimony telluride crystals. Other electrical properties of the layer were also measured.

The results could not be used to confirm any of the phase diagrams for antimony-tellurium. However, by using the electrical measurements in conjunction with those of other workers, progress has been made in the elucidation of the electronic properties of the material. In particular, the two valence band model proposed by Rönnlund was verified. It was shown that knowledge of the anisotropy of conductivity may perform a valuable function in such investigations.

REFERENCES

1 J. Bardeen and W. H. Brattain, Phys. Rev., 74, 230 (1948)

2 J. C. A. Peltier, Ann. Chim. Phys., 56, 371 (1834)
T. J. Seebeck, Abh. Kgl. Wiss. Akad. Berlin 1822/23, S.265

3 F. D. Rosi, B. Abeles and R. V. Jensen, J. Phys. Chem. Solids, 10, 191 (1959)

4 J. M. Ziman, 'Electrons and Phonons', Oxford, 1960

5 F. J. Blatt, Solid State Physics, 4, 199 (1957)

6 F. Herman, Proc. Intern. Conf. Phys. Semicond., Paris, 1964, p. 3

7 J. R. Drabble, Progress in Semiconductors, 7, 45 (1963)

8 W. Paul and H. Brooks, Progress in Semiconductors, 7, 135 (1963)

9 D. L. Greenaway and G. Harbeke, J. Phys. Chem. Solids, 26, 1585 (1965)

10 H. Ehrenreich and H. R. Philipp, Proc. Intern. Conf. Phys. Semicond., Exeter, 1962, 367

11 C. Sébenne, J. de Physique, 24, 216 (1963)

12 R. Sehr and L. R. Testardi, J. Phys. Chem. Solids, 23, 1219 (1962)

13 P. A. Wolff, Proc. Intern. Conf. Phys. Semicond., Exeter, 1962, 220

E. M. Conwell and B. W. Levinger, Proc. Intern. Conf. Phys. Semicond., Exeter, 1962, 227

R. H. Parmenter, Phys. Rev., 104 (1), 22 (1956)

V. L. Bonch-Bruevich, Soviet Phys.-Solid St., 5 (7), 1353 (1964)

S. F. Edwards and Y. B. Gulyaev, Proc. Phys. Soc., 83, 495 (1964)

14 I. P. Zvyagin, Sov. Phys., Solid St., 7 (4), 779 (1965)

15 N. F. Mott, Phil. Mag., 6, 287 (1961)

16 N. F. Mott, Proc. Intern. Conf. Phys. Semicond., Exeter, 1962, p. 2

17 L. Esaki, Phys. Rev., 109, 603 (1958)

18 V. I. Fistul, E. M. Omelyanovsky, D. G. Andrianov and I. V. Dahovsky, Proc. Intern. Conf. Phys. Semicond., Paris, 1964, 371

19 V. V. Galavanov, O. V. Emel'yanenko and F. P. Kesamanly, Sov. Phys., Solid St., 5 (2), 448 (1963)

20 R. S. Allgaier and B. B. Houston, Jr., Proc. Intern. Conf. Phys. Semicond., Exeter, 1962, 172

21 J. A. Kafalas, R. F. Brebrick and A. J. Strauss, Appl. Phys. Letters, 4, 93 (1964)

22 L. Sosnowski, Proc. Intern. Conf. Phys. Semicond., Paris, 1964, 341

W. Zawadzki, R. Kowalczyk and J. Kolodziejczak, Phys. Stat. Sol., 10, 513 (1965)

23 J. McDougall and E. C. Stoner, Phil. Trans. Roy. Soc., A237, 67 (1938)

P. Rhodes, Proc. Roy. Soc., A204, 396 (1950)

A. C. Beer, M. N. Chase and P. F. Choquard, Helv. Phys. Acta, 28, 534 (1955)

24 E. H. Putley, 'The Hall Effect and Related Phenomena' (Butterworths, 1960)

25 R. S. Allgaier, J. Appl. Phys., 36 (8), 2429 (1965)

26 J. Black, E. M. Conwell, L. Seigle and C. W. Spencer, J. Phys. Chem. Solids, 2, 240 (1957)

27 O. G. Folberth and H. Weiss, Z. Naturforsch, 10a, 615 (1955)

28 R. R. Heikes and R. W. Ure, Jr., 'Thermoelectricity, Science and Engineering', Interscience, 1961, chapter 13

29 D. M. Bercha, Z. V. Pankevich, A. V. Savitskii and K. D. Tovstyuk, Sov. Phys., Solid St., 7 (8), 1968 (1966)

30 W. B. Pearson, 'Lattice Spacings and Structures of Metals and Alloys', Pergamon, 1958

31 L. S. Ramsdell, Amer. Mineralogist, 15, 119 (1930)

32 P. W. Lange, Naturwissenschaften, 27, 133 (1939)

33 S. A. Semiletov, Kristallografiya, 1 (4), 403 (1956)

34 E. Dönges, Z. Anorg. Chem., 265, 56 (1951)

35 U. Birkholz, Z. Naturforsch., 13a, 780 (1958)

36 W. R. Bekebrede and O. J. Guentert, J. Phys. Chem. Solids, 23, 1023 (1962)

37 M. J. Smith, R. J. Knight and C. W. Spencer, J. Appl. Phys., 33 (7), 2186 (1962)

38 A. Brown and B. Lewis, J. Phys. Chem. Solids, 23, 1597 (1962)

39 E. Mooser and W. B. Pearson, J. Phys. Chem. Solids, 7, 65 (1958)

40 G. F. Koster, Solid State Physics, 5, p. 208 (1957)

41 A. I. Andrievskii, I. D. Nabitovich and Ya. V. Voloshchuk, Sov. Phys., Crystallography, 7 (6), 704 (1963)

42 Sh. Movlanov, G. B. Abdullaev, A. Bashshaliev, A. Kuliev and I. Kerimov, Doklady Akad. Nauk Azerbaidzhan SSR., 17, 375 (1961)

43 V. A. Brodovii and V. I. Lyashenko, Ukr. Fiz. Zh, 6, 664 (1961)

44 L. R. Testardi, J. N. Bierly, Jr. and F. J. Donahoe, J. Phys. Chem. Solids, 23, 1209 (1962)

45 L. Liebe, Ann. der Phys., 7, 15, 179 (1965)

46 T. C. Harman, B. Paris, S. E. Miller and H. L. Goering, J. Phys. Chem. Solids, 2, 181 (1957)

47 W. Eichler and H. Nieke, Wiss. Z. Univ. Halle, Math.-Nat., 13, 1 (1964)

48 J. R. Drabble, Proc. Phys. Soc., 72, 380 (1958)

49 B. A. Efimova, V. I. Novikov and A. G. Ostroumov, Proc. Intern. Conf. Phys. Semicond., Exeter, 1962, 647 Soviet Phys., Solid St., 3, 2004 (1962)

50 R. Jäschke, Ann. der Phys., 15, 106 (1965)

51 M. I. Klinger, Sov. Phys., Solid St., 2 (6), 1231 (1960)

52 Yu. V. Ilisavskii, Sov. Phys., Solid St., 4 (3), 601 (1962)

53 J. E. Parrott and A. W. Penn, Solid St. Phys. Electronics Telecommun., Proc. Intern. Conf. Brussels, 2 (2), 836 (1958)

54 H. Benel, Compt. Rend., 247, 584 (1958)

55 H. Rodot and H. Benel, Solid St. Phys. Electronics Telecommun., Proc. Intern. Conf. Brussels, 2 (2), 692 (1958)

56 F. I. Vasenin, Zh. Tekh. Fiz., 25, 1190 (1955)

57 I. Teramoto and S. Takayanagi, J. Phys. Chem. Solids, 19, 124 (1961)

58 G. V. Kokosh and S. S. Sinani, Sov. Phys., Solid St., 2 (6), 1012 (1960)

59 B. Rönnlund, O. Beckman and H. Levy, J. Phys. Chem. Solids, 26, 1281 (1965)

60 G. B. Abdullaev, A. A. Bashshaliev, S. A. Aliev, M. I. Aliev and I. G. Kerimov, Izv. Akad. Nauk Azerb. SSSR., Ser. Fiz.-Mat. i Tekhn. Nauk 1961 (5), 55

61 P. J. Price, Phil. Mag., 46, 1252 (1955)

62 S. Katsugi, Sumitomo Electric Review, 83, 102 (1963)

63 S. Misra and M. B. Bever, to be published

64 L. R. Testardi and J. R. Wiese, Trans. AIME., 221, 647 (1961)

65 J. R. Drabble, Proc. Phys. Soc., 72, 380 (1958)

66 L. R. Testardi, P. J. Stiles and E. Burstein, Solid St. Comm., 1, 28 (1963)

67 G. Landwehr and P. Drath, Proc. Intern. Conf. Phys. Semicond., Paris, 1964, 669

68 R. Sehr and L. R. Testardi, J. Appl. Phys., 34, 2754 (1963)

69 H. H. Soonpaa, J. Appl. Phys., 34, 3600 (1963)

70 P. M. Lee and L. Pincherle, Proc. Phys. Soc., 81, 461 (1963)

71 E. K. Kudinov, Soviet Phys., Solid St., 3, 227 (1961)

72 I. Ya. Korenblit, Soviet Phys., Solid St., 2, 2738 (1961)

73 B. Yates, J. Electronics and Control, 6, 26 (1959)

74 P. A. Walker, Proc. Phys. Soc., 76, 113 (1960)

75 R. W. Ure, Jr., Proc. Intern. Conf. Phys. Semicond., Exeter, 1962, 653

76 M. J. Smith, J. Appl. Phys., 34, 2879 (1963)

77 J. H. Dennis, Advanc. Energy Conv., 1, 99 (1961)

78 A. Sagar and R. W. Ure, Jr., Proc. Intern. Conf. Phys. Semicond., Paris, 1964, 557

79 A. F. Wells, 'Structural Inorganic Chemistry', Oxford, 1962, p. 662

80 R. T. Sanderson, 'Chemical Periodicity', Reinhold, 1960, p. 96

81 B. W. Howlett, Somnath Misra and M. B. Bever, Trans. AIME., 230, 1367 (1964)

82 J. Lagrenaudie, J. Phys. Radium, 18 (3 suppl.), 39A (1957)

83 J. R. Drabble and C. H. L. Goodman, J. Phys. Chem. Solids, 5, 142 (1958)

84 G. Offergeld and J. van Cakenburghe, J. Phys. Chem. Solids, 11, 310 (1959)

85 G. R. Miller and Che-Yu Li, J. Phys. Chem. Solids, 26, 173 (1965)

86 F. A. Kröger, J. Phys. Chem. Solids, 7, 276 (1958)

87 P. Delavignette and S. Amelinckx, Phil. Mag., 6, 601 (1961)

88 Ya. I Gerasimov and A. V. Nicol'skaya, Proc. 4th All-Union Conf. on Semiconducting Materials, 1963, 22

89 N. N. Koren and N. N. Sirota, Dokl. Akad. Nauk Belorussk. SSR., 7 (10), 666 (1963)

90 R. A. Horne, Solid St. Electronics, 5, 55 (1962)

91 P. Delavignette and S. Amelinckx, Phil. Mag., 5, 729 (1960)

92 M. Hansen and K. Anderko, 'Constitution of Binary Alloys', McGraw-Hill, 1958

93 N. Kh. Abrikosov, L. V. Poretskaya and I. P. Ivanova, Russ. J. Inorg. Chem., 4, 1163 (1959)

94 H. Fay and H. E. Ashley, Amer. Chem. J., 27, 95 (1902)

95 W. Haken, Ann. Phys., (4), 32, 291 (1910)

96 K. Honda and H. Endo, J. Inst. Metals, 37, 29 (1927)

97 H. Pelabon, Compt. Rend., 142, 207 (1906)

98 N. S. Konstantinov and V. I. Smirnov, Izvest. St. Petersburg Politekh. Inst. Imp. Petra Velik, 23, 713 (1915)

99 Y. Kimata, Mem. Coll. Sci, Kyoto Univ., 1, 115-8 (1915)
J. Inst. Metals, 15, 347 (1916)

100 N. Kh. Abrikosov and V. F. Bankima, Zh. Neorg. Khim., 3, 659 (1958)
N. Kh. Abrikosov, V. F. Bankima and K. F. Kharitonovich, Russ. J. Inorg. Chem., 5, 978 (1960)

101 L. V. Poretskaya, N. Kh. Abrikosov and V. M. Glazov, Russ. J. Inorg. Chem., 8, 620 (1963)

102 A. J. Rosenberg and A. J. Strauss, J. Phys. Chem. Solids, 19, 105 (1961)

103 J. S. Anderson, Advances in Chemistry Series, 39, 1 (1963)

104 M. M. Stasova, J. Struct. Chem., 5, 731 (1964)

105 H. V. Warren and M. A. Peacock, Univ. Toronto Studies, Geol. Series, (49), 55 (1945)

106 A. A. Godovikov, J. Struct. Chem., 3, 38 (1962)

107 G. F. Gubskaya and I. V. Evfimovskii, Russ. J. Inorg. Chem., 7, 834 (1962)

108 D. R. Mason and J. S. Cook, J. Appl. Phys., 32, 475 (1961)
D. J. Barber, J. Appl. Phys., 35, 398 (1964)

109 E. A. D. White, G.E.C. Journal, 31, 43 (1964)

110 A. J. Goss, J. Metals, 5, 1085 (1953)

111 W. W. Piper, J. Chem. Phys., 20, 1343 (1952)

112 A. C. Prior, Conf. on Metallurgical Aspects of Semiconductors, Birmingham, 1958
J. Electrochem. Soc., 108, 82 (1961)

113 G. A. Kurov, S. A. Semiletov and Z. G. Pinsker, Sov. Phys., Doklady, 1, 604 (1956)

114 J. Czochralski, Z. Physik. Chem., 92, 219 (1917)

115 J. N. Shive, 'The Properties, Physics and Design of Semiconductor Devices', van Nostrand, 1959

116 D. C. Stockbarger, Rev. Sci. Instr., 7, 133 (1936)

117 W. G. Pfann, Trans. A.I.M.E., 194, 747 (1952)

118 C. Hamann, Phys. Stat. Solidi, 12, 498 (1965)

119 N. B. Hannay, 'Semiconductors', Reinhold, 1959

120 E. Billig, Proc. Roy. Soc., 235A, 37 (1956)

121 J. van den Boomgaard, F. A. Kröger and H. J. Vink, J. Electronics, 1, 212 (1955)

122 B. D. Wedlock and F. M. Norton, Proc. Conf. Ultrapurification of Semiconductor Materials, Boston, 1961, 84

123 G. V. Kidson, J. Nucl. Mater., 3, 21 (1961)

124 J. Bloem, Philips Res. Repts., 11, 273 (1956)
M. J. Smith, Appl. Phys. Letters, 1, 79 (1962)

125 W. Biltz and R. Juza, Z. Anorg. Chem., 190, 161 (1930)
J. B. Westmore, K. H. Mann and A. W. Tickner, J. Phys. Chem., 68, 606 (1964)

126 T. I. Kucher, Sov. Phys., Solid St., 3, 401 (1961)

127 B. I. Boltaks, Zh. Tekh. Fiz., 25, 767 (1955)

128 A. A. Kuliev and G. B. Abdullaev, Sov. Phys., Solid St., 1, 545 (1959)

129 A. M. Samarin, J. Iron Steel Inst., 200, 95 (1962)
E. N. Nikitin and V. K. Zaitsev, Instrum. and Expt. Techniques, no 4, 952 (1965)

130 C. A. Bryant and J. B. Gunn, Rev. Sci. Instr., 36, 1614 (1965)

131 E. W. Johnson and H. H. Johnson, Rev. Sci. Instr., 35, 1510 (1964)

132 R. G. Mazur and D. H. Dickey, Spring Meeting of the Electrochemical Society, 1963
J. Electrochem. Soc., 113, 255 (1966)

133 E. E. Gardner, J. F. Hallenback, Jr. and P. A. Schumann, Jr., Solid St. Electronics, 6, 311 (1963)

134 L. B. Valdes, Proc. I.R.E., 42, 420 (1954)
A. Uhlir, Jr., Bell Syst. Tech. Jour., 34, 105 (1955)
F. Keywell and G. Dorosheski, Rev. Sci. Instr., 31, 833 (1960)
D. E. Vaughan, Brit. J. Appl. Phys., 12, 414 (1961)

135 A. Mircea, Solid St. Electronics, 6, 459 (1963)

136 J. Hornstra and L. J. van der Pauw, J. Electronics and Control, 17, 169 (1959)
J. D. Wasscher, Philips Res. Repts., 16, 301 (1961)
L. J. van der Pauw, Philips Res. Repts., 16, 187 (1961)

137 J. K. Hargreaves and D. Millard, Brit. J. Appl. Phys., 13, 231 (1962)

138 L. J. van der Pauw, Philips Res. Repts., 13, 1 (1958)

139 J. N. Hummel, Trans. A.I.M.E. (Geophysical Prospecting), 1932, p. 392

140 A. F. Stevenson, Physics, 5, 114 (1934)

141 G. N. Watson, 'Theory of Bessel Functions', Cambridge University Press, 1952

142 J. C. van Dam, Thesis, Delft (1964) (Publ. Uitgeverij Waltman, Delft, 1964)

143 H. Hora, Zeit. fur angew. Phys. 15, 491 (1963)

144 V. L. Kon'kov, Sov. Phys., Solid St., 6, 1747 (1965)

145 P. A. Schumann, Jr. and E. E. Gardner, Trans. A.I.M.E., 233, 602 (1965)

146 C. L. Pekeris, Geophysics, 5, 31 (1940)

147 L. B. Slichter, Physics, 4, 307, (1933)

148 R. E. Langer, Bull. Amer. Math. Soc., 39, 814 (1933)
42, 747 (1936)

149 L. V. King, Proc. Roy. Soc., 139A, 237 (1933)

150 H. Margenau and G. M. Murphy, 'The Mathematics of Physics and Chemistry' (van Nostrand, 1956)

151 R. Maillet and H. G. Doll, Gerlands Beitr. z. Geoph. Ergänzungs Hefte für Angewandte Geoph., 3, 109 (1932)
R. Maillet, Geophys., 12, 529 (1947)

152 M. Cutler, Advanced Energy Conv., 2, 29 (1962)

153 M. Cutler, J. Appl. Phys., 32, 1075 (1961)

154 T. M. Dauphinee and S. B. Woods, Rev. Sci. Instr., 26, 693 (1955)

155 J. Mathews and R. L. Walker, 'Mathematical Methods of Physics' (Benjamin, 1964)

156 F. A. Cunnell and C. H. Gooch, J. Phys. Chem. Solids, 15, 127 (1960)

157 G. I. Guseva and I. M. Tsidil'kovskii, Sov. Phys., Solid St., 5, 191 (1963)

158 G. E. Tauber, J. Phys. Chem. Solids, 23, 7 (1962)

159 I. M. Longman, Proc. Camb. Phil. Soc., 52, 764 (1956)
Math. Tables, Aids Comp., 11, 166 (1957)

ACKNOWLEDGEMENTS

The author wishes to express his gratitude to Dr. J. S. Llewelyn Leach for his help and guidance throughout the course of this work.

He is indebted to Professor J. G. Ball for the provision of laboratory facilities.

Thanks are due to the Science Research Council for financial support and to those members of the technical staff of Imperial College who have given their assistance at various stages of the work.

The author would like to thank his wife. She has contributed much, both through her continued patience and through discussions on all aspects of the work. But for her, the work could not have been completed.

Appendix I

Summary of Electronic Transport Formulae

Various parameters of the electronic system in solids are here stated in terms of the basic functions set out in section 2.2.

i Fermi distribution function; the probability of occupation of a state with energy ε (relative to the band extremum),

$$f(\eta, \eta_F) = (1 + \exp((\eta - \eta_F)/kT))^{-1} \qquad (A1.1)$$

where η is the 'reduced' energy ε/kT

η_F equals ε_F/kT

ε_F is the 'Fermi energy'.

ii Fermi-Dirac integrals (see page 17)

$$F_n(y) = \int_0^\infty x^n . f(x,y) . dx \qquad (A1.2)$$

For $y < -2$, $F_n(y) \approx e^y (n + 1)$ (A1.3)

For $y > 5$, $F_n(y) \approx y^{n+1}/(n + 1)$ (A1.4)

iii Effective mass; the inertial mass of an electron in a solid differs from the free electron mass because of the interaction with the potential of the crystal lattice. For a non-degenerate band extremum the reciprocal effective mass tensor is defined by

$$(1/m)_{ij} = \frac{1}{h^2} \cdot \frac{\partial^2 \varepsilon(\underline{k})}{\partial k_i \partial k_j} \qquad (A1.5)$$

Various other effective masses may be defined in terms of the components of the diagonalised effective mass tensor. Important is the 'density of states effective mass',

$$m_N = N^{2/3}(m_1\ m_2\ m_3)^{1/3} \qquad (A1.6)$$

for the case of a non-degenerate band with N equivalent ellipsoidal valleys.

iv Scattering mechanisms; any deviation from periodicity in the lattice causes scattering of current carriers.

Acoustic phonons cause a dilatation of the lattice and hence a change of potential of the energy bands. The varying potential scatters carriers and there is an (approximately isotropic) relaxation time

$$\tau \propto \varepsilon^{-1/2} . m^{-3/2} . T^{-1} \qquad (A1.7)$$

Optical phonons in non-polar crystals scatter carriers by a similar mechanism. At high temperatures the magnitude of scattering is generally of the same order as that due to acoustic phonons. In polar crystals, optical modes cause polarisation of the lattice. At high temperatures a relaxation time exists for scattering by this process,

$$\tau \propto \varepsilon^{-\frac{1}{2}} . m^{-\frac{1}{2}} . T^{-1} \qquad \text{(A1.8)}$$

Ionised impurity scattering is of importance chiefly at low temperatures. The relaxation time cannot be expressed in a simple form like A1.7 or A1.8.

Scattering of current carriers may occur, under suitable conditions, between different bands or between different valleys of the same band.

v Mobility; defined, for a single type of current carrier, from the simple expression for electrical conductivity,

$$\sigma = ne\mu \qquad \text{(A1.9)}$$

where σ is the conductivity, n is the carrier density, e is the electronic charge and μ is the mobility. The 'Hall mobility' is defined from the assumption that the Hall coefficient, R_H, equals $(ne)^{-1}$.

vi Carrier density; in a simple parabolic band the effective density of current carriers equals

$$n = 4\pi(2m^*/h^2)^{3/2} \int_0^\infty \varepsilon^{\frac{1}{2}}.f(\eta, \eta_F).d\varepsilon$$

$$= 4\pi(2m^* kT/h^2)^{3/2} F_{\frac{1}{2}}(\eta_F) \qquad \text{(A1.10)}$$

where m^* is the effective mass, k is Boltzmann's constant and h is Planck's constant.

vii Electrical conductivity; for a single band

$$\sigma = -\frac{16\pi}{3} e^2 \frac{(2m^*)^{\frac{1}{2}}}{h^3} \int_0^\infty \tau(\varepsilon).\varepsilon^{3/2}.\frac{\partial f}{\partial \varepsilon}.d\varepsilon \qquad \text{(A1.11)}$$

For $\tau \propto \varepsilon^p.m^{*q}.T^r$,

$$\sigma \propto m^{*(q + \frac{1}{2})}.T^{(p + r + 3/2)}.(p + 3/2).F_{p + \frac{1}{2}}(\eta_F) \qquad \text{(A1.12)}$$

For two bands, the conductivities of each band are summed to give the total,

$$\sigma = \sigma_1 + \sigma_2 \qquad \text{(A1.13)}$$

viii Hall coefficient; for a single band and weak magnetic field is

$$R_H = -{}^3/2 \cdot \frac{(2p + {}^3/2)}{(p + {}^3/2)^2} \cdot \frac{F_{\frac{1}{2}}(\eta_F) \cdot F_{2p + \frac{1}{2}}(\eta_F)}{F^2_{p + \frac{1}{2}}(\eta_F)} \cdot \frac{1}{ne} \qquad (A1.14)$$

For two bands having conductivities σ_1 and σ_2 and Hall coefficients R_1 and R_2 respectively,

$$R = (R_1\sigma_1^2 + R_2\sigma_2^2)/(\sigma_1 + \sigma_2)^2 \qquad (A1.15)$$

ix Thermoelectric power; for a single band,

$$\alpha = \frac{k}{e}\left[\eta_F - \frac{(2p + 5)\, F_{p + {}^3/2(\eta_F)}}{(2p + 3)\, F_{p + {}^1/2(\eta_F)}}\right] \qquad (A1.16)$$

For two bands,

$$\alpha = (\alpha_1\sigma_1 + \alpha_2\sigma_2)/(\sigma_1 + \sigma_2) \qquad (A1.17)$$

Appendix II

The Distribution of Electric Potential in Inhomogeneous Media which are Anisotropic in the Horizontal Plane

The problem described at the end of section 4.3.iii is discussed. We consider the potential distribution due to a point source of current on the surface of a semi-infinite anisotropic medium. The medium possesses three independent components to its conductivity tensor. One of the principal directions lies perpendicular to the surface of the medium, $z = 0$. The other principal directions are taken as the x and y axis in a Cartesian coordinate system. The principal conductivities σ_x, σ_y and σ_z depend only on the z coordinate and possess generally different functional forms. The source is at the origin of coordinates.

A formulation similar to that of section 4.3.i is required and is presented here. A transformation of the medium like that of section 4.3.iii may always be applied to make the situation isotropic in either the (x, z) or (y, z) plane, so we consider only the case $\sigma_x(z) = \sigma_z(z) \neq \sigma_y(z)$.

Starting with the equation representing charge conservation, div $\underline{j} = 0$, the equation for the potential may be derived.

$$\frac{\partial^2 V}{\partial x^2} + h(z)\frac{\partial^2 V}{\partial y^2} + \frac{\partial^2 V}{\partial z^2} + f(z)\frac{\partial V}{\partial z} = 0 \qquad \text{(A2.1)}$$

where $h(z) = \sigma_y/\sigma_z$ (A2.2)

and $f(z) = \frac{1}{\sigma_z}\frac{d\sigma_z}{dz}$ (A2.3)

Equation A2.1 is separable. Putting $V(x, y, z) = X(x).Y(y).Z(z)$ we obtain

$$X''/X = -\theta^2 \qquad \text{(A2.4)}$$

$$Y''/Y = -\gamma^2 \qquad \text{(A2.5)}$$

$$Z'' + f(z).Z' - (\theta^2 + \gamma^2 h(z)).Z = 0 \qquad \text{(A2.6)}$$

θ and γ are the separation constants. Equations A2.4 and A2.5 have the relevant solutions

$$X = A_1\cos(\theta x) \text{ and } Y = A_2\cos(\gamma y) \qquad \text{(A2.7)}$$

respectively.

The integral over all values of θ and γ of the product of X, Y, Z and a weighting function $K_1(\theta, \gamma)$ gives the potential distribution V(x, y, z).

$$V(x,y,z) = Q \int_0^\infty d\theta.\cos(\theta x) \int_0^\infty d\gamma.\cos(\gamma y).Z(\theta,\gamma,z).K_1(\theta,\gamma) \qquad (A2.8)$$

Q is the source strength. $K_1(\theta,\gamma)$ is to be found.

The quantity $(\frac{\partial V}{\partial z})_{z=0}$ equals zero and is independent of the conductivity profile, i.e. the function Z does not appear in the expression for $(\frac{\partial V}{\partial z})_{z=0}$. Thus $K_1(\theta,\gamma)$ must contain a factor $(\frac{dZ}{dz})_{z=0}$ in its denominator. Writing $K_1(\theta,\gamma) = K_2(\theta,\gamma)/(\frac{dZ}{dz})_{z=0}$, the boundary condition gives

$$0 = \int_0^\infty d\theta.\cos(\theta x) \int_0^\infty d\gamma.\cos(\gamma y).K_2(\theta,\gamma) \qquad (A2.9)$$

In the sense that

$$\int_0^\infty dp.\cos(qp) = \lim_{r \to 0} \int_0^\infty dp.\cos(qp).\exp(-rp)$$

$$= \lim_{r \to 0} r/(r^2 + q^2)$$

$$= 0$$

the equation A2.9 is satisfied by $K_2(\theta,\gamma)$ = constant.

The value of the constant may be found by evaluating A2.8 for the homogeneous, isotropic case. The result is that $K_2(\theta,\gamma) = -2/\pi$. Hence

$$V(x,y,z) = -\frac{2Q}{\pi}\int_0^\infty d\theta.\cos(\theta x)\int_0^\infty d\gamma.\cos(\gamma y).\frac{Z(\theta,\gamma,z)}{Z'(\theta,\gamma,0)} \qquad (A2.10)$$

The function $K(\theta,\gamma,z) = -\frac{2}{\pi}Z(\theta,\gamma,z)/Z'(\theta,\gamma,0)$ serves the same purpose as the similarly defined kernel function in equation 4.8. Equation A2.10 may be inverted to read

$$K(\theta,\gamma,z) = \frac{4}{\pi^2}\int_0^\infty dx.\cos(\theta x)\int_0^\infty dy.\cos(\gamma y).V(x,y,z) \qquad (A2.11)$$

This is the equivalent of equation 4.10.

Appendix III

i Radial Heat Flow from an Oscillating Source

Consider a uniform half-space defined by the spherical coordinates (r, φ, θ), $0 \leqslant \theta \leqslant \frac{1}{2}\pi$. The time is t. A point source of heat (H(t) energy units/time) at r = 0 produces a temperature distribution T(r, t) in the medium of thermal conductivity k. T approaches zero for large values of r. The strength of the heat source is

$$Q(t) = H(t)/2\pi k. \qquad (A3.1)$$

The equation governing the temperature distribution is (ref. 150)

$$\nabla^2 T - \frac{1}{a^2}\frac{\partial T}{\partial t} = 0 \qquad (A3.2)$$

where a^2, the thermal diffusivity, equals $(k/\rho s)$. ρ is the density and s the specific heat of the medium.

As the simplest case of an oscillating source consider $Q(t) = Q_0 \sin wt = -i.\mathrm{Im}(Q_0 e^{iwt})$ where $i = (-1)^{\frac{1}{2}}$ and w is the angular frequency of the source. Then clearly T(r, t) is also periodic in t.

$$T(r,t) = T_o(r)\sin wt$$

$$= -i.\mathrm{Im}(T_o(r).e^{iwt}) \qquad (A3.3)$$

Substituting A3.3 into A3.2 gives

$$\frac{\partial^2 T_o}{\partial r^2} + \frac{2}{r}.\frac{\partial T_o}{\partial r} - \frac{iw}{a^2}T_o = 0 \qquad (A3.4)$$

since A3.2 is true at all times. Equation A3.4 is easily solved using the substitution $W = Tr$, giving

$$T_o(r) = \frac{Q_o}{r}.\exp(-\frac{r}{a}(\tfrac{1}{2}w)^{\frac{1}{2}}(1+i)) \qquad (A3.5)$$

where use was made of the known solution for $w = 0$,

$$T_o(r)_{w=0} = \frac{Q_o}{r} \qquad (A3.5a)$$

Thus, substituting A3.5 into A3.3, the temperature distribution due to the oscillating source is obtained:-

$$T(r,t) = \frac{H_o}{2\pi kr}.e^{-\frac{r}{a}(\frac{1}{2}w)^{\frac{1}{2}}}.\sin(wt - \frac{r}{a}(\tfrac{1}{2}w)^{\frac{1}{2}}) \qquad (A3.6)$$

This expression represents a spherical, exponentially damped wave of velocity $a(2w)^{\frac{1}{2}}$.

ii The Measured Thermal Effect

The actual generation of heat by the source depends, in the present experimental situation, on the current waveform. The heat source may be considered as a series of sinusoidal oscillators whose strengths are known by Fourier analysis.

$$Q(t) = \sum_{n=1}^{\infty} q_n \sin(nwt) \qquad (A3.7)$$

The temperature distribution due to each component source, of angular frequency nw, may be found from A3.6 and the total found by addition.

$$T(r,t) = \sum_{n=1}^{\infty} \frac{q_n}{r} . e^{-r\gamma n^{1/2}} . \sin(nwt - r\gamma n^{1/2}) \qquad (A3.8)$$

where

$$\gamma = (\tfrac{1}{2}w)^{1/2}/a \qquad (A3.9)$$

In the specimen under investigation, this temperature generated a thermoelectric e.m.f. which altered the potential of the potential measuring probe by an amount $a\Delta T$. (a is the thermoelectric power.) Each half cycle the connections to the potential probes were reversed so that the mean output potential was

$$\underline{U}(r) = \alpha \int_{0}^{2\pi} T(r,t).\beta(wt).d(wt) \qquad (A3.10)$$

where

$$\beta(wt) = \begin{cases} 1 & , \ 0 < wt < \pi \\ -1 & , \ \pi < wt < 2\pi. \end{cases}$$

Hence,

$$\underline{U}(r) = \frac{\alpha}{\pi^2 r} \sum_{\substack{n=1 \\ n \text{ odd}}}^{\infty} \frac{q_n}{n} .e^{-r\gamma n^{1/2}} .\cos(r\gamma n^{1/2}) \qquad (A3.11)$$

The Fourier analysis of the current waveform in the experiment (Figure 18, ii), i.e.

$$Q(t) = \begin{cases} 0 & , \quad 0 < t < \tfrac{1}{2}A \\ S & , \quad \tfrac{1}{2}A < t < \tfrac{1}{2}A + B \\ 0 & , \quad \tfrac{1}{2}A + B < t < 3A/2 + B \\ -S & , \quad 3A/2 + B < t < 3A/2 + 2B \\ 0 & , \quad 3A/2 + 2B < t < 2A + 2B \end{cases} \qquad (A3.12)$$

yields the q_n of A3.7. Putting $R = {}^{1}/_{4A/(A + B)}$

$$q_n = \begin{cases} \dfrac{4S}{\pi n}\cos(2\pi nR) & , \text{ n odd} \\ 0 & , \text{ n even} \end{cases} \qquad \text{(A3.13)}$$

The source strength amplitude, S, is given in the present case by the Peltier heat generation at the current contact (Π, the Peltier coefficient, equals α times absolute temperature, T_a).

$$S = \frac{\Pi I_{max}}{2\pi k} \qquad \text{(see A3.1)}$$

I_{max} is the current amplitude. The experimentally measured current (the mean absolute value) is $I = I_{max}(1 - 4R)$.

Hence the expression for the measured effect of the thermoelectric potentials arising from the Peltier effect at a small electrode is derived.

$$\underline{U}(r) = \frac{4\alpha^2 T_a I}{\pi^3 r(1-4R)k} \sum_{\substack{n=1 \\ n \text{ odd}}}^{\infty} n^{-2}.\exp(-r\gamma n^{1/2}).\cos(r\gamma n^{1/2}).\cos(2\pi Rn) \qquad \text{(A3.14)}$$

The constant R accounts for the current waveform; γ, α and k include the constants of the medium.

iii An Alternative Expression for the Temperature Distribution

An expression giving the temperature distribution T(r, t) equivalent to A3.8 may be found by considering the heat source waveform to be composed of a series of step functions. The temperature due to a single step function is determined. The series representing T(r, t) is then written down by taking into account the time differences between the steps. Using section 7.16 of reference 150 and equation A3.5.a

$$T(r,t) = \frac{H'}{2\pi kr} \sum_{n=0}^{\infty} (-1)^n \left[\operatorname{erf}\left(\left(t + \frac{n\pi}{w} \right)^{-\frac{1}{2}} \frac{r}{2a} \right) + \operatorname{erf}\left(\left(t + \frac{R}{w} + \frac{n\pi}{w} \right)^{-\frac{1}{2}} \frac{r}{2a} \right) \right] \qquad (A3.15)$$

where H' is the rate of heat generation when current flows.

Equation A3.15 is most useful in determining the temperature distribution at times close to one of the steps in the square waveform.

Appendix IV

List of Symbols

a	thermal diffusivity
a_{Hex}	hexagonal lattice parameter
A_i	parameter for fitting experimental data
$b_i(z)$	ith coefficient in $v(z, \theta)$ (eq. 4.17)
$B_i(z)$	$b_i(z)/c(z)$
c_{Hex}	hexagonal lattice parameter
$c(z)$	normalised conductivity, $\sigma(z)/\sigma(\infty)$
$D_i(z)$	function of $B_i(z)$ (eq. 4.23)
f	Fermi distribution function
$F_n(y)$	Fermi-Dirac function of order n
$f(z)$	function derived from $\sigma(z)$ (eq. 4.3)
$g(z)$	anisotropy function (eq. 4.33)
I	current
Im	imaginary part
$\underline{j}$	current density
k	wave number
	thermal conductivity
	Boltzmann's constant
$\underline{k}$	wave vector
$k(\theta)$	kernel function (eq. 4.9)
n	carrier concentration
$n(k)$	density of states

P_i, Q_i, R_i	functions of $B_i(z)$ (eq. 4.30)
Q	source strength
$R(r)$	separation function in 4.4
$R_{AB,CD}$	transfer characteristic in van der Pauw method
R_H	Hall coefficient
r	radial coordinate
s	position of specimen surface
T	temperature
$u(z)$	$c(z)^{-2}$
V	electric potential
$v(z,\Theta)$	function defined by 4.13
$W(z)$	$(c(z).g(z))^{-2}$
X	stoichiometric deviation
z	a coordinate
$Z(z)$	separation function in 4.4
α	thermoelectric power
γ	separation constant in A2.1
ε	energy of current carrier
ε_F	Fermi energy
η	reduced energy, ε/kT
η_F	reduced Fermi energy
Θ	separation constant in 4.4 and A2.1
λ	weighting function

μ	mobility
Π	Peltier coefficient
ρ_{ij}	resistivity
ρ_{ijk}	Hall coefficient
σ	conductivity of isotropic medium
	geometric mean conductivity in anisotropic me[illegible]
τ	relaxation time
φ	angular coordinate
Ψ	potential/current due to electrical point sour[illegible]
Ω	total potential/current

List of Tables

Table	page	
1	202	Published data on electrical conductivity of antimony telluride at room temperature
2	202	Published data on thermoelectric power of antimony telluride at room temperature
3	121	Properties of layers removed from diffused specimen 2-27A
4	123	Typical set of potential measurements
5	131	Parameters derived from the potential distribution for specimen 2-27A

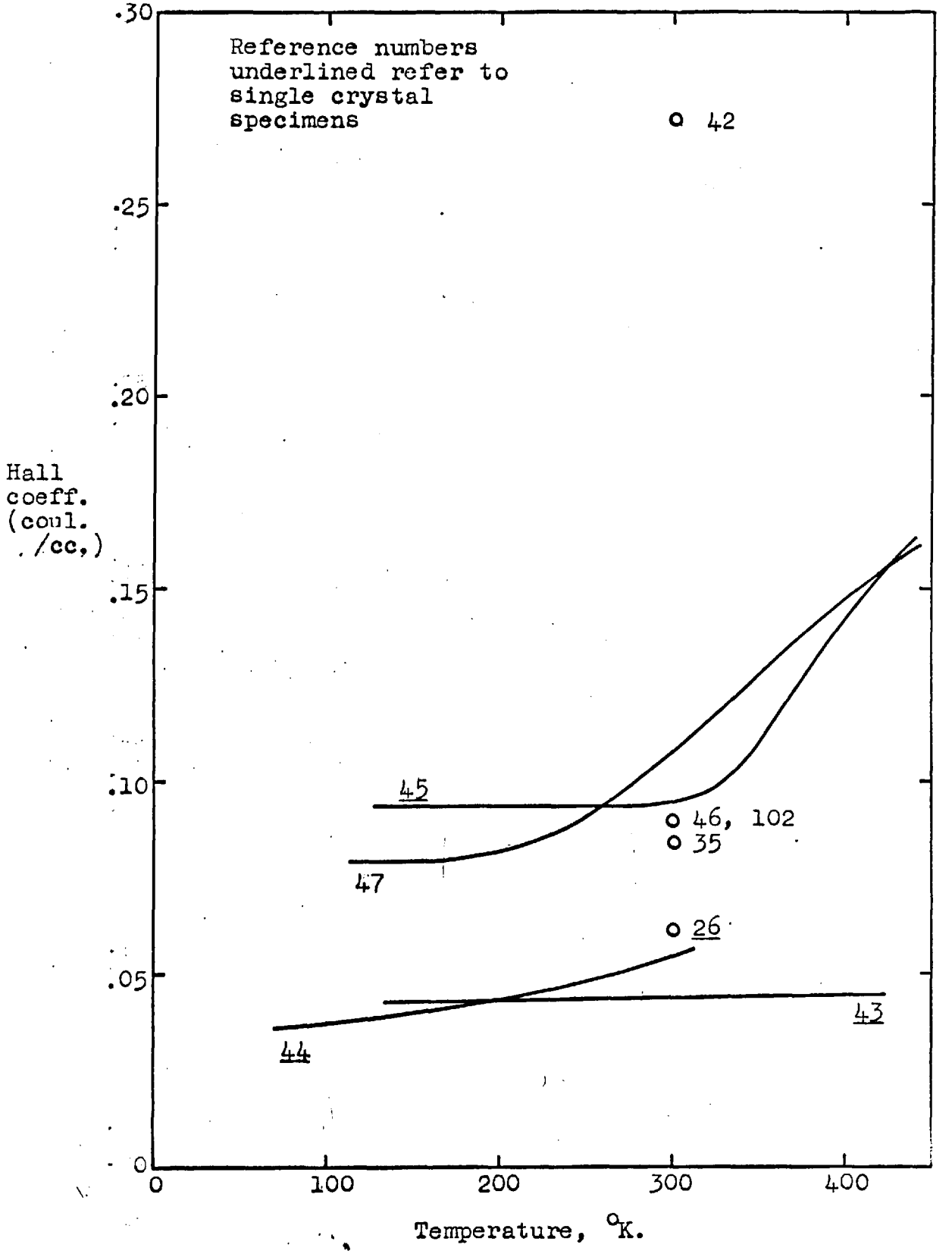


Figure 1. Published Hall coefficient data for Sb_2Te_3 as a function of temperature.

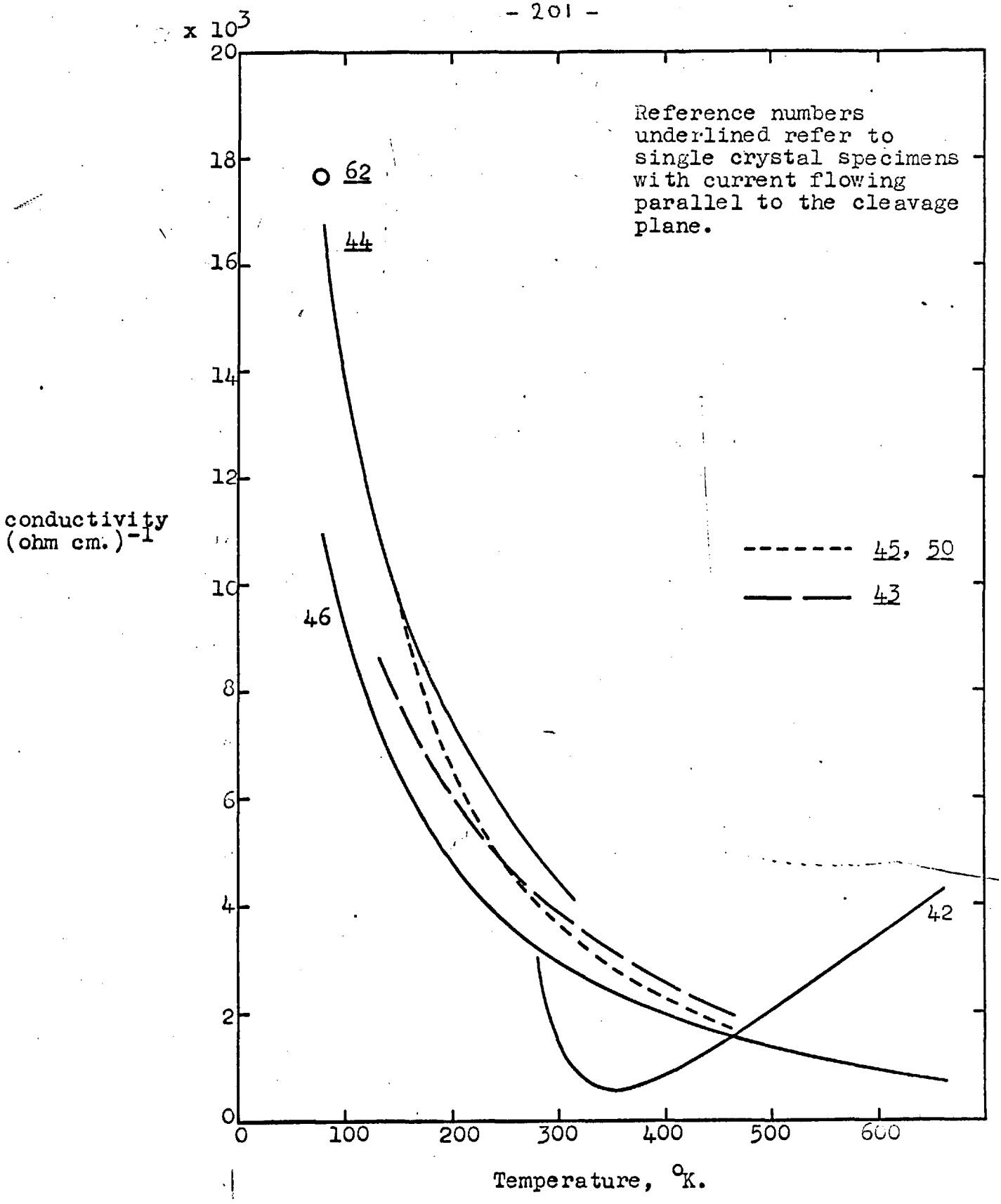


Figure 2. Published electrical conductivity data for Sb_2Te_3 as a function of temperature.

Table 1

Published data on electrical conductivity of antimony telluride at room temperature

Conductivity $(ohm.cm)^{-1}$	Crystalline state	Reference
5000	m	26
4770	p	3
4380	p	35
4300	m	44
3970	m	43
3620	m	45, 50
3330	p	58
3150	p	56
3050	p	46
2850	p	102
2250	p	55
1400	p	42

m - monocrystalline, refers to σ_{11}
p - polycrystalline

Table 2

Published data on thermoelectric power of antimony telluride at room temperature

Thermoelectric power, $\mu V/^{o}C$	Reference
106	56
102	58
100	57
87	53
83	55
82.5	43
81	93
80	46
79	35
77	44
70	102
30	42

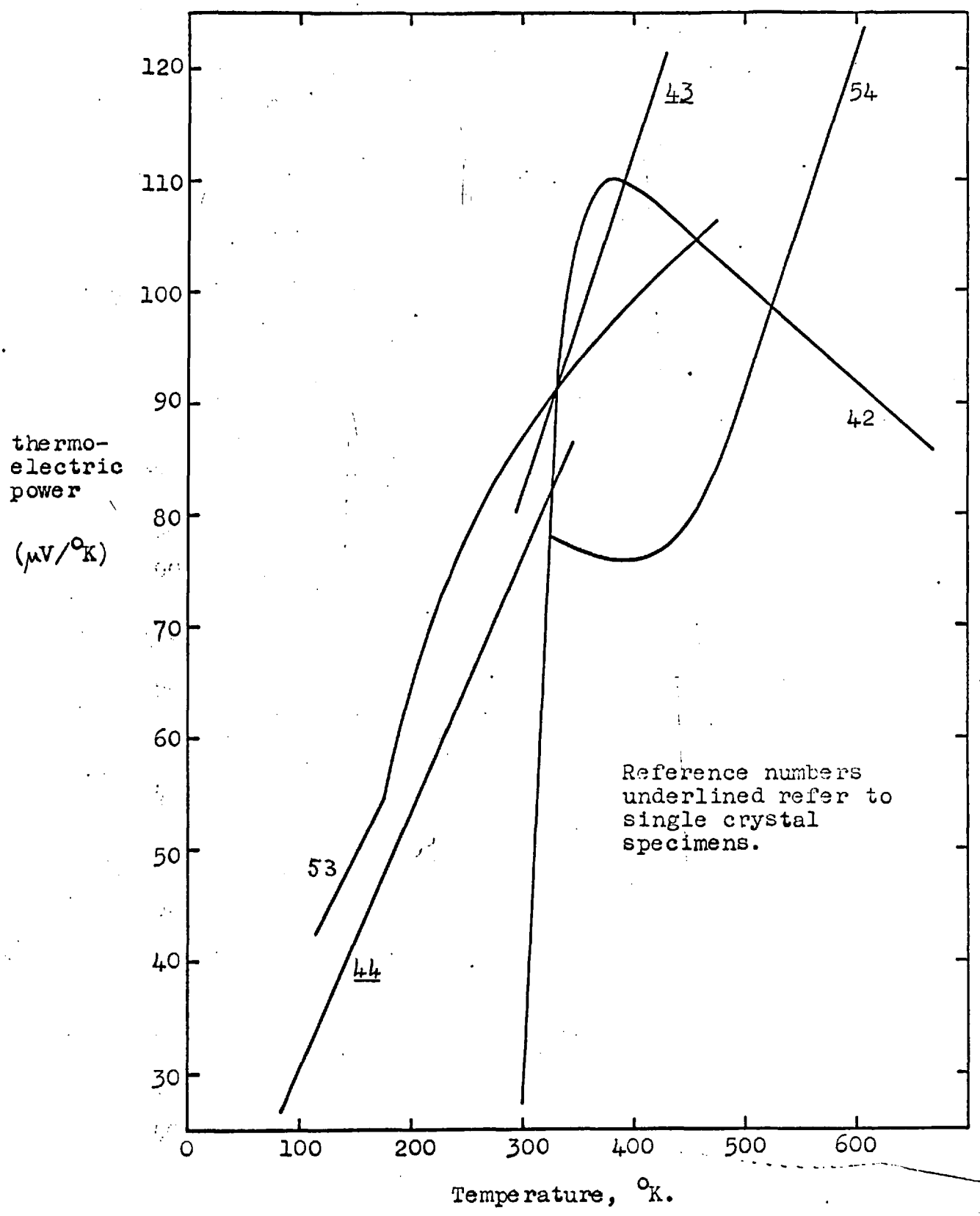


Figure 3. Published thermoelectric power data for Sb_2Te_3 as a function of temperature.

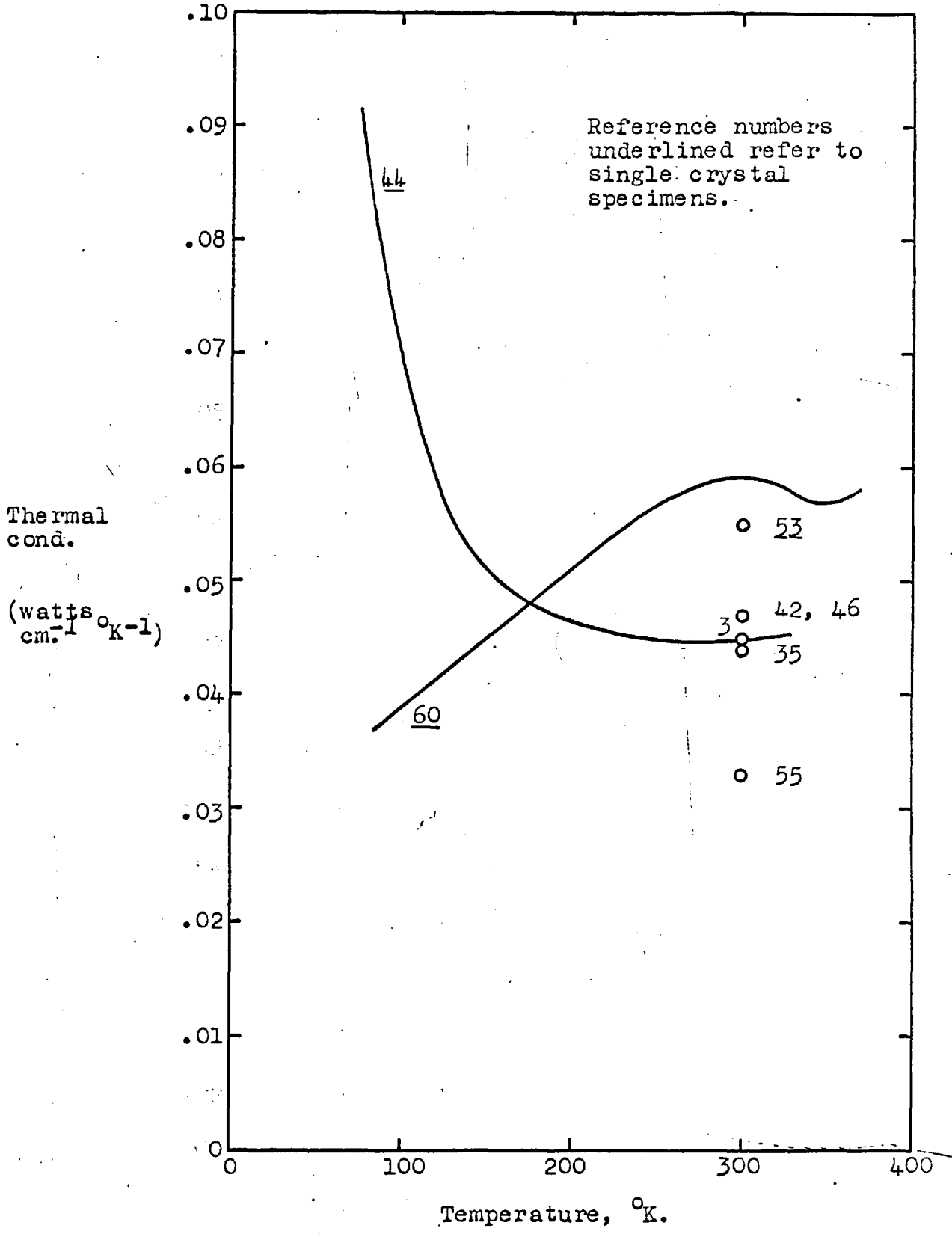
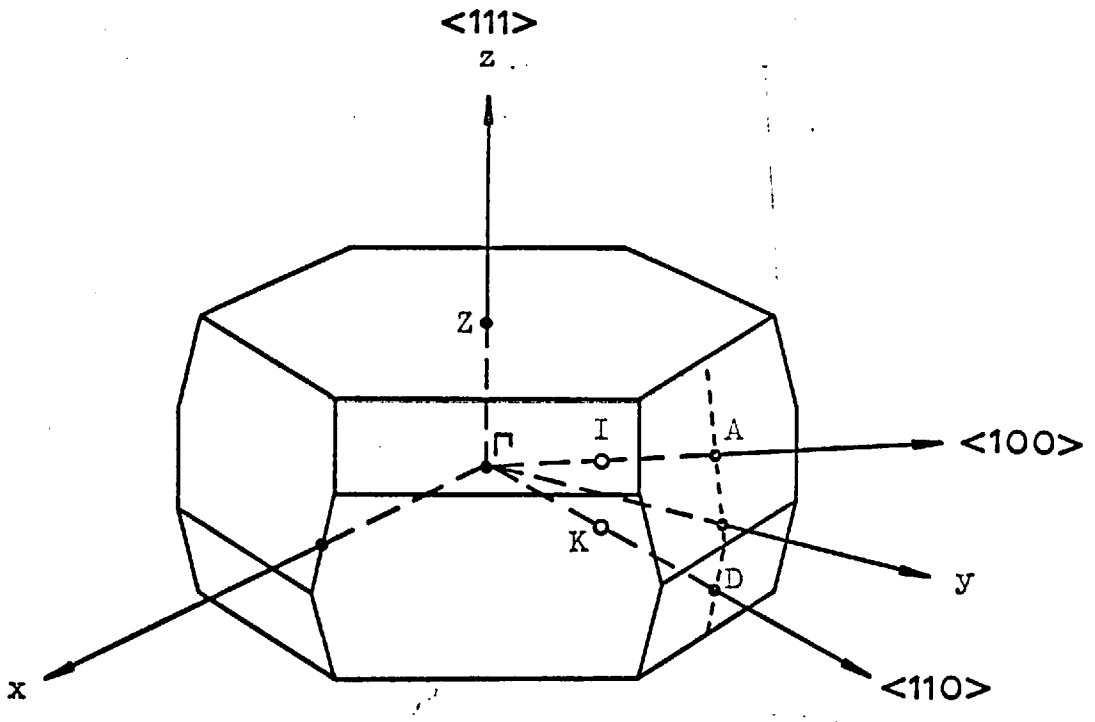


Figure 4. Published thermal conductivity data for Sb_2Te_3 as a function of temperature.



Vertical scale elongated by about 50%.

Figure 5. Brillouin zone of Sb_2Te_3.

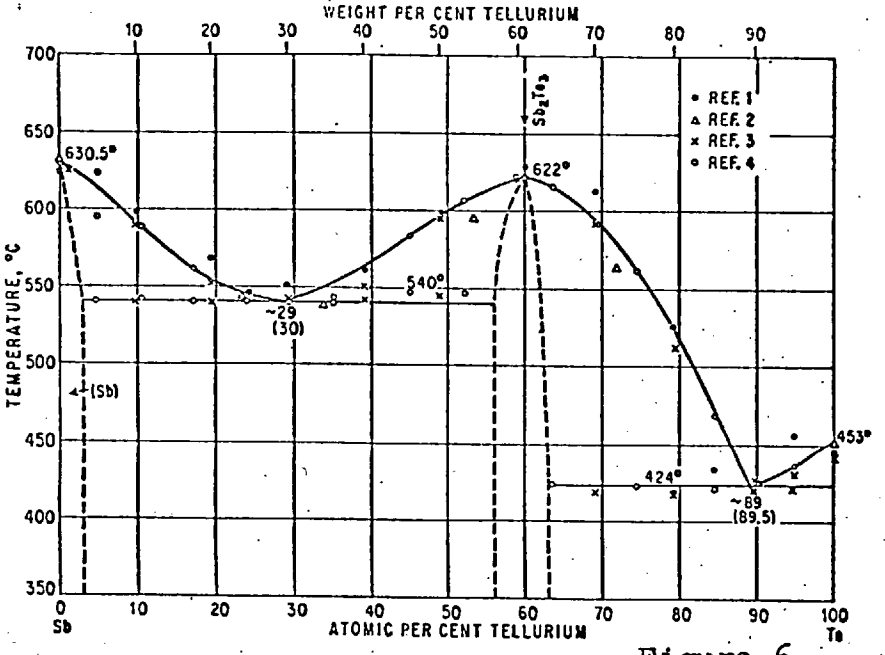


Figure 6

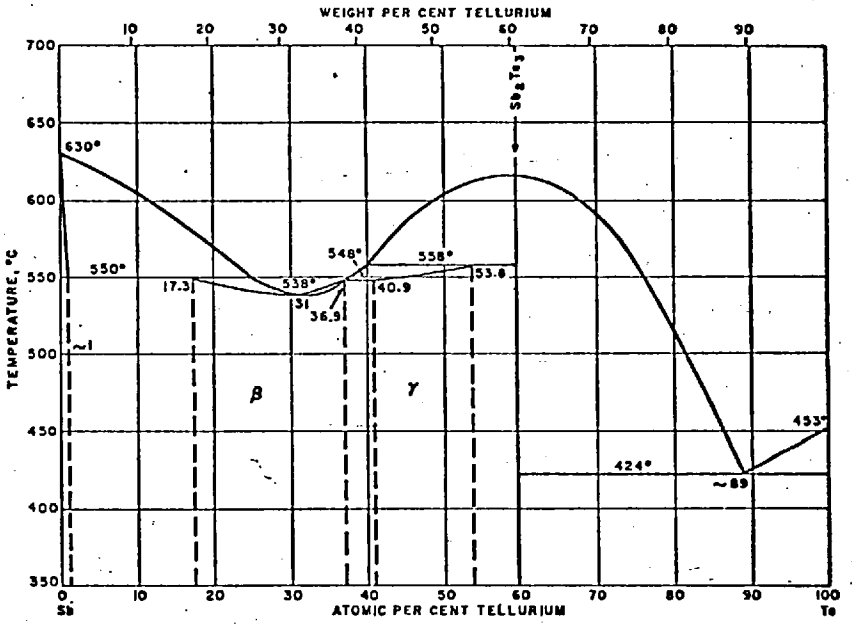
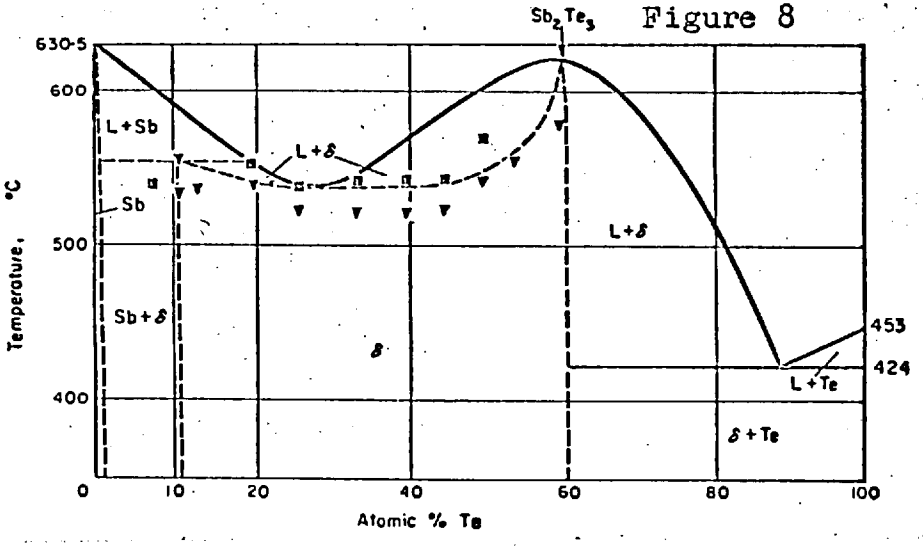


Figure 7

Figure 8



Equilibrium phase diagram for the Sb-Te system after

Hansen - Figure 6

Abrikosov - Figure 7

Brown - Figure 8

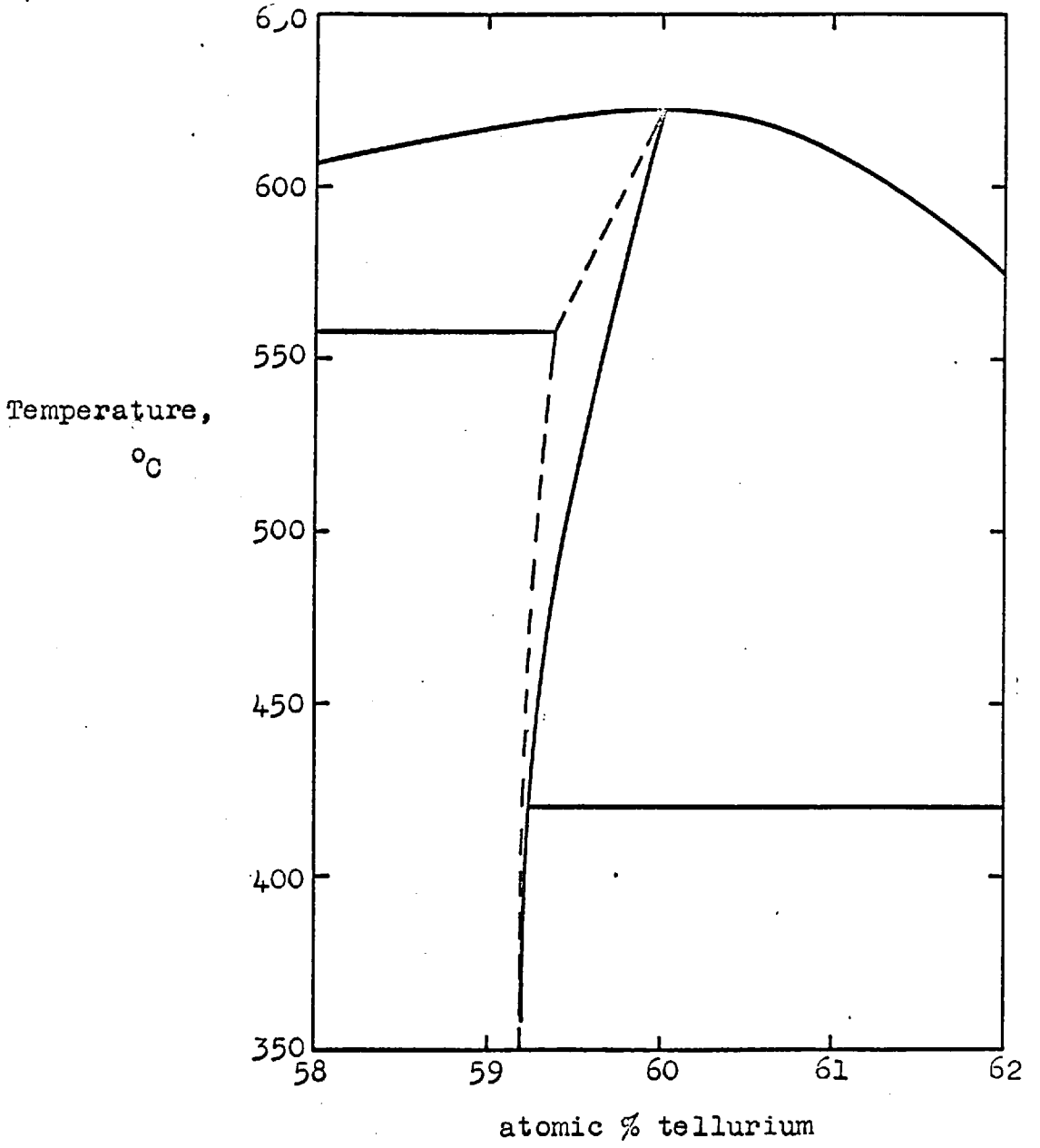


Figure 9. Equilibrium phase diagram near Sb_2Te_3 after Poretskaya. (ref. 101)

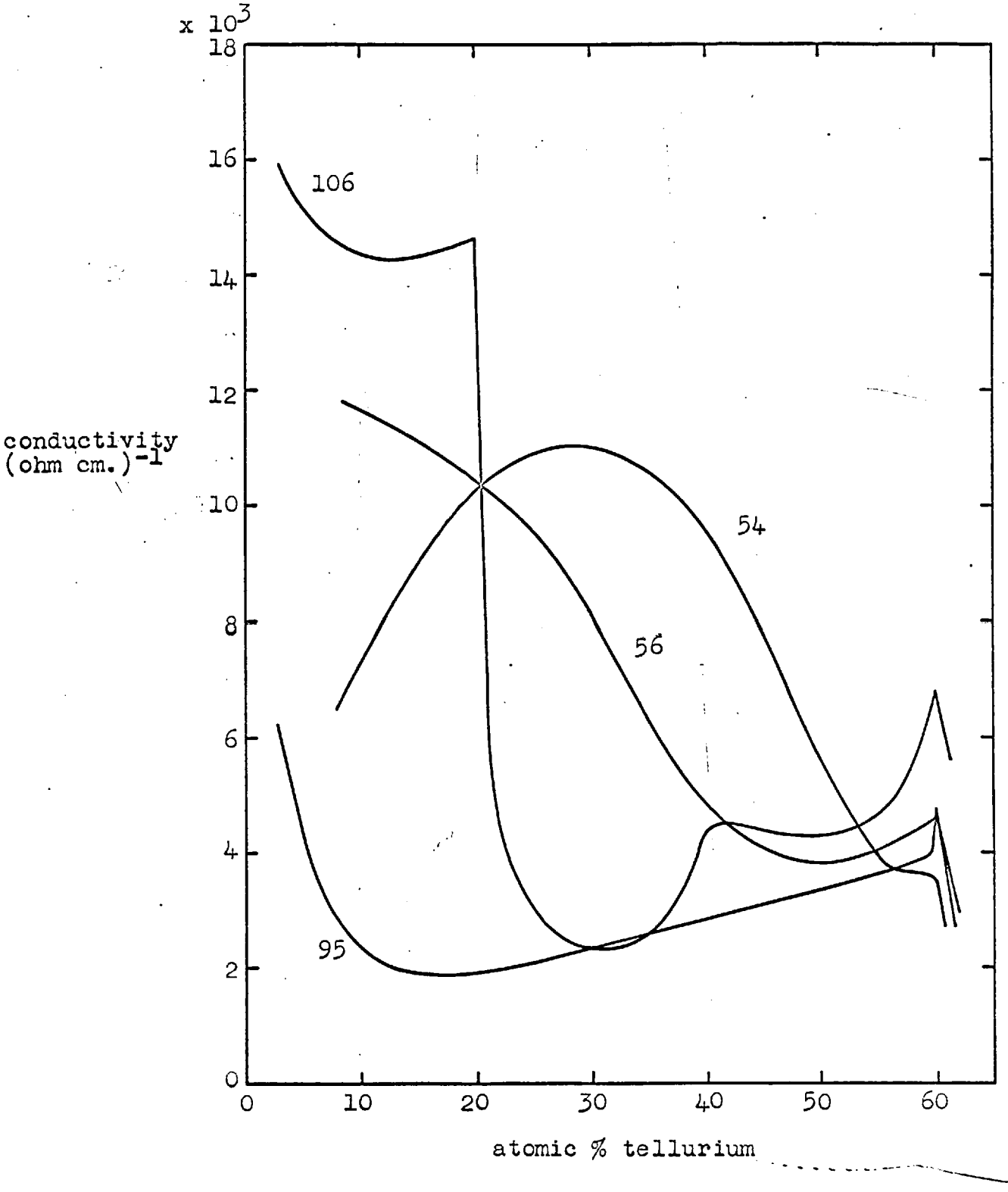


Figure 10. Published electrical conductivities of alloys of Sb and Te in the range Sb - Sb_2Te_3 at room temperature.

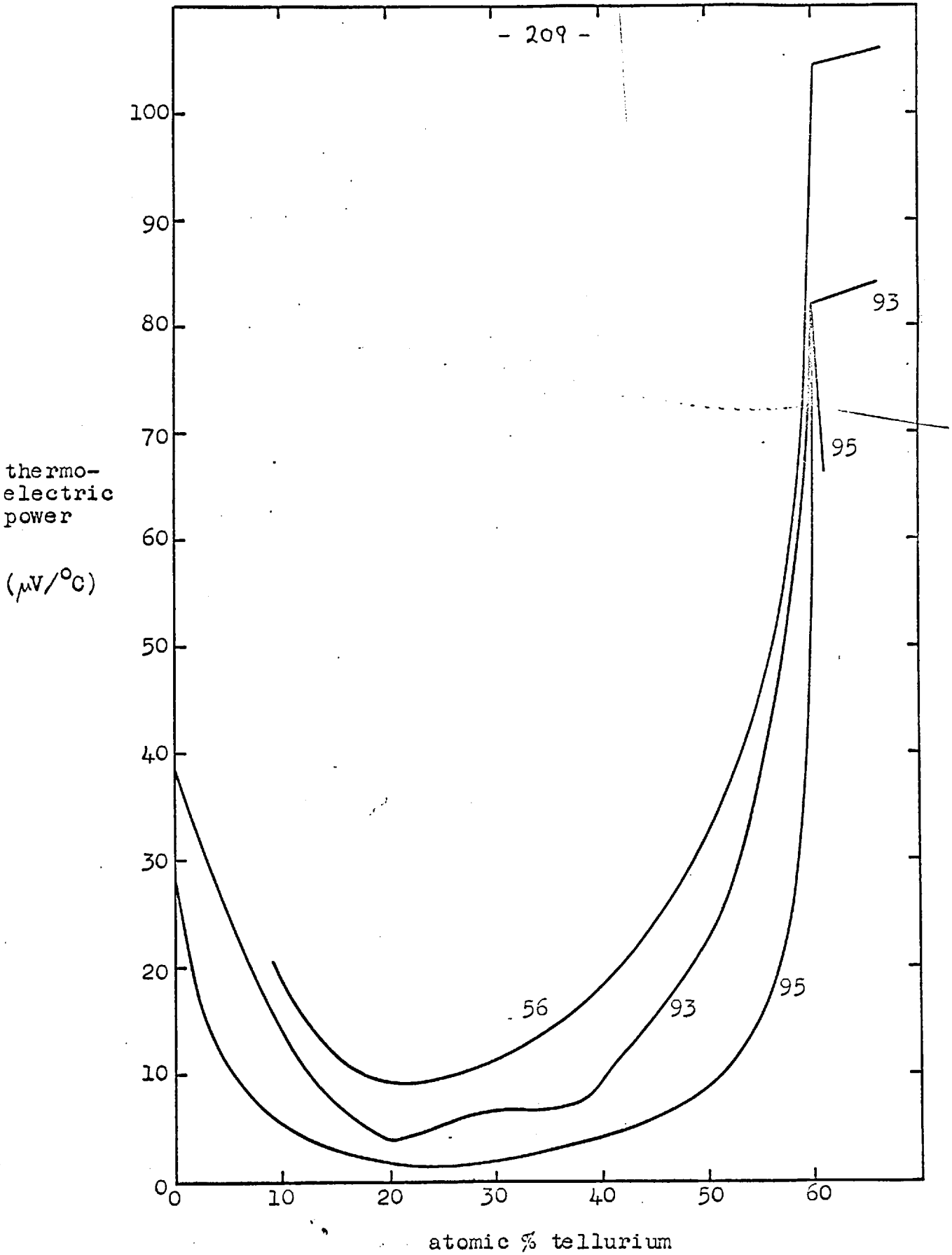


Figure 11. Published thermoelectric powers of alloys of Sb and Te in the range Sb - Sb_2Te_3 at room temperature.

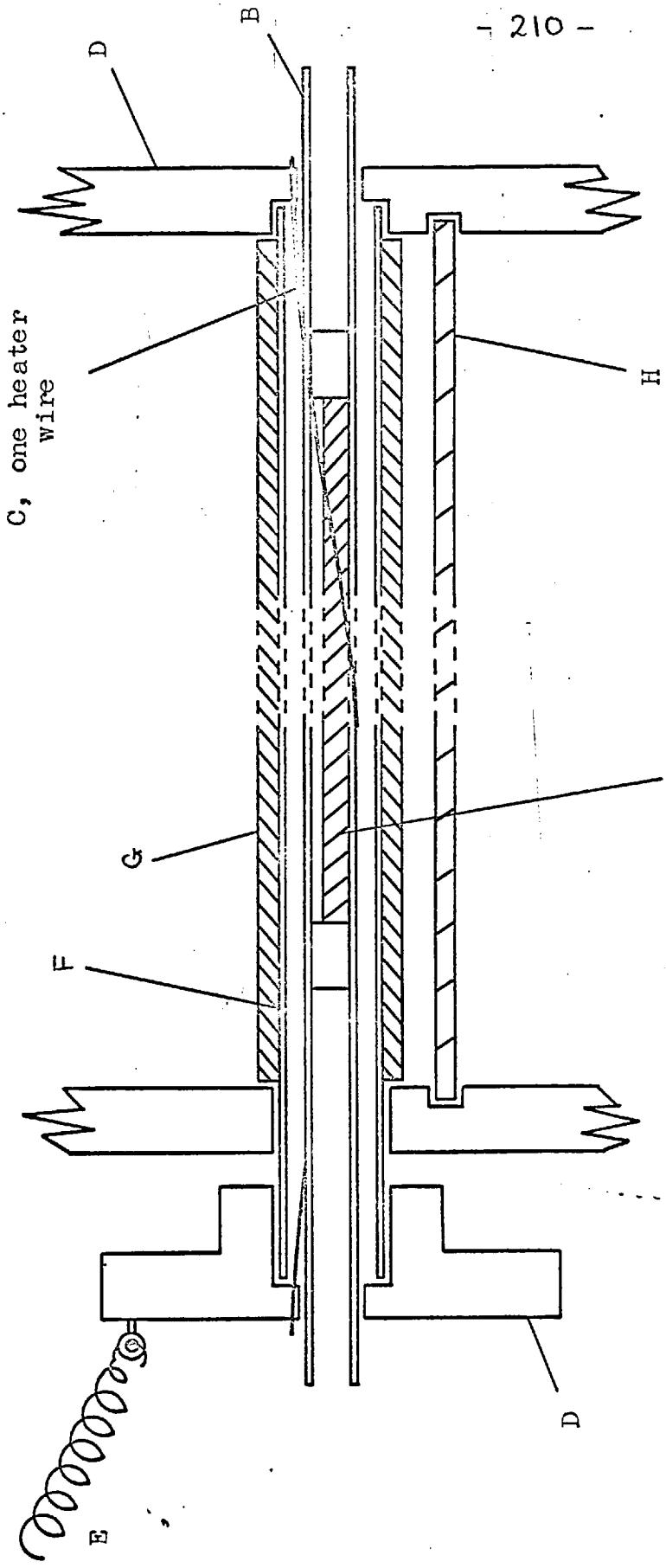


Figure 12. Construction of zone melter.

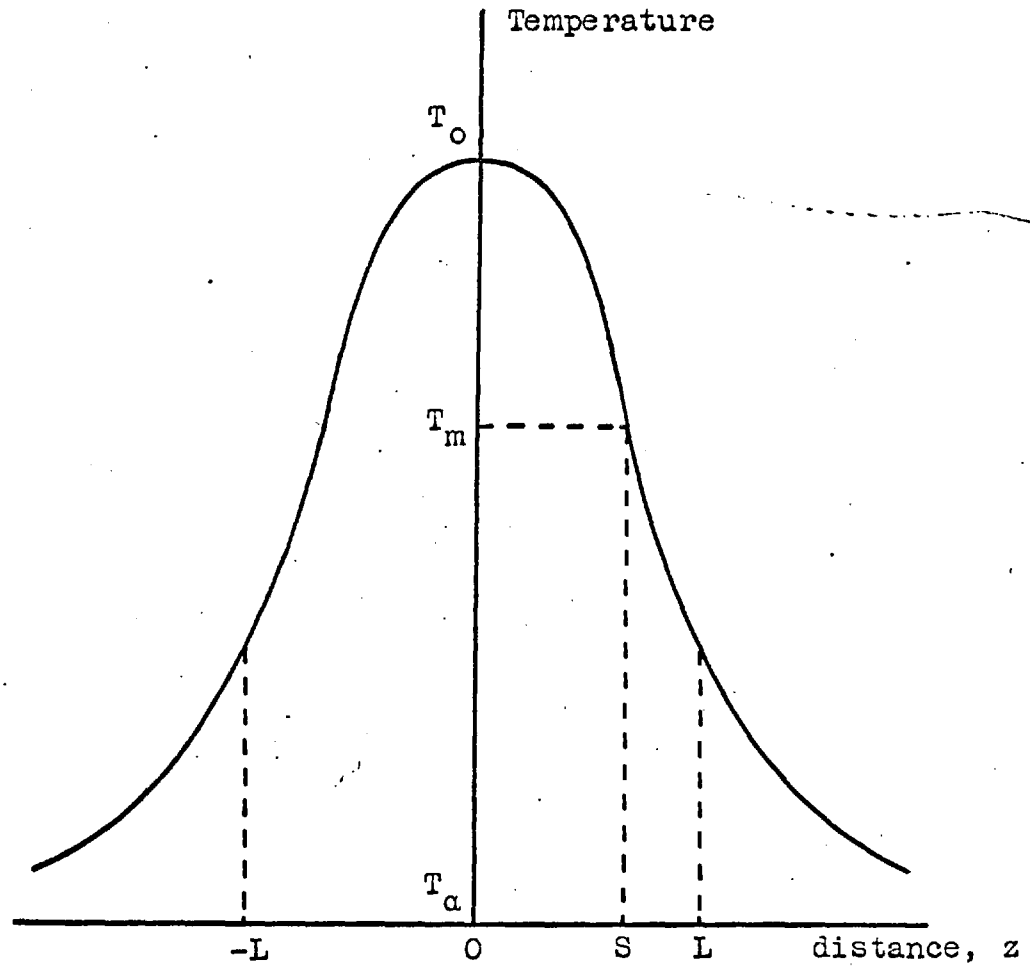


Figure 13. Temperature distribution in furnace during crystal growth.

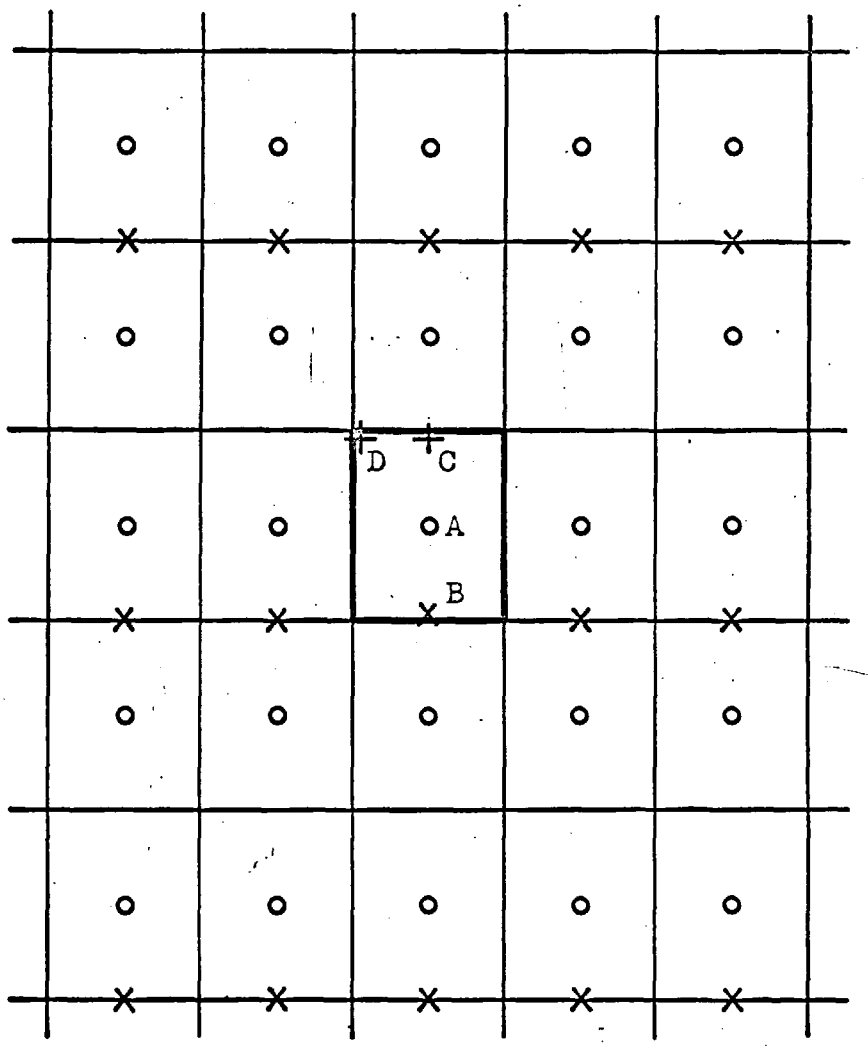


Figure 14. Images of sources A and B in rectangular specimen.

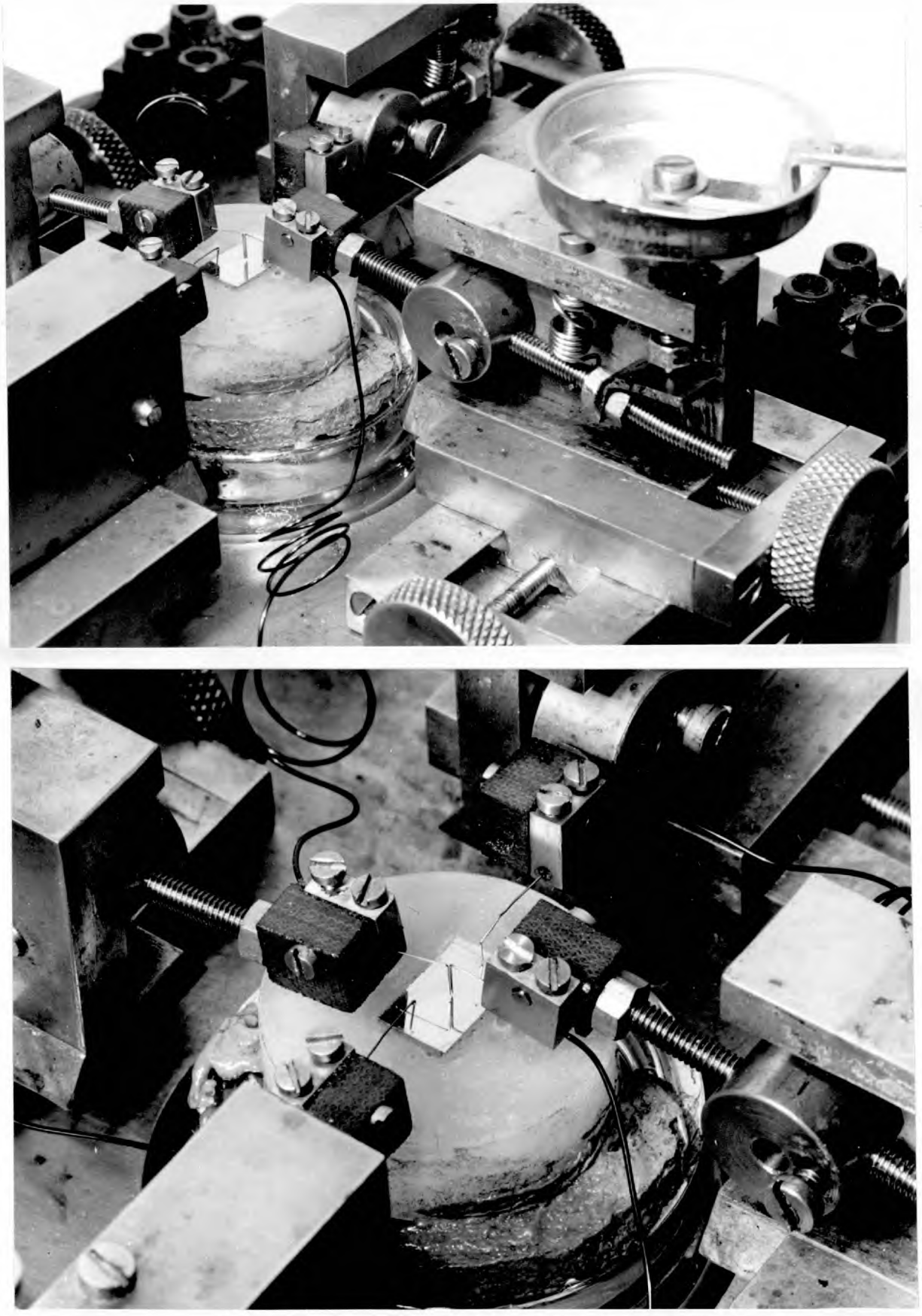


Figure 15. The Four Probe Apparatus.

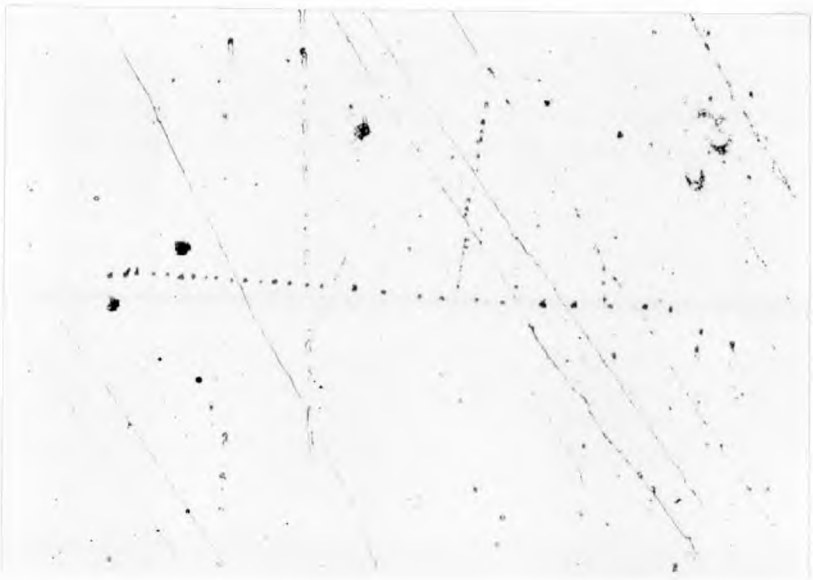


Figure 16. A typical photograph for the measurement of probe spacing. (Corresponds to the results of table 4 and figure 22. Scale, 1 cm = 50.5 microns)

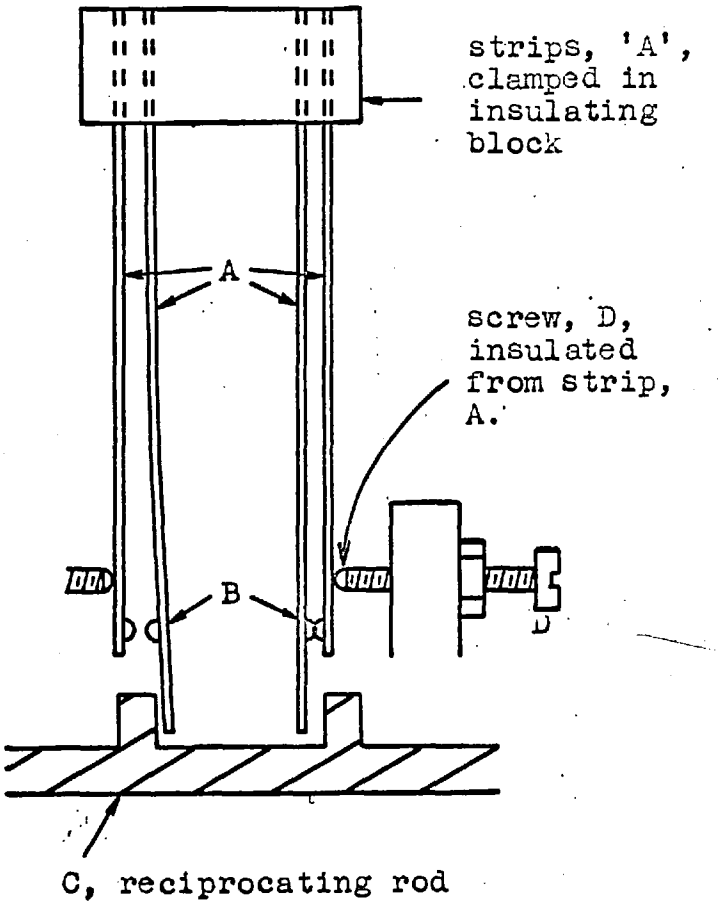


Figure 17. Chopper mechanism.

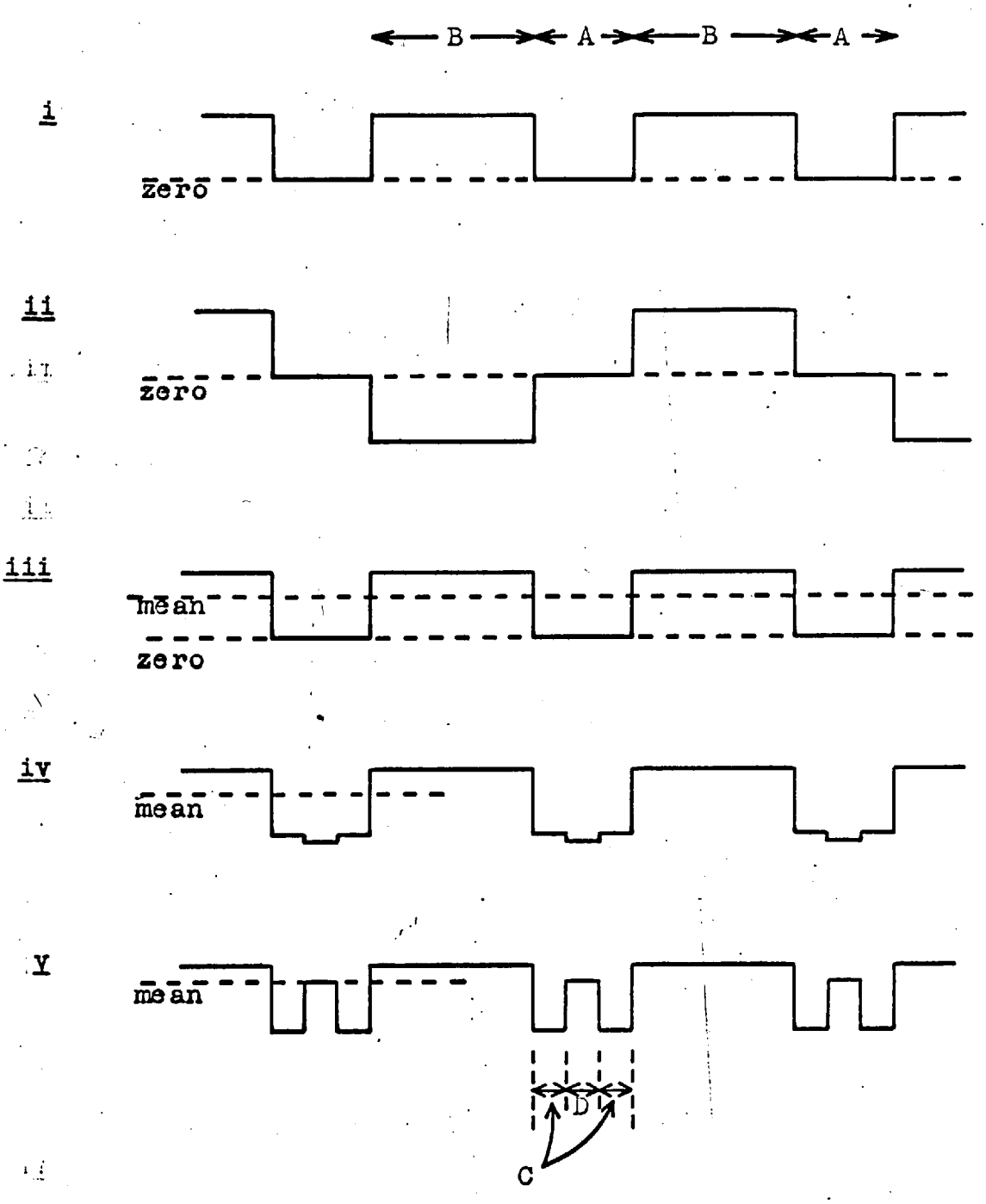


Figure 18. Chopper waveforms.

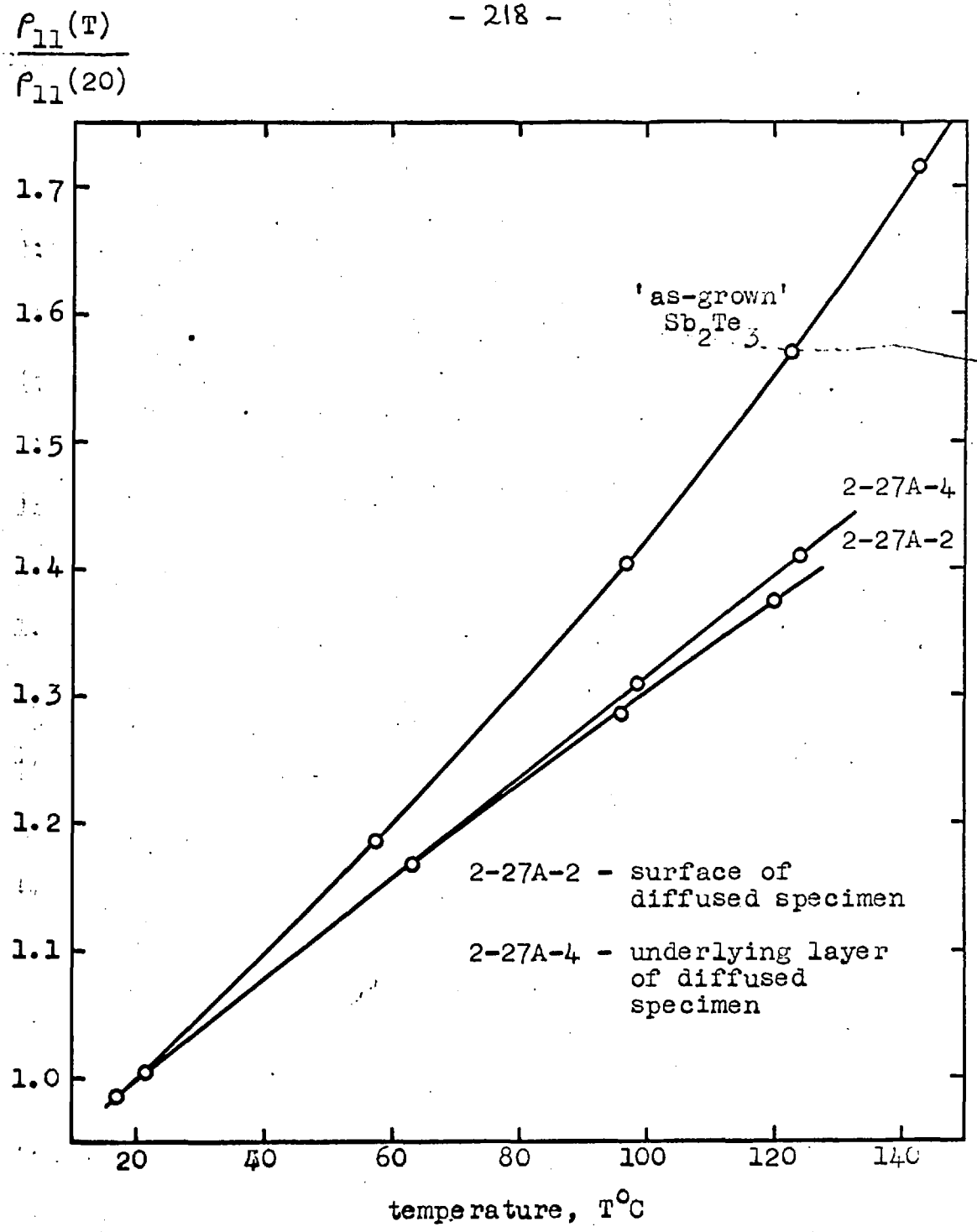


Figure 19. Radial resistivity temperature dependence.

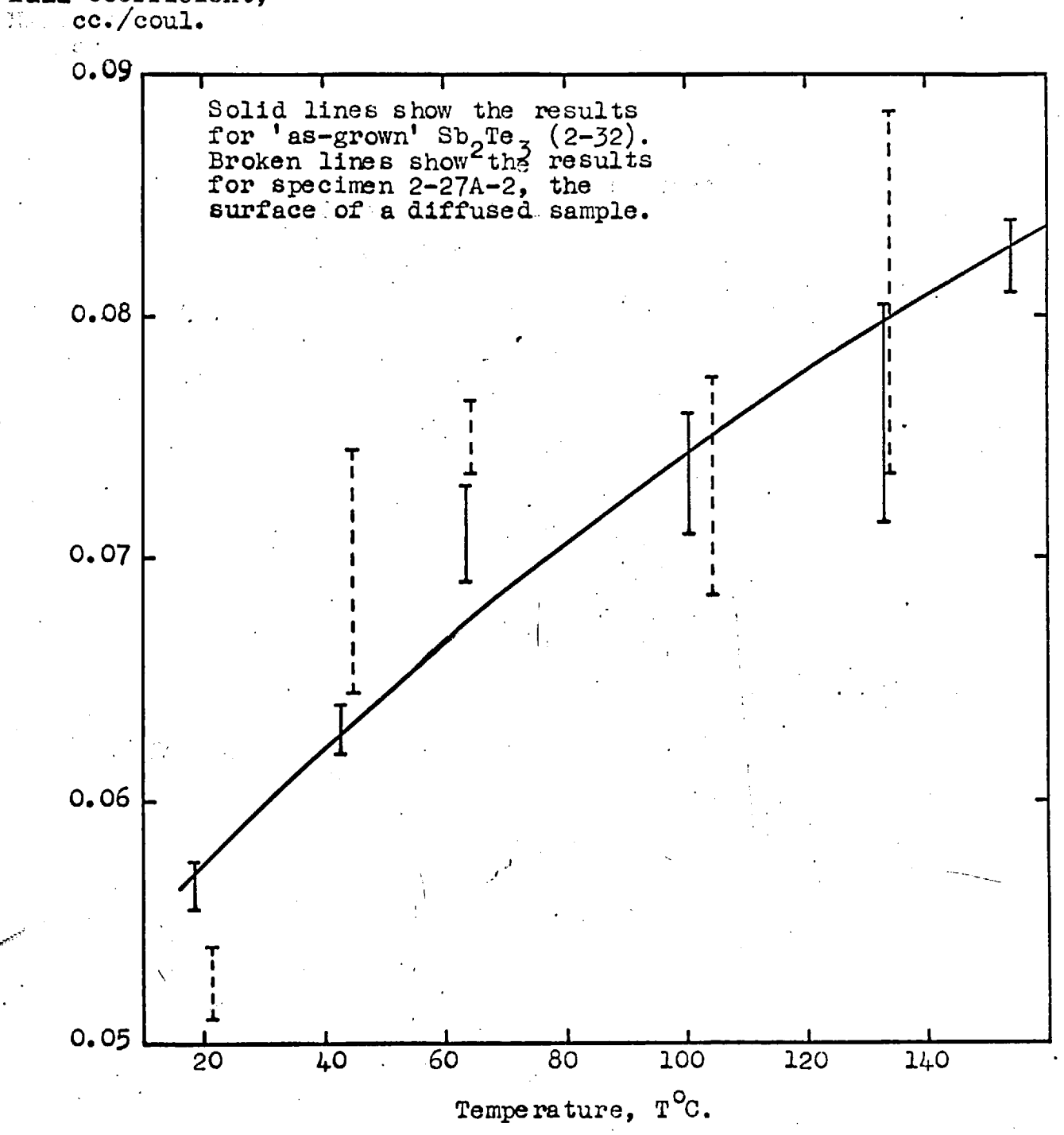


Figure 20. Temperature dependence of the Hall coefficient.

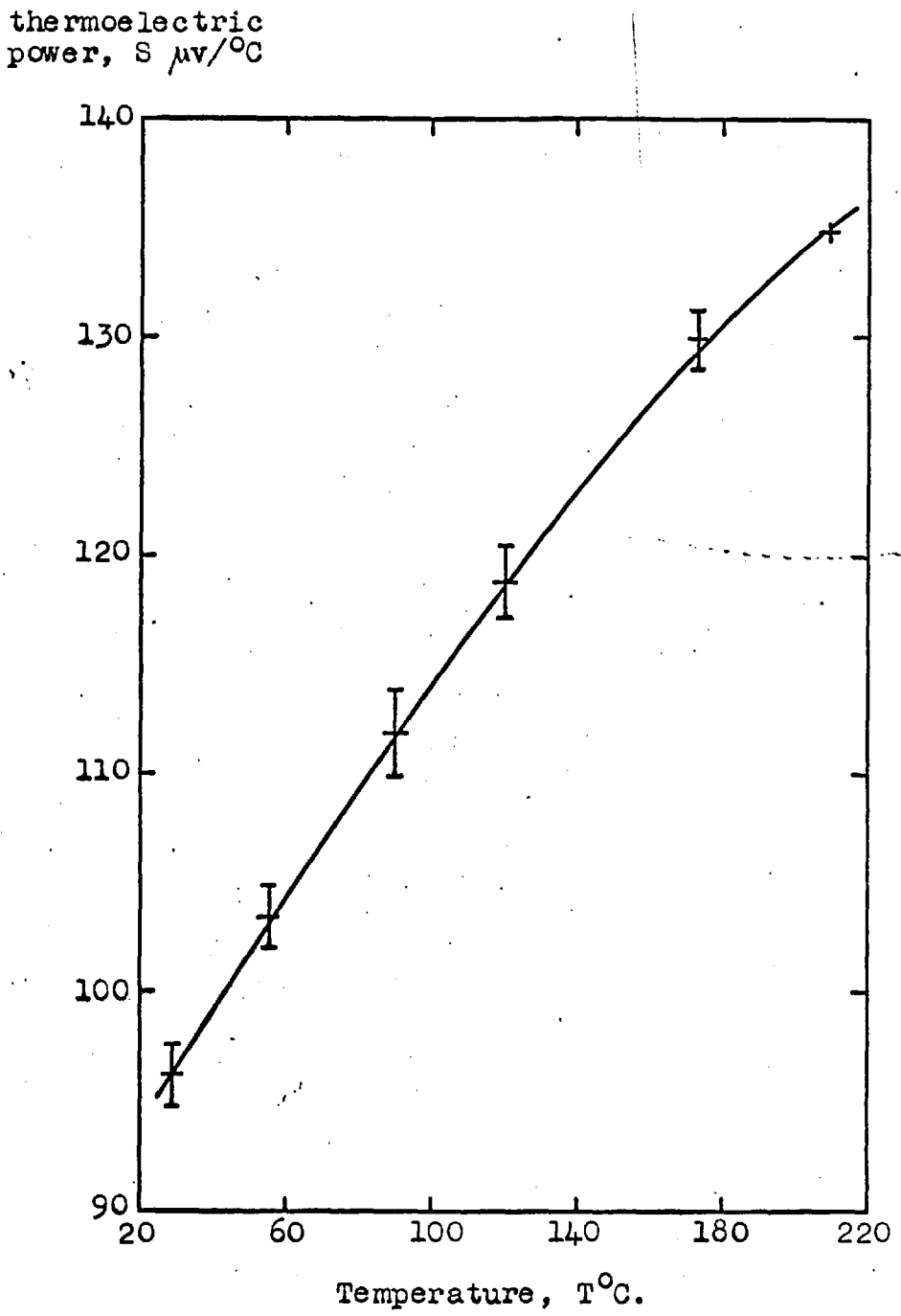


Figure 21. Absolute thermoelectric power of as-grown antimony telluride.

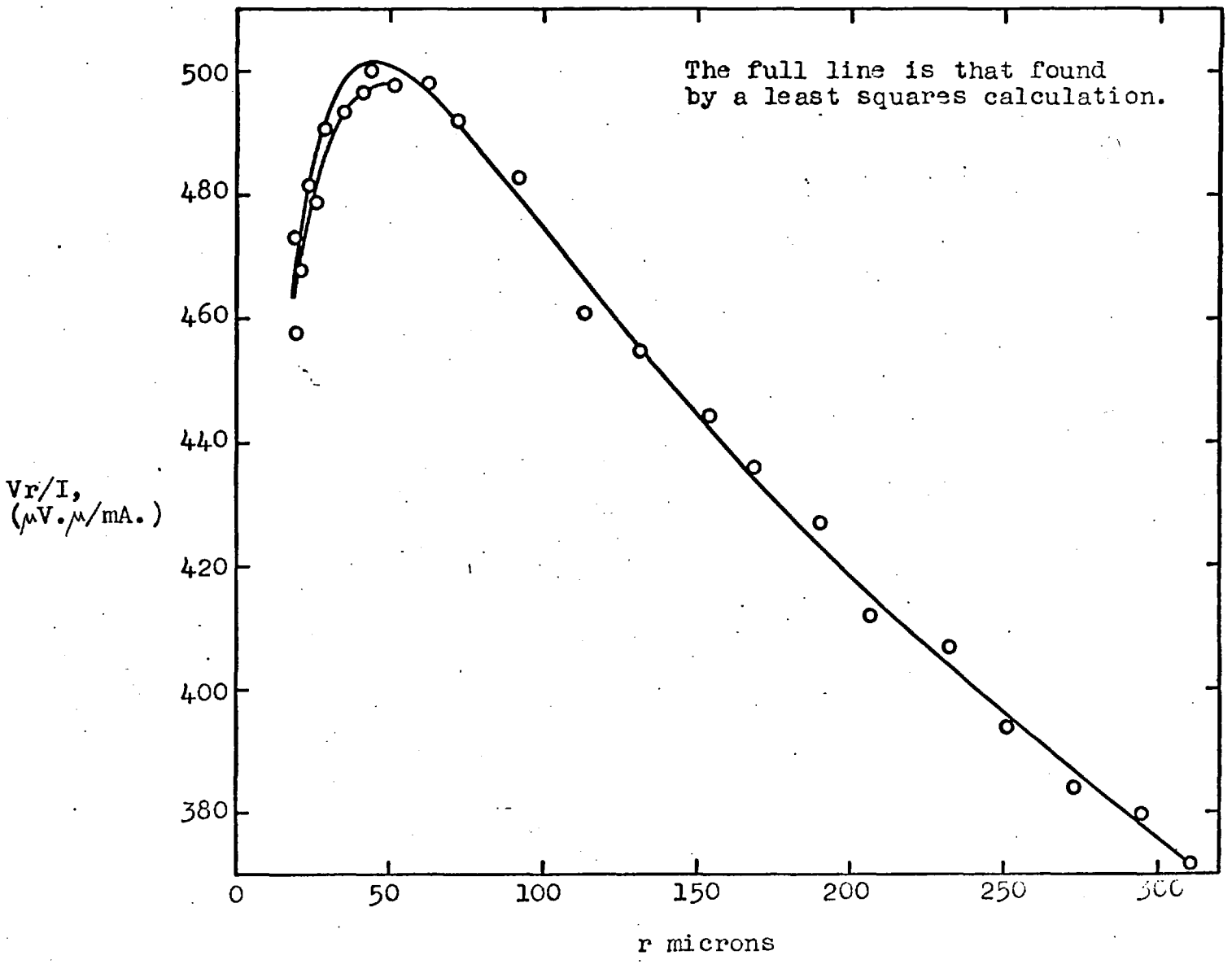


Figure 22. Typical results of a four probe experiment.

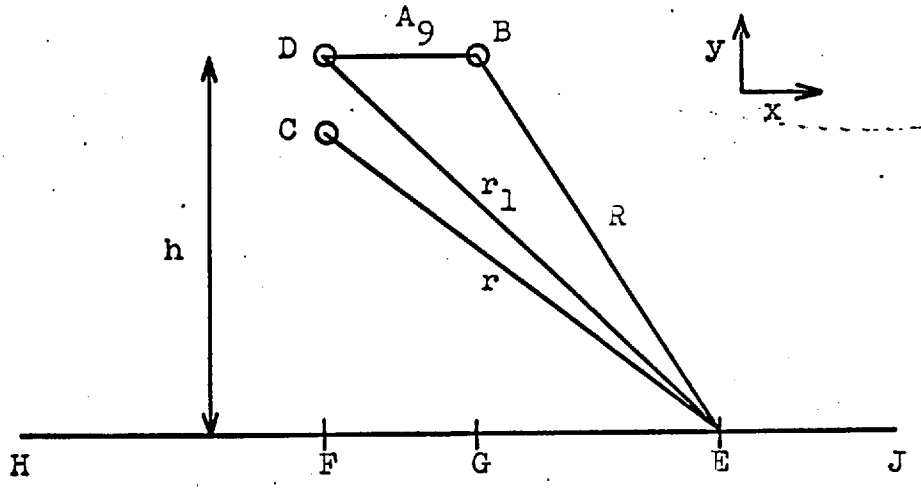


Figure 23. Illustrating the effect of errors in the determination of position of the current electrode.